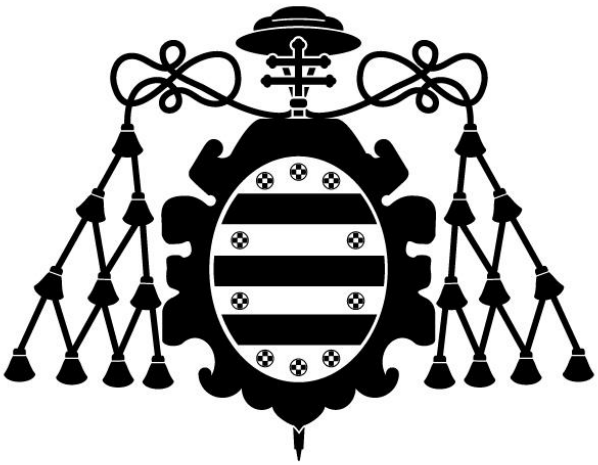

Universidad de Oviedo
*Universidá d'Uviéu*
*University of Oviedo*

Programa de Doctorado de Materiales

# FABRICATION AND MAGNETIC CHARACTERIZATION OF FERROMAGNETIC ANTIDOT ARRAYS THIN FILMS

TESIS DOCTORAL

Mohamed Salaheldeen Mohamed Hassan

June 2019

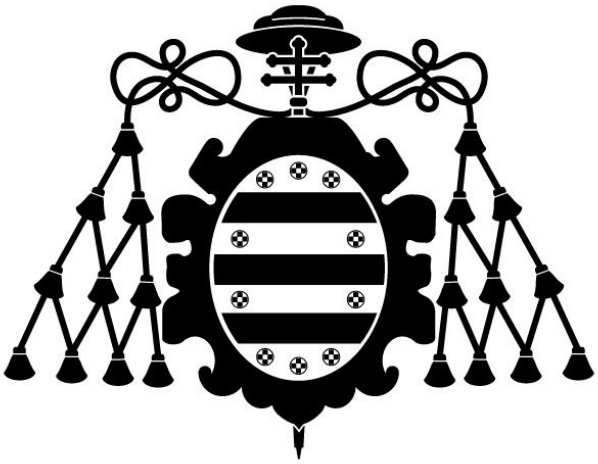

Universidad de Oviedo
*Universidá d'Uviéu*
*University of Oviedo*

Programa de Doctorado en Materiales

# FABRICATION AND MAGNETIC CHARACTERIZATION OF FERROMAGNETIC ANTIDOT ARRAYS THIN FILMS

TESIS DOCTORAL

**Prof. Dr. Agustín Fernández Suarez**

**Prof. Dr. Víctor Manuel de la Prida Pidal**

Universidad de Oviedo
*Universidá d'Uviéu*
*University of Oviedo*

# RESUMEN DEL CONTENIDO DE TESIS DOCTORAL

| **1.- Título de la Tesis** | |
|---|---|
| Español: Fabricación y caracterización magnética de películas delgadas ferromagnéticas con estructuras ordenadas de antidots | Inglés: Fabrication and magnetic characterization of ferromagnetic antidot arrays thin film. |

| **2.- Autor** | |
|---|---|
| Nombre: Mohamed Salaheldeen Mohamed Hassan | Pasaporte: A |
| Programa de Doctorado: Materiales | |
| Órgano responsable: Comisión Académica Programa de Doctorado en Materiales | |

## RESUMEN (en español)


Este trabajo presenta un estudio sobre las propiedades magnéticas de las matrices de nanohuecos o "antidots" ordenadas hexagonalmente a nano escala en películas delgadas magnéticamente blandas (Ferromagnéticas, FM = Fe, Co, Ni y Ferrimagnéticas, FIM = Dy-Fe). Los arreglos de antidots se fabrican depositando los materiales magnéticos sobre membranas de alúmina nanoporosa con diferentes diámetros de poros que varían en el rango entre 32 ± 2 a 93 ± 1 nm. Por lo tanto, varios conjuntos de matrices FM-antidots se han fabricado con diferentes diámetros de antidots, d, pero distancia fija entre nanohuecos, $D_{int}$ y espesor de capa, t, lo que reduce la separación de borde a borde entre los antidots adyacentes, ($W = D_{int} - d$). La caracterización magnética se logra mediante métodos integrales como la magnetometría de muestra vibrante (VSM) y del efecto Kerr magnetoóptico (MOKE), así como los métodos de magnetometría microscópica, como la microscopía de fuerza magnética (MFM). Todos los métodos experimentales están respaldados por simulaciones micromagnéticas realizadas con el código mumax3. La presencia de antidots conduce generalmente a un efecto de endurecimiento magnético con mejoras de los campos coercitivos, por lo general, de hasta dos órdenes de magnitud. Se observa un cambio notable en la dependencia de los campos coercitivos con el tamaño de hueco, d, y la distancia entre bodes de nanohuecos, W, encontrándose un tamaño crítico para la distancia al borde, $W_c$, al que se invierte el comportamiento del campo coercitivo. La disminución de la coercitividad en el plano para las muestras de FM-antidots con $W < W_c$ da lugar a un aumento de la contribución del componente magnética fuera del plano con el aumento del tamaño del antidot. El cambio en el tamaño del nanohueco de las muestras de antidots se refleja en la imanación remanente, como así lo revela la simulación micromagnética. Dependiendo de los parámetros d y W, se pueden identificar tres patrones de dominio distintos. El patrón de dominio para muestras con un diámetro de nanohueco pequeño ($W > 50$ nm) donde se reproduce la estructura pelicular bien conocida, con una fuerte anisotropía magnética en el plano de la muestra. Para muestras de antidots con $W \approx W_c$, la estructura del dominio magnético presenta paredes de superdominio de alta energía, los HE-SDW, y los ciclos de histéresis muestran un comportamiento magnético de múltiples pasos y un campo coercitivo máximo en la dirección del plano de la muestra. Finalmente, la estructura del dominio magnético que surge en las muestras de antidots con un diámetro de nanohueco grande, donde $W < W_c$, dominan los procesos por rotación de la imanación, que se asemeja al estado de orden magnético de *spin-ice* en hielo artificialmente frustrado geométricamente, aumentando la anisotropía magnética

fuera de plano. Además, la anisotropía magnética presenta un cruce inesperado desde la dirección en el plano de la muestra a la posición de fuera del plano, debido al aumento de la densidad de energía efectiva de la anisotropía magnética perpendicular con el tamaño del nanohueco, para las distintas muestras de antidots. Cabe destacar los elevados valores de la densidad de energía de la anisotropía magnética perpendicular efectiva, $K_{eff}$ x t, para aleaciones de antidots de Dy-Fe con espesores, t = 30 nm, (3.8 erg / $cm^2$) y (1.44 erg / $cm^2$) para matrices de antidots de Ni con t = 20 nm, que se han obtenido en este trabajo. Además, se ha encontrado que la distribución de los elementos de las aleaciones Dy-Fe alrededor y entre los nanohuecos de las muestras de antidots, la compleja inversión de la imanación y la alta estabilidad térmica de la estructura hexagonal de los conjuntos de antidots, permiten sintonizar tanto la temperatura de Curie como el punto de compensación de la aleación ferrimagnética a valores cercanos a temperatura ambiente para las muestras de antidots de aleaciones Dy-Fe. Estas observaciones pueden ser de enorme interés para el desarrollo de nuevos sensores magnéticos y avalan el comportamiento de las películas magnéticas de antidots como excelentes candidatas para diseño de medios de grabación magneto-óptica perpendicular y dispositivos para spintrónica basados en técnicas de deposición asistida mediante plantillas nanoestructuradas.

**RESUMEN (en Inglés)**

This work presents a study about the magnetic properties of nanoscaled, hexagonally ordered antidot arrays within magnetically soft thin films (Ferromagnetic, FM= Fe, Co, Ni and Ferrimagnetic, FIM=Dy-Fe alloy). The antidot arrays are fabricated by depositing the magnetic materials onto nanoporous alumina membranes with different pore diameters varying in the range between 32±2 to 93±1 nm. Therefore, several sets of FM- antidot arrays thin films have been fabricated with different hole diameter, d, but fixed inter-hole distance, $D_{int}$, and layer thickness, t, therefore reducing the edge-to-edge separation between adjacent antidots, (W= $D_{int}$ – d). Magnetic characterization is achieved by integral methods such as vibrating sample magnetometry (VSM) and magneto-optical Kerr effect (MOKE) measurements, as well as microscopic magnetometry methods, such as magnetic force microscopy (MFM). All experimental methods are supported by micromagnetic simulations performed with mumax3 code. The presence of the antidots generally leads to a magnetic hardening effect with enhancements of the coercive fields by typically two orders of magnitude. A dramatic change in the coercive fields dependence with W and d have been found at a critical edge to edge distance, $W_c$, which the coercive fields behaviour with W is reversed. The decreasing of the in-plane coercivity for FM-antidot samples with W < $W_c$ gives rise to an increase of the out-of-plane magnetic component contribution with the antidot hole size increasing. Changing in nanohole size of the antidot samples reflects in the remanent magnetization, as revealed by micromagnetic simulation. Dependent on the d and W, three distinct domain patterns can be identified. The domain pattern for samples with small hole diameter where (W > 50 nm) show the well-known leaf structure with a strong in-plane magnetic anisotropy of the magnetization reversal. For antidot samples with W ≈ $W_c$ the magnetic domain structure shows high-energy super domain walls, HE-SDWs, and hysteresis loops show a multi-steps magnetic behaviour and maximum in-plane coercive field. Finally, the magnetic domain structure arising in antidot arrays with large hole diameter where (W < $W_c$) resembles the spin ordered state in geometrically frustrated artificial spin-ice and increase the out-of-plane magnetic anisotropy of the magnetization reversal. In addition, the magnetic anisotropy exhibits

an unexpected crossover from the in-plane to out-of-plane direction due to the increasing of the effective perpendicular magnetic anisotropy energy density with the hole size of antidot arrays. It is worth to mention large values of effective perpendicular magnetic anisotropy energy density, $K_{eff} \times t$, for Dy-Fe antidot alloys with t = 30 nm (3.8 erg/cm$^2$) and (1.44 erg/cm$^2$) for Ni antidot arrays with t = 20 nm that have been obtained in this work. Furthermore, the unique elements distribution of Dy-Fe alloys around and between the holes of antidot samples, the complex magnetization reversal and the high thermal stability of the hexagonal structure of antidot arrays enable us to tailor the Curie temperature and the room temperature compensation point of Dy-Fe antidot alloys. These observations can be of high interest for the development of novel magnetic sensors and represent an excellent candidate for magneto-optic perpendicular recording patterned media and spintronic devices based on template-assisted deposition techniques.

**SR. PRESIDENTE DE LA COMISIÓN ACADÉMICA DEL PROGRAMA DE DOCTORADO EN MATERIALES**

To My

Father & Mother

# Acknowledgments

In the next few words, I would like to thank and express my gratitude to everybody who supported or helped me in this work.

I would like to thank the supervisors **Prof. Agustín Antonio Fernández Suárez, Prof. Victor Manuel del la Prida Pidal** for the real support, help, guidance and the fruitful discussions.

It was a pleasure to work in the Magnetic Materials and Nanomaterials research group in Department of Physics, Oviedo University with **Prof. Blanca Hernando Grande, Dr. Victor Vega and Dr. Rafael Caballero-Flores, Dr. Javier García and Dra. Ana Silvia González.**

I would like to acknowledge the work financial support provided by the Spanish MINECO Ref. MAT2016-76824-C3-3-R and MAT2013-48054-C2-2-R, by the Asturias Government Ref. FC-15-GRUPIN14-085 research projects.

I greatly thank **Prof. Blanca Hernando, Victor Vega and R. Caballero-Flores** for the very nice time and the continuous assistance in general life in Oviedo, and I specially thank my friend Abd El-Moez A. Mohamed, who has kept in touch despite the far away distance.

I must express my profound gratitude to Shaimaa my wife and my dear kids Mariam, Ahmed and Omar who were patient with me. I'd like to say to them: "*I apologize to you about the times when which I could not be with you because of research. Thanks for your quietness and patience for sometimes which helped me to research. You are my soul, my heart and my hope in this life. Really, I love you a lot.*"

# Abstract

This work presents a study about the magnetic properties of nanoscaled, hexagonally ordered antidot arrays within magnetically soft thin films (Ferromagnetic, FM= Fe, Co, Ni and Ferrimagnetic, FIM=Dy-Fe alloy). The antidot arrays were fabricated by depositing the magnetic materials onto the planar surface of nanoporous alumina membranes with different pore diameters varying in the range between 32±2 to 93±1 nm. Therefore, several sets of FM and FIM- antidot arrays thin films have been fabricated with different hole diameter, d, but fixed inter-hole distance, $D_{int}$, and layer thickness, t, therefore reducing the edge-to-edge separation between adjacent antidots, ($W= D_{int} – d$). Magnetic characterization is achieved by integral methods such as vibrating sample magnetometry (VSM) and magneto-optical Kerr effect (MOKE) measurements, as well as microscopic magnetometry methods, such as magnetic force microscopy (MFM). All experimental methods are supported by micromagnetic simulations performed with mumax$^3$ code. The presence of the antidots generally leads to a magnetic hardening effect with enhancements of the coercive fields by typically up to two orders of magnitude. A noticeable change in the coercive fields dependence with W and d have been found at a critical edge to edge distance, $W_c$, which the coercive fields behaviour with W is reversed. The decreasing of the in-plane coercivity for FM-antidot samples with $W < W_c$ gives rise to an increase of the out-of-plane magnetic component contribution with the antidot hole size increasing. Changing in nanohole size of the antidot samples reflects in the remanent magnetization, as revealed by micromagnetic simulation. Depending on the d and W lattice parameters, three distinct domain patterns can be identified. The domain pattern for samples with small hole diameter where ($W > 50$ nm) show the well-known leaf structure with a strong in-plane magnetic anisotropy of the magnetization reversal. For antidot samples with $W \approx W_c$ the magnetic domain structure shows high-energy super

domain walls, HE-SDWs, and hysteresis loops show a multi-steps magnetic behaviour and maximum in-plane coercive field. Finally, the magnetic domain structure arising in antidot arrays with large hole diameter where ($W < W_c$) resembles the spin ordered state in geometrically frustrated artificial spin-ice and increase the out-of-plane magnetic anisotropy of the magnetization reversal. In addition, the magnetic anisotropy exhibits an unexpected crossover from the in-plane to out-of-plane direction due to the increasing of the effective perpendicular magnetic anisotropy energy density with the hole size of antidot arrays. It is worth to mention large values of effective perpendicular magnetic anisotropy energy density, $K_{eff} \times t$, for Dy-Fe antidot alloys with t = 30 nm (3.8 erg/cm$^2$) and (1.44 erg/cm$^2$) for Ni antidot arrays with t = 20 nm that have been obtained in this work. Furthermore, the unique elements distribution of Dy-Fe alloys around and between the holes of antidot samples, the complex magnetization reversal and the high thermal stability of the hexagonal structure of antidot arrays enable us to tailor the Curie temperature and the room temperature compensation point of Dy-Fe antidot alloys. These observations can be of high interest for the development of novel magnetic sensors and represent an excellent candidate for magneto-optic perpendicular recording patterned media and thermo-magnetic recording patterned media based on template-assisted deposition techniques.

# Resumen

Este trabajo presenta un estudio sobre las propiedades magnéticas de las matrices de nanohuecos o "antidots" ordenadas hexagonalmente a nano escala en películas delgadas magnéticamente blandas (Ferromagnéticas, FM = Fe, Co, Ni y Ferrimagnéticas, FIM = Dy-Fe). Los arreglos de antidots se fabrican depositando los materiales magnéticos sobre membranas de alúmina nanoporosa con diferentes diámetros de poros que varían en el rango entre 32 ± 2 a 93 ± 1 nm. Por lo tanto, varios conjuntos de matrices FM y FIM-antidots se han fabricado con diferentes diámetros de antidots, d, pero distancia fija entre nanohuecos, $D_{int}$ y espesor de capa, t, lo que reduce la separación de borde a borde entre los nanohuecos o antidots adyacentes, ($W = D_{int} - d$). La caracterización magnética se logra mediante métodos integrales como la magnetometría de muestra vibrante (VSM) y del efecto Kerr magnetoóptico (MOKE), así como los métodos de magnetometría microscópica, como la microscopía de fuerza magnética (MFM). Todos los métodos experimentales están respaldados por simulaciones micromagnéticas realizadas con el código mumax[3]. La presencia de antidots conduce generalmente a un efecto de endurecimiento magnético con mejoras de los valores de campo coercitivo de hasta dos órdenes de magnitud. Se observa un cambio notable en la dependencia de los campos coercitivos con el tamaño de hueco, d, y la distancia entre bordes de nanohuecos, W, encontrándose un tamaño crítico para la distancia entre bordes de antidots, $W_c$, al que se invierte el comportamiento del campo coercitivo. La disminución de la coercitividad en el plano para las muestras de FM-antidots con $W < W_c$ da lugar a un aumento de la contribución del componente magnética fuera del plano con el aumento del tamaño del antidot. El cambio en el tamaño del nanohueco de las muestras de antidots se refleja en la imanación remanente, como así lo revela la simulación micromagnética. Dependiendo de los parámetros d y W, se pueden identificar tres patrones de dominios magnéticos

distintos. El patrón de dominio para muestras con un diámetro de nanohueco pequeño (W > 50 nm) donde se reproduce la estructura pelicular bien conocida, con una fuerte anisotropía magnética en el plano de la muestra. Para muestras de antidots con $W \approx W_c$, la estructura del dominio magnético presenta paredes de superdominio de alta energía, los HE-SDW, y los ciclos de histéresis muestran un comportamiento magnético de múltiples pasos y un campo coercitivo máximo en la dirección del plano de la muestra. Finalmente, la estructura del dominio magnético que surge en las muestras de antidots con un diámetro de nanohueco grande, donde $W < W_c$, dominan los procesos por rotación de la imanación, que se asemeja al estado de orden magnético de *spin-ice* en hielo artificialmente frustrado geométricamente, aumentando la anisotropía magnética fuera del plano. Además, la anisotropía magnética presenta un cruce inesperado desde la dirección en el plano de la muestra a la posición de fuera del plano, debido al aumento de la densidad de energía efectiva de la anisotropía magnética perpendicular con el tamaño del nanohueco, para las distintas muestras de antidots. Cabe destacar los elevados valores de la densidad de energía de la anisotropía magnética perpendicular efectiva, $K_{eff} \times t$, para aleaciones de antidots de Dy-Fe con espesores, t = 30 nm, (3.8 erg / $cm^2$) y (1.44 erg / $cm^2$) para matrices de antidots de Ni con t = 20 nm, que se han obtenido en este trabajo. Además, se ha encontrado que la distribución de los elementos de las aleaciones Dy-Fe alrededor y entre los nanohuecos de las muestras de antidots, la compleja inversión de la imanación y la alta estabilidad térmica de la estructura hexagonal de los conjuntos de antidots, permiten sintonizar tanto la temperatura de Curie como el punto de compensación de la aleación ferrimagnética a valores cercanos a temperatura ambiente para las muestras de antidots de aleaciones Dy-Fe. Estas observaciones pueden ser de enorme interés para el desarrollo de nuevos sensores magnéticos y avalan el comportamiento de las películas magnéticas de antidots como excelentes candidatas para

diseño de medios de grabación magneto-óptica perpendicular y dispositivos para spintrónica basados en técnicas de deposición asistida mediante plantillas nanoestructuradas.

# Contents

# Chapter 1: Introduction

In condensed matter physics, materials science, chemistry, mechanical and electrical engineering, research on the nano-scale has gained particular attention, as much as it reveals novel effects from fundamental relevance and paves the way for future technologies [1,2] Subject of research is so-called nanostructured materials, which can be classified as objects with a characteristic length scale in the order of few nanometers in at least one dimension [3,4] The computers and electronic devices have become indispensable companions in our everyday life through an abundance of applications in education, medicine, automotive industry, and all the way to space industry. Most important material traits involved in these devices at the atomic and nanometre scales are the electron's charge and spin, which may couple to each other through direct and indirect interactions, all building up a rather new field of research called as "spintronics" [5,6] The term "spintronics" (SPIN Transport electrONICS), introduced in 2000 [7] designates a field of electronics aimed to manufacture devices, the electrical characteristics of which are controlled by modifying its spin state. The emerging of spintronics is usually associated with observation of giant magnetoresistance effect (GMR 1988) in three-layer and multilayer metallic F/N structures (F, N = ferromagnetic and normal metal, respectively) [8,9]

Indeed, this discovery, at first, initiated a huge increase of research in this area and second, almost immediately found some application such as, magnetic field sensors, which put in the basis of reading heads for magnetic hard disk drives and rising to a new level of magnetic data storage capacities, biosensors, microelectromechanical systems (MEMS) and other devices [10]. Both inventors shared the Nobel Prize for this

achievement in 2007. After its first economic usage as a magnetic sensor element [11], it is undoubtedly found its way to commercialization as 'read-head' for magnetic hard disk drives in 1997 by IBM [12] and, thus, became amongst the most important innovations in the last decades, only 9 years after its discovery.

Of particular importance in the evolution toward higher areal densities is the transition from longitudinal to perpendicular magnetic recording (PMR) [13], whereas a difference from longitudinal magnetic recording (LMR) technology [14], the out-of-plane orientation of the bit magnetization is perpendicular to the disk surface. One of the fundamental advantages of PMR is that it allows to reach higher magnetic writing fields as compared to LMR, and thus to use materials with higher magnetic anisotropy (Ku). The possibility of using high-Ku materials is critically important to maintain the stability of the magnetic bits against superparamagnetic effects [15,16], which eventually might cause the bit magnetization to flip due to thermal fluctuations and hence lead to data loss. At present the areal density approaches the 1 $Tb/in^2$ density point, which means that each individual bit, despite being composed by several magnetic grains, is only ~25 $nm^2$ in size. A second aspect concerning superparamagnetic effects is related to the bit volume V, because the time between fluctuations of the bit magnetization is essentially proportional to Ku×V [15]. This quantity determines the nonvolatility of the magnetic medium. Therefore, to further decrease the bit volume, for example, by using materials with smaller grains, it is in principle necessary to accordingly increase Ku [17]. This implies that the higher magnetic fields provided by PMR are required for the writing process.

Within the next 10 years due to the continuous development of emergent technologies such as heat-assisted magnetic recording (HAMR), bit-patterned magnetic recording [18–20], shingled magnetic recording (SMR) [21] and/or two-dimensional

magnetic recording (TDMR) [22] , the areal bit density of data storage will increase more than 10 Tb/in$^2$ as reported in Fig. 1.1.

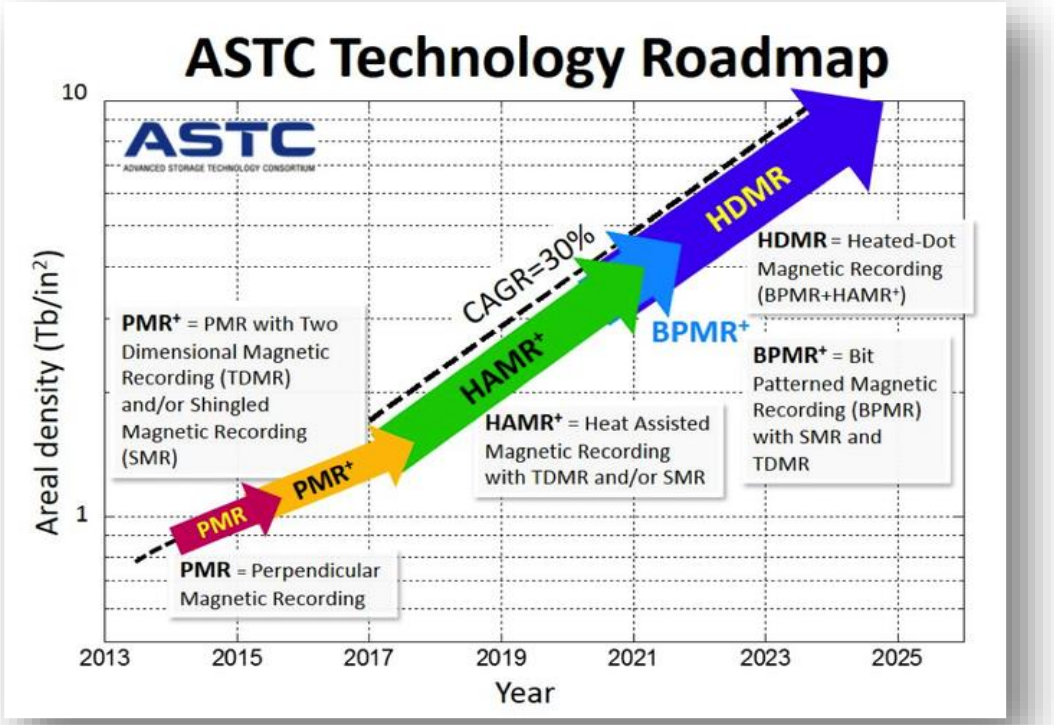


**Figure 1.1**: Bit areal density progress in magnetic hard disk drives [23]

The engineering of magnetic systems based on planar patterned nanostructures by properly controlling the shape and size of the patterned nano-objects allows obtaining magnetic films with non-collinear magnetization distribution, thus enabling the development of magnetic data processing devices with perpendicular architecture and spin-based electronics [24]. Nanoscale antidot arrays lattices in magnetic materials, i.e., periodic spatial arrangements of nanometric holes in thin metal films, have been studied in a wide scientific and technical scope. Tuned magnetic frustration in spin ice [25,26] and spin glass [27] behaviour have been investigated and detected in magnetic nanoscale antidot arrays. Moreover, their ability to act as magnonic crystals which -similar to

photonic crystals for photons- exhibits a periodic potential for magnons, allowing to tailor the spin wave dispersion [3,28]. Thus, antidot arrays systems are promising candidates for applications in the field of spintronics as spin wave filters or spin wave guides [29,30]

In addition, the antidot arrays with perpendicular easy magnetic anisotropy axis are interesting systems from the application point of view in superconductor as flux pining centres [31,32]. Furthermore, many studies used magnetic materials with a perpendicular magnetic anisotropy as host films for the antidot lattices and declared their efficiency for magnetic recording and bit patterned media compared to unpatterned films [33–35]. The extraordinary features exhibited by these nanostructured materials comes from their relatively large surface to volume ratio, which influences the shape, morphology, crystalline structure, and surface roughness of the material in the nanoscale range [36].

These artificial arrays have been recently used in ultra-high density data storage applications [37,38] where the antidot lattices allow to define a peculiar type of bit patterned media that can overcome the superparamagnetic limit due to the non-formation of isolated magnetic domains [39,40]. The presence of antidots in the continuous thin film form a complex magnetic domain structure at remanent state such as superdomains, as shown in Fig. 1.2. The latter are exotic magnetic domain structures characterized by a common average magnetization, while presenting inhomogeneous magnetization inside an antidot cell [41]. Neighbouring superdomains with different average magnetization are separated by superdomains walls (SDWs) (inset of Fig. 1.2b). The geometrical confinement of the magnetization between holes may find different applications: in the field of information storage, the magnetic entity surrounded by the nearest antidots can be used as memory bits [42]. Magnetic domain structures arising in antidot arrays have been experimentally observed by means of magnetic force microscopy (MFM), Lorentz microscopy, X-ray photoemission electron microscopy, and magneto-optic Kerr effect

measurements [41,43–45] Particular attention has been devoted to the nucleation and propagation of discrete domain chains, to explore the possibility of controlling domain walls with well-defined magnetic configurations [41,46] A fundamental support to understand the complex magnetic behaviour exhibited by the antidot arrays has been found in micromagnetic simulations, which are based on the solution of the Landau-Lifshitz equation as described in chapters 5 and 6 and reported in [37,47–49]

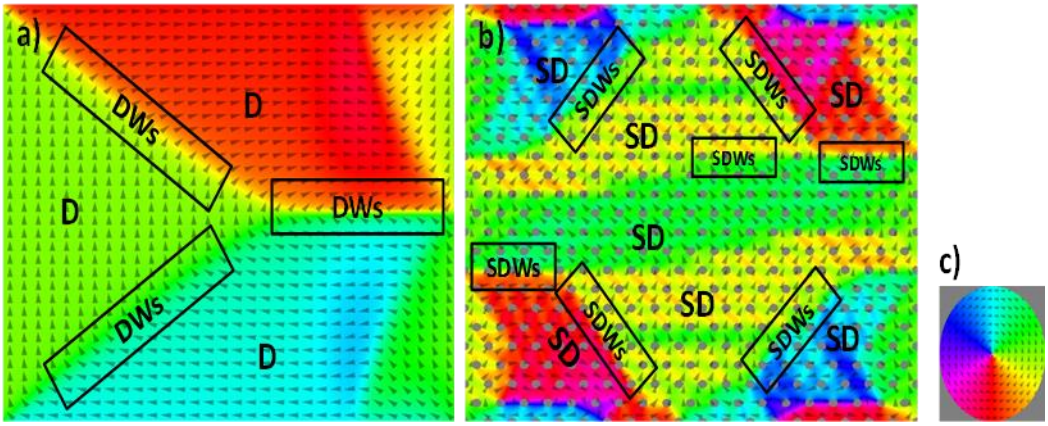


**Figure 1.2:** a) Simulated magnetic domain structure at remanent state for Ni continuous thin film (inset shows the large magnetic domain, D, separated with domain walls, DWs). b) Simulated magnetic domain configuration at remanent state for Ni antidot arrays with hole diameter, d = 40 nm and interpore distance, $D_{int}$ = 105 nm (inset shows the formation of magnetic super domains, SD, separated with super-domain walls, SDWs. C) color mapping where each color indicates easy magnetization direction for each single D or SD.

Antidot arrays are commonly prepared by different nanolithography techniques [50–53], focused ion beam lithography [54–56], holographic lithography [57,58], colloidal lithography [59], and block copolymer self-assembly [60]. Some of these techniques, however, are restricted to laboratory scale applications by expensive procedure or limited patterned areas. Antidot arrays based on nanoporous anodic alumina templates, allow obtaining elaborated and reproducible 3D arrangement of self-ordered

nanopores with precise control on the lattice parameters of the former alumina templates, such as the pore diameter, interpore distance and pore length. Normally the periodical ordering cannot be achieved using the latter method, but this problem has already been successfully addressed even for wafer-size scale by introducing pre-patterning step before anodization of the alumina surface [61,62].

## 1.1 Outline of the thesis

This thesis is composed of eight Chapters. The next two Chapters (Chapter two and three) discuss on the theoretical frameworks and the experimental techniques used in this work. This is then followed by two parts. Chapters four, five and six make up part one of the thesis and it starts by investigating the magnetic properties of ferromagnetic (Fe, Co and Ni) antidot arrays thin film. Therefore, Chapter four focused on the effect of antidot layer thickness on the magnetic anisotropy mainly the in-plane angular dependence of the coercivity and reduced remanence. Meanwhile, Chapter five studied deeply the influence of antidot hole diameter on the magnetic properties of FM-antidot arrays thin film and their effect on the micromagnetic domain structure. Finally, Chapter six investigated the tailored perpendicular magnetic anisotropy in Ni antidot arrays by varying the nanohole size of antidot arrays for spintronic application. Part two is made up by Chapter seven and eight. The preparation and characterization of RE-TM (Dy-Fe) alloys antidot thin film with different layer thickness and elemental/atomic concentration as ferrimagnetic on the magnetic properties such as the magnetic anisotropy, compensation point, and Curie temperature is presented in Chapter seven. After that, finally it comes the summary and main conclusions of the work at Chapter eight, together the bibliography.

# Chapter 2: Phenomena and concepts

The interesting phenomena displayed by magnetic materials based on antidot arrays thin films are governed by their geometrical parameters and lattice symmetry. This Chapter discusses about the most important concepts in magnetic antidot arrays thin films to have a deep understanding of the related phenomena.

## 2.1 Exchange Interaction

To explain the main properties of ferromagnetic antidot materials like the magnetic ordering, we introduce the magnetic interactions theories and the existence of magnetic domains.

Heisenberg and Dirac independently described an interaction between quantum mechanical particles, with which it was possible to explain why the magnetic moments in a ferromagnetic state align parallel to each other [63,64]. This phenomenon was named as "exchange interaction". Within the Heisenberg model, the exchange interaction energy between neighboring magnetic moments reads:

$$E_{ex} = -J_{ij}\,\overrightarrow{S_i}\,.\,\overrightarrow{S_i} \qquad (2.1)$$

where $\overrightarrow{S_i} = \overrightarrow{m_i}/\overrightarrow{m_i}$. For a ferromagnet, $the\ coupling\ constant\ \ J_{ij}$ is positive for ferromagnetic ordering, so that a parallel alignment of spins results in a reduction of interaction energy, while a negative $J_{ij}$ describes the antiferromagnetic ordering. When instead of localized magnetic moments the magnetization, M, is regarded as a property in the sense of a continuum theory, which is especially relevant in the context of micromagnetic simulations (see section 6.4), the exchange energy can be expressed as:

$$E_{ex} = \int_V \frac{A_{exch}}{M_s} \left( \left( \frac{\partial \vec{M}}{\partial x} \right)^2 + \left( \frac{\partial \vec{M}}{\partial y} \right)^2 + \left( \frac{\partial \vec{M}}{\partial y} \right)^2 \right) V \qquad (2.2)$$

here, the exchange stiffness constant $A_{exch} = (\mathrm{cJS}^2)/\mathrm{a}$ is introduced. a is the lattice constant, and the parameter c takes the values 1, 2 and 4 for simple cubic, sc, body-centered cubic, bcc, and face-centered cubic, fcc, lattice symmetry, respectively [65].

## 2.2 Magnetic Domains and Domain Walls

In general, the magnetization of a ferromagnetic ordering is not homogeneous, but it is divided into a multitude of regions in which the magnetization has the same easy magnetization direction. These regions are called as magnetic domains. Each two neighboring magnetic domains are separated by a domain wall, DW, where the magnetization gradually reorients over a distance in the order of several hundreds of the lattice constants, a.

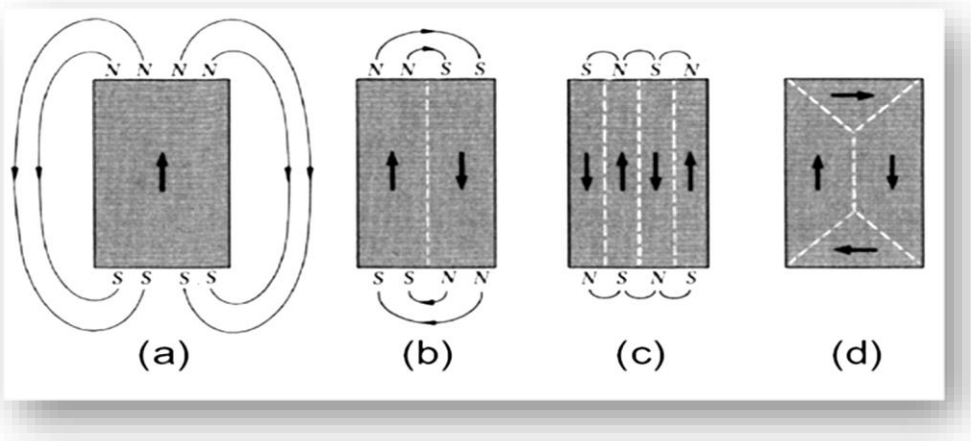


**Figure 2.1:** The formation of magnetic domains reduces the stray field energy. Details see text. Image from Ref [66].

Magnetic domains are formed due to a competition of the different energy contributions in the magnetic system such as different terms of magnetic anisotropy.

While the magnetization with a single domain is favorable in terms of exchange interaction, the resulting demagnetizing fields are usually large, as sketched in Fig. 2.1 a. Such a configuration is thus only possible if the stray field energy can be overcompensated by magnetocrystalline anisotropy [66]. Splitting the sample into two domains with opposite magnetization directions reduces the stray field energy (Fig. 2.1 b). The cost for the additional domain is an increase in exchange energy due to formation of the domain wall. A very favorable configuration is shown in Fig. 2.1d, where almost no stray field emerges at the samples edges due to a closure of the magnetic flux. Such a configuration, however, can only be attained when the magnetocrystalline anisotropy is negligible, for example in micron scaled rectangular prisms of the Permalloy [66].

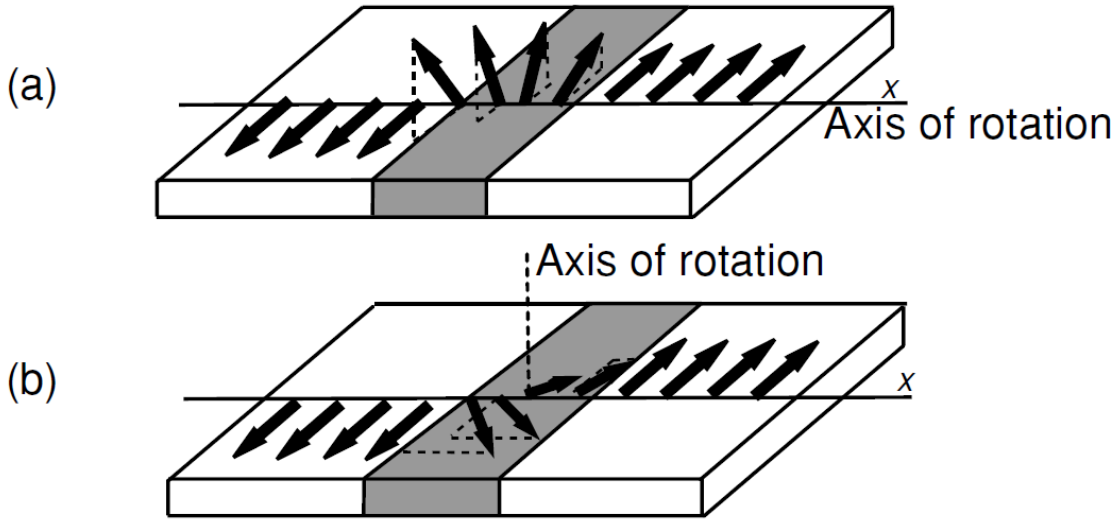


**Figure 2.2**:a) Bloch and b) Néel domain Wall, as it usually occurs in soft magnetic thin films [67].

Two common types of domain wall are illustrated in Fig. 2.2. In bulk ferromagnetic materials, the domain walls are usually in the form of Bloch domain walls.

In a Bloch wall, the magnetization always stays within the DW plane. The width of the domain wall is hereby given by a competition between exchange interaction and the magnetocrystalline anisotropy. In soft magnetic thin film elements, Fe, Co and Ni, the formation of Bloch domain walls would lead to an out of plane component of the magnetization, which is unfavorable due to shape anisotropy with strong in-plane magnetic anisotropy.

In this context, the exchange length, $l_{exch}$, is an important property:

$$l_{exch} = \sqrt{\frac{A_{exch}}{\mu_0 M_s^2}} \qquad (2.3)$$

For the materials used for the preparation of the antidot arrays in this thesis, the values are $l_{exch}$ = 2.4 nm for Fe, $l_{exch}$ = 3.8 nm for Co, and $l_{exch}$ = 5.1 nm for Ni [68]. The corresponding Néel wall widths in polycrystalline samples of these materials are in the range between 30 and 200 nm [69,70]. Therefore, after/by modifying the geometrical parameters of antidot arrays we can tailor the micromagnetic domain structure and magnetic anisotropy, as it will be described in Chapters 5 and 6.

### 2.2.1 The coherence radius

The critical size and nucleation field for ideal magnetic particles were given for the following shapes: sphere, infinite long cylinder, prolate ellipsoid, and hollow cylinder [68]. The maximum size of the ferromagnetic material at which its magnetization reversal takes place by quasi-uniform magnetization rotation process rather than domain wall movement is called the characteristic length, $R_{Coh}$ and given approximately by [67,71]:

$$\left(R_{Coh} = \sqrt{24A/\mu_0 M_s^2} = \sqrt{24}\, l_{exch}\right) \qquad (2.4)$$

In this work we found a strong relation between the $R_{Coh}$ and the magnetic properties of ferromagnetic antidot arrays thin films.

## 2.3 Magnetic anisotropy in continuous thin film and antidot arrays thin films

Most of the previous works on antidot arrays are made by lithography, and they show homogeneous magnetic domain structures due to the spatial periodicity of the nanoholes arrangement. The magnetic behavior demonstrates a great enhancement in comparison with their counterpart continuous thin film. The anisotropy induced by the sample geometry and lattice symmetry define the magnetic behavior of the antidot arrays, such as coercivity, $H_C$, and reduced remanence, $m_r = Mr/M_S$ Many studies have shown that the intrinsic anisotropy of the unpatterned film is still present in the arrays [39,72]. The anisotropies that must be taken into account in the system of antidot arrays are:

### 2.3.1 Magnetocrystalline anisotropy

The energy corresponding to a given magnetization configuration of a ferromagnetic material depends on the relative orientation of the magnetization vector $\vec{M}$ and the crystal axes of the material. The origin of this magnetocrystalline anisotropy is the spin-orbit interaction. The easy magnetization axis lies along certain crystal directions, so that the ferromagnetic materials are easily magnetized and saturated by means of an external applied field along these preferred directions. Once the magnetization points in a favorable direction resulting in a square-like hysteresis loop as show in Fig. 2.3a. Such directions which minimize the energy are called easy anisotropy or magnetization axes (Fig. 2.3a). For a magnetocrystalline easy anisotropy axis, however, the orbital contribution to the magnetic moment is always maximized [73]. The energetically most unfavorable orientations of the magnetization are then called the hard

axis as shown in Fig. 2.3b. It takes relatively large fields to force the magnetization into such a direction, and once the external field is turned off; there is a tendency for the magnetization to rotate into a neighboring easy magnetization axis.

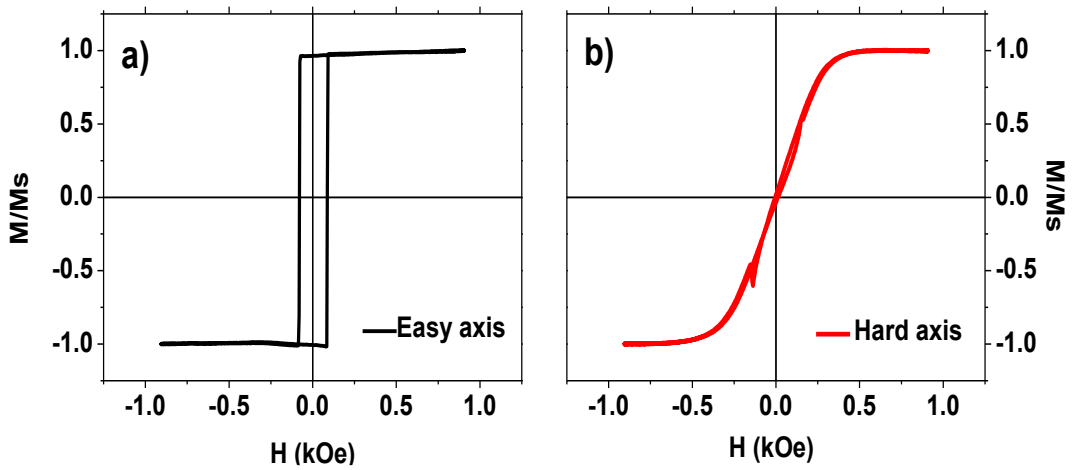


**Figure 2.3**: Schematic hysteresis loops for a magnetic field applied along (a) easy magnetization axis and (b) hard magnetization axis.

Also, ferromagnetic materials can be characterized by its magnetocrystalline anisotropy by the magnitude of the quality factor, Q, which is related to the ratio:

$$Q = \frac{2k}{M_s^2} \qquad (2.5)$$

If Q >> 1, the magnetic anisotropy behavior is dominated by the magnetocrystalline anisotropy; such materials are called as “hard” magnetic material. If Q << 1, the magnetic anisotropy behavior is governed by the magnetostatic energy and such materials are called as “soft” magnetic materials [74].

For the antidot arrays prepared in this thesis, the shape anisotropy always dominates over the magnetocrystalline anisotropy. This is due to the relatively small

intrinsic values for the anisotropy constants of the materials used for the thin film preparation.

### 2.3.2 Shape Anisotropy

Shape anisotropy in a magnetic specimen is purely a magnetostatic self-energy, which originates from the magnetostatic interaction among magnetic dipoles. To understand the effect of the shape of a specimen on developing this anisotropy, let us define the demagnetizing field.

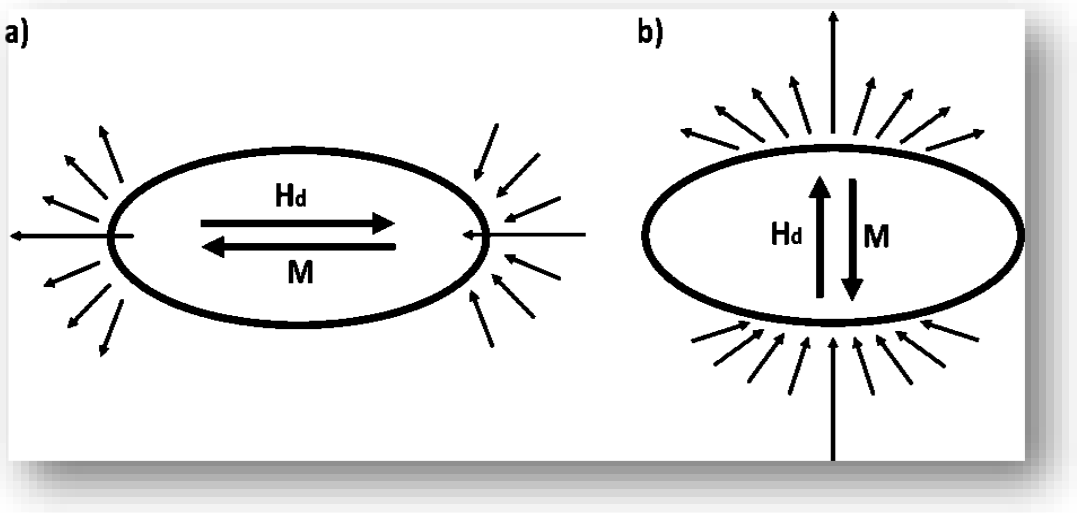


**Figure 2.4**: Magnetization (M) and demagnetizing field ($H_d$) in an ellipsoid when the external field is applied in the direction of the long axis (a) and short axis (b). $H_d$ is higher for (b) because of smaller distance between dipoles.

Consider an external magnetic field, $H_{ext}$, applied to an ellipsoid of ferromagnetic material in the direction parallel to the long axis, as show in Fig. 2.4a. This causes that the ellipsoid becomes magnetized with the north and south poles as shown in Fig. 2.4a. Due to the magnetic lines of force emerge out of the North Pole and ended at the South Pole, the field line inside the ellipsoid goes in the opposite direction to that of the external field $H_{ext}$. This fact makes to develop an intrinsic magnetic field which opposes to the

external magnetic field $H_{ext}$ [75]. This opposite field is called as the demagnetizing field, $H_d$, which originates from the magnetization of the specimen (M) and depends on the shape of the specimen. It can be written as:

$$\overrightarrow{H_d} = N_d . \vec{M} \qquad (2.6)$$

where $N_d$ is a demagnetization factor and depends solely on the shape of the specimen. Theoretical calculations have shown that $N_d$ is smaller for the longer axis [76]. This means, higher $N_d$ values are expected for external field $H_{ext}$ applied as shown in Fig. 2.4b and hence higher $H_d$ values. In other words, it is hard to magnetize in the short axis direction as shown in Fig. 2.4b and easier in the long axis direction as shown in Fig. 2.4a. In the case of magnetic thin films, the value of the in-plane demagnetization field, $N_d^{in-plane}$ is very much lower in comparison to the out-of-plane value, $N_d^{out-of-plane}$. Therefore, the easy magnetization axis always lies within the plane of the film and results the in-plane magnetic anisotropy for all the continuous thin film (CTF) samples within the scope of current thesis.

The shape anisotropy in Fe, Co and Ni continuous thin films always favors the in-plane magnetic anisotropy and is one of the major contributors to net effective magnetic anisotropy.

The magnetostatic energy per unit volume for a specimen with its saturation magnetization $M_s$ can be written as;

$$E_d = \frac{\mu_0}{2} M_s^2 \cos^2 \theta \qquad (2.7)$$

where $\mu_0$ is the magnetic permeability of free space and $\theta$ is the angle between the magnetization and normal to the film surface.

Let's define the $K_{sh} = (\mu_0 /2) M_S^2 = 2\pi M_s^2$ such that, $E_d = K_{sh} \cos^2 \theta$. We will call this constant $K_{sh}$ the "shape anisotropy constant", which has units of energy/volume. According to the equation of above, the shape anisotropy favors the in-plane magnetic anisotropy in thin films.

### 2.3.3 Uniaxial anisotropy

For a hexagonal crystalline structure, as in hcp cobalt, the equation for magnetocrystalline uniaxial anisotropy energy density can be written in its simplest form as:

$$E_u = -K_1 \cos^2 \theta + K_2 \cos^4 \theta \qquad (2.8)$$

where θ is the angle between the magnetization direction and the crystallographic c-axis, while $K_1$ and $K_2$ are the anisotropy constants. In expression (2.8), higher order terms are neglected as the anisotropy constant values are very small.

Depending on the values of $K_1$ and $K_2$, there are different kinds of anisotropy (i) with $K_1 = K_2 = 0$, the isotropic magnetic system; (ii) with $K_1 > 0$, the magnetic system with an easy magnetization axis along the c-axis and (iii) with $K_1 < 0$, the magnetic system with an easy magnetization plane perpendicular to the c-axis.

## 2.4 Magnetic anisotropy constants determined from experimental measurements

The magnetic anisotropy constants can be experimentally obtained from magnetic hysteresis curves, M(H). To derive those parameters, the magnetic hysteresis curves should be measured along both easy and hard magnetization axes by using instruments like the vibrating sample magnetometer (VSM), Superconducting Quantum Interference Device (SQUID), longitudinal and polar magneto-optical Kerr effect (MOKE)

measurements (L and P -MOKE) etc. When the field is applied along the easy magnetization axis, the external applied field required to get up to magnetic saturation, let us define as $H_{sat}^{easy}$, is minimum. Likewise, the value of $H_{sat}^{hard}$ is maximum when the field is applied in the parallel direction to one of the hard magnetization axes. Fig. 2.5 shows an example of the M–H hysteresis curves measured in both In-Plane (black) and Out-of-Plane (red) directions.

The magnetic hysteresis curve is defined by different physical parameters, such as coercive field ($H_C$), remanence magnetization (Mr), and saturation magnetization ($M_S$). The term $H_K$ is generally called the anisotropy field and there is a difference between external fields required for saturation of magnetization along the hard and easy magnetization axes:

$$H_k = H_{sat}^{hard} - H_{sat}^{easy} \qquad (2.9)$$

Then the overall or effective anisotropy constant can be calculated from experimental observations using the equation

$$K_{eff} = \frac{H_k \,.\, M_s}{2} \qquad (2.10)$$

Here, if $H_K$ is given in Oersted (or Gauss) and $M_S$ is in emu/cm$^3$ then we get $K_{eff}$ in erg/cm$^3$.

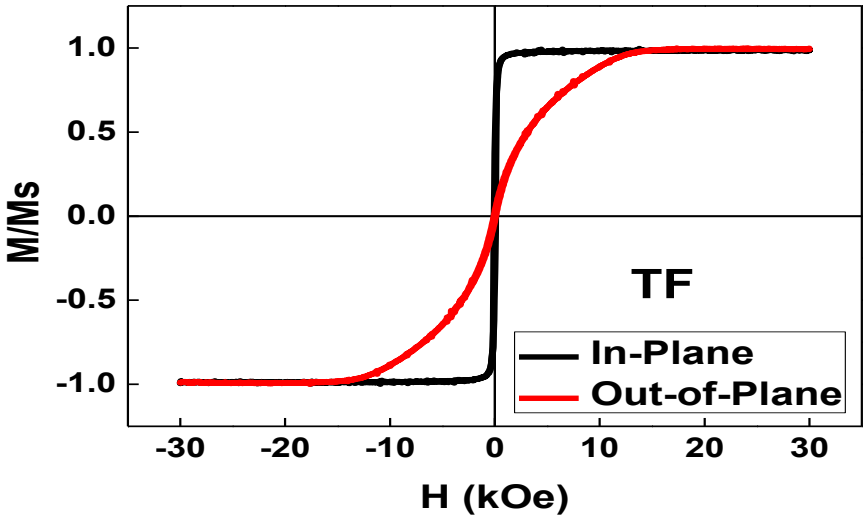


**Figure 2.5:** Typical M–H hysteresis curves for a continuous thin film of Ni with layer thickness of 20 nm. The hysteresis curves are measured with the applied field in the In-Plane (black) and Out of Plane (red) directions.

## 2.5 Coercivity

Generally, the coercivity is the resistance of a magnetic material to change in the magnetization, equivalent to the field intensity necessary to demagnetize the fully magnetized material. A periodic nonmagnetic inclusion i.e. nanoholes in a continuous thin film, CTF, reduces the local anisotropy energy, showing an interesting feature, the hardening effect on the magnetic properties when comparing to the corresponding CTF [77]. The presence of the pinning defects leads to an irregular DW movement consisting on a series of Bakhausen jumps as the wall skips from hole to hole [6]. If the defect width is smaller than the DW width, the coercivity is predicted by the micromagnetic calculations to increase linearly with the inter-nanohole distance, $D_{int}$ [78,79]. The DW is more strongly pinned if a larger number of defects fill the wall thickness.

Several works have demonstrated the relation between $H_{C//}$ and the geometric properties of the arrays. The in-plane coercivity, $H_{C//,}$ increases with $1/D_{int}$, hence stronger

magnetic fields are needed to overcome this pinning effect [80]. On the other hand, when $D_{int}$ is kept constant, $H_C$ is found to increase with the antidot hole diameter, d, due to the increasing of the local stray fields [39,51]. In general, the increases of the $H_C$ with increasing d and $D_{int}$, is attributed to the pinning of DW due to the local dipolar effect [81].

$$H_{C\,//} \alpha \frac{1}{D_{int} - d} \alpha \frac{1}{W} \qquad (2.11)$$

According to the micromagnetic model, the in-plane $H_C$ saturates for larger defects. As expected, the coercivity decreases with the separation distance between the edges of nanoholes, $W = D_{int} - d$. The separation of the non-magnetic structures implies a decrease in the magnitude of the demagnetizing energy relative to the total energy. In this thesis we find a limitation for this micromagnetic model where the behaviour of $H_C$ reversed after reaching a critical separation distance, $W_c$ , where $H_C \alpha \frac{1}{W}$ for $W \geq W_c$ and $H_C \alpha W$ for $W < W_c$ (as will be discussed in Chapter 5).

## 2.6 Objective of this work

This work is focused on the systematic study of the enhancement of the magnetic properties of two type of magnetic materials within the shape of thin films, (ferromagnetic and ferrimagnetic materials), by using nano-patterned systems of antidot arrays. The competition between the intrinsic and shape anisotropy together with the local effects induced by the antidots creates new scenario to engineer and tailor the magnetic properties of the magnetic thin films by modifying their geometrical parameters. Special focusing in the magnetic anisotropy for both directions, the in-plane and the out-of-plane, have done to find possible application in spintronics and bit-patterned magnetic recording media. In order to exploit the magnetic properties of the antidot arrays and applying them

instead of the continuous thin film, the magnetic properties with different geometrical features must be deeply known. In addition, micromagnetic domain structure study has been done with micromagnetic simulation to investigate and analyse the effect of geometrical parameters on magnetic domain structure.

The presented nanoporous alumina membrane, NPAM, has exceptional features for the purposes of this work such as low cost, the reproducibility of the samples, the relatively easy manipulation of the geometric properties and the desired nano-dimensions. Besides, these alumina membranes display long-range porous area, in which the controlled pores diameter are of few tens of nanometres and are hexagonally arranged within geometric domains of micrometric size. The total effective area is of the order of $cm^2$.

The engineering of the geometric properties of the NPAM is the keystone of this work, by using electrochemical processes. The well-equipped laboratory at (Scientific and Technical Services of the University of Oviedo), holds the necessary conditions to obtain a big amount of nanoporous alumina templates with a wide range of different pore diameters varied between 32±2 to 93±1 nm, but keeping constant the interpore distance, $D_{int}$, to the value of 103±2 nm, within the scope of this study (see Fig.3.2). The fabrication technique behind these systems is chemical in origin, which together with physical deposition method, i.e. thermal evaporation, consisted in a bottom-up method.

# Chapter 3: Preparation and characterization of antidot arrays

In this Chapter, an overview of the experimental techniques concerning fabrication and characterization of antidot samples are presented. It is divided in three parts: i) fabrication techniques, ii) topography and structural characterization and iii) magnetic characterization. The work of this study focusses on improvements in the characteristics of the nanoporous alumina templates aiming tailored magnetic properties. The experimental techniques are described making special emphasis in those involving our most active work.

## 3.1 Preparation of antidot arrays thin films

### 3.1.1 Nanoporous alumina templates fabrication

In brief, the initial samples consist of 0.5 mm thick, high purity Al foils (99.999%, Goodfellow, Huntingdon, UK) that were cleaned by sonication in ethanol and isopropyl alcohols and electropolished at 20 V in perchloric acid and ethanol solution (1:3 vol., 5 °C) for 5 min see (Fig.3.1a). These polished Al foils were then employed as starting substrates for the anodic synthesis of nanoporous alumina templates through mild anodization process. The two-step electrochemical anodization was performed in 0.3 M oxalic acid, at a temperature range between 1 and 3 °C and under a potentiostatic applied voltage of 40 V, measured versus a Pt counter electrode. Between the two anodization steps, the alumina samples were immersed in 0.2 M $CrO_3$ and 0.6 M $H_3PO_4$ aqueous solution. This chemical etching step allowed for the selective removal of the first grown anodic alumina layer, which contained randomly disordered nanopores at its top surface see (Fig.3.1b). During the second anodization step, which lasted for 5 h, the nanopores grew following the highly self-ordered hexagonal symmetry pre-patterned engineering

during the first anodization process as sketched in (Fig.3.1c, d). To obtain alumina templates with different pore size, the samples were chemically etched in 5 wt.% orthophosphoric acid at 30 °C, for different etching times, $T_{etching}$, that were varied between 5 and 53 minutes. This procedure allowed us to obtain a great variety of nanoporous alumina templates with a wide range of different pore diameters ranging between 32±2 and 93±1 nm, but keeping constant the interpore distance, $D_{int}$, to the value of 103±2 nm see (Fig.3.2).

Fig. 3.2 summarizes the evolution of the alumina membrane pore diameter as a function of the etching time for the pores widening chemical etching. A linear relationship is found between the pore diameter and $T_{etching}$ with an inflection point for ($T_{etching}$= 37.5 min), at which the rate of the pore size increases with etching time changes. The Al oxide of pore wall removed in the early stage is etched at a higher rate ($T_{etching}$ < 37.5 min with slope = 1.14), than that in the later stage ($T_{etching}$ > 37.5 min with slope = 0.95). The retarded rate of chemical etching in the later stage can be attributed to the relatively more pure Al oxide nature of the inner pore wall, as compared to the less dense Al oxide of the outer pore wall due to the incorporation of anionic species [82]. The linearity of pore diameter increasing with pore widening time has been already previously described for many studies [38,77,83]. By increasing the pore diameter of alumina membrane and keeping constant $D_{int}$, this distance is reduced down to its minimum value. Consequently, the pore diameter reaches a maximum value for a network with a fixed $D_{int}$ parameter, around pore diameter = $D_{int}$ ≈ 103 nm. Here, the maximum pore diameter value reaches ≈ 93 nm, indicating that the stabilization of the hexagonal network is stable up to 90.3% of the maximum value for pores of the alumina membrane. This value here reached is higher than the ones previously obtained in the literature with similar techniques [41,84–86].

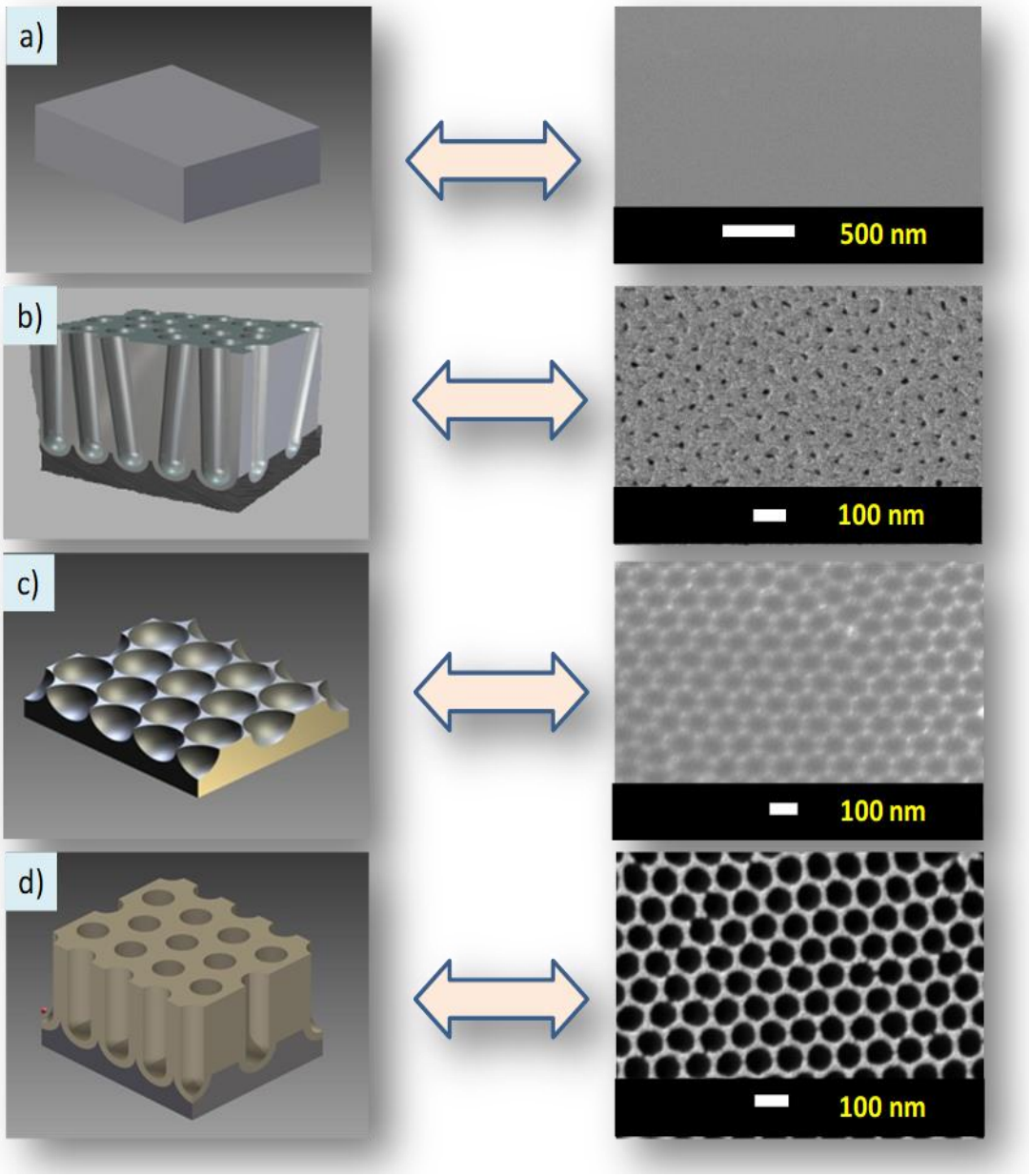


**Figure 3.1:** The steps for obtaining the nanoporous alumina membrane and related SEM images for each step. (a) first one starts from an electropolished Al surface; (b) scheme of a nanoporous alumina membrane after first anodization process with random nucleation of the pores in the top-surface; (c) Al foil after removing the first anodized alumina revealing the engraved hole structure; (d) nanoporous alumina membrane after the second anodization process with hexagonal self-ordered pattern of nanoholes.

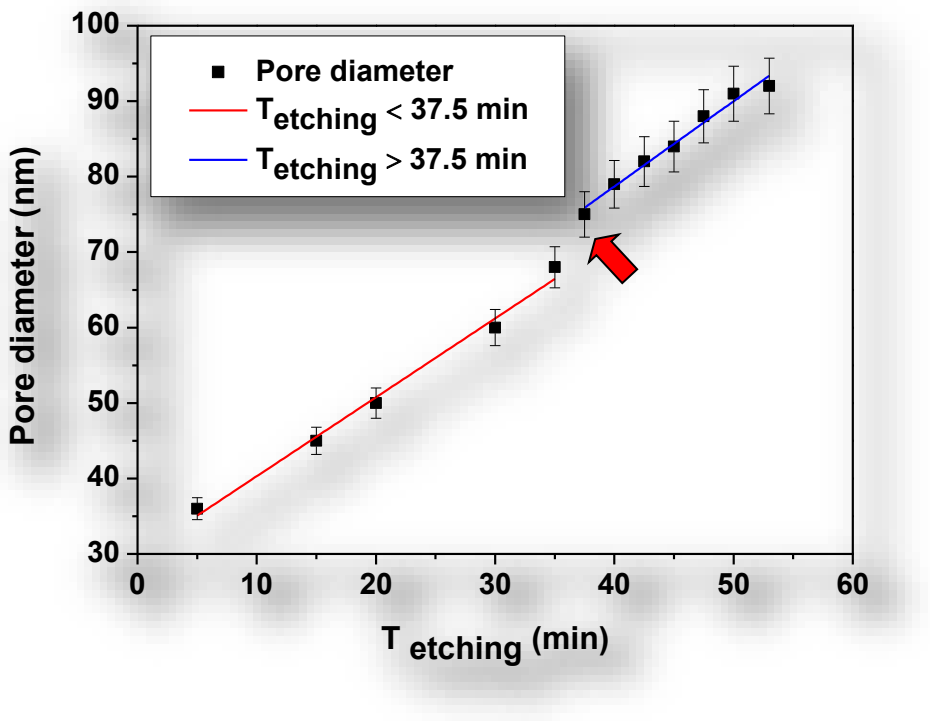


**Figure 3.2:** Pore diameter of alumina membrane versus etching time $T_{etching}$ during the pore widening procedure of the alumina templates. The red arrows indicate the inflection point at $T_{etching}$= 37.5 min.

### 3.1.2 Thin film deposition by thermal evaporation system

The controlled deposition of the metallic thin film formed by highly pure metal pieces of magnetic materials (99.999%) was performed in a high vacuum thermal evaporation technique using an E306A thermal vacuum coating unit (Edwards, Crawley, UK) with an ultimate vacuum better than $4.1\times10^{-7}$ mbar, having a diffusion pump backed by rotary pumping together with a liquid nitrogen trap as sketched in Fig. 3.3a [77]. The pure element of magnetic metal pieces was placed inside a water-cooled copper crucible and heated by the action of magnetically focused electron ion-beams. The evaporated target metal was deposited on the top-surface of the hexagonally ordered nanoporous alumina membranes, which acted as templates to obtain the thin film antidot arrays, as depicted in Fig. 3.3 b [38]. The control of the film thickness was achieved by using two

independent quartz crystal controllers that monitored simultaneously and independently the deposition rates of each evaporation source. The source to substrate distances were maintained constant at about 18 cm. The deposition rate was around 0.10–0.15 nm $s^{-1}$.

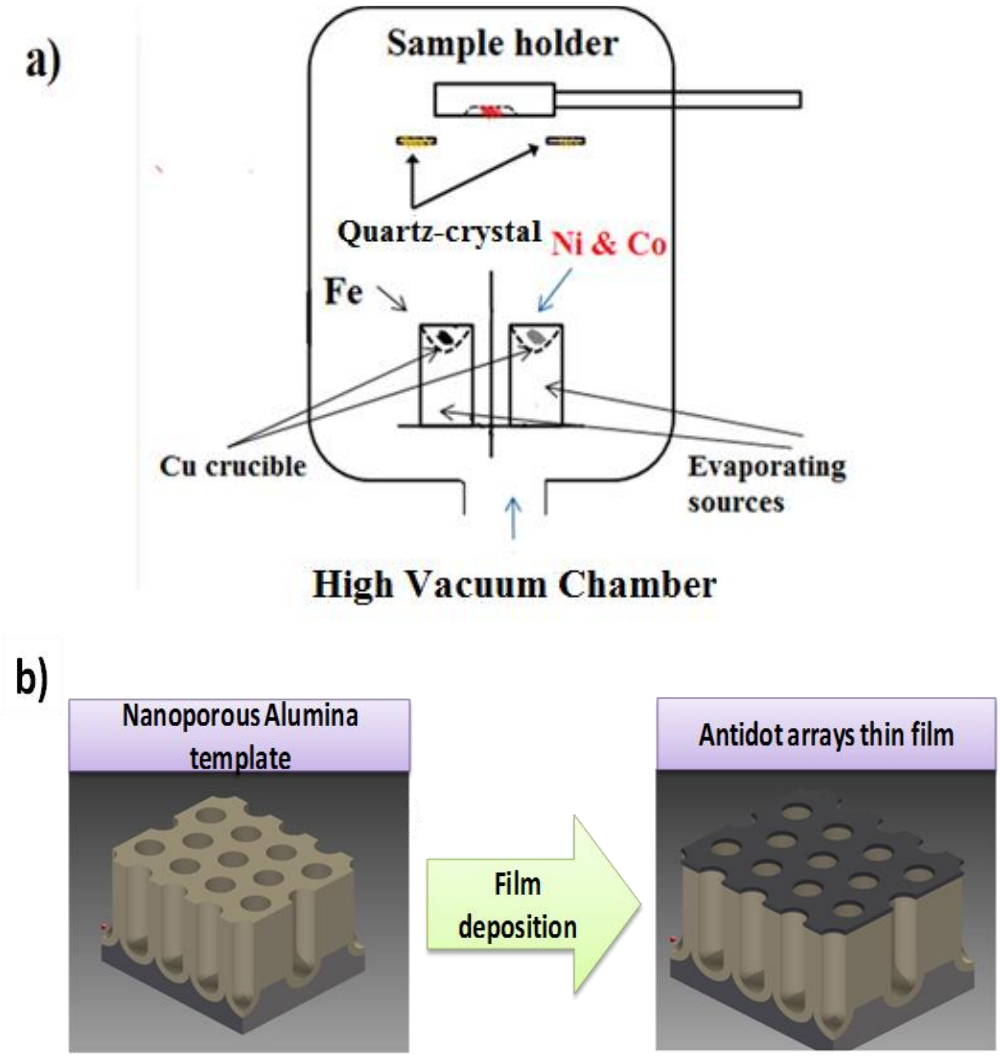


**Figure 3.3:** a) Sketch of the thermal evaporating system. b) Deposition film on top-surface of the nanoporous alumina membrane.

## 3.2 Morphology and micro-structure characterization

### 3.2.1 Scanning Electron Microscope

The surface morphological characterization of the Ferromagnetic and Ferrimagnetic antidot arrays samples have been carried out mainly by Scanning Electron

Microscopy (SEM) (JSM 5600, JEOL, Akishima, Tokyo, Japan). This technique not only allows studying the micro and nano-structure of the samples, but also allows obtaining information on the chemical composition and homogeneity of the samples. The operation of the SEM is based on the interactions between the surface of the sample and the electron beam that runs through it in a sweeping/scanning mode (as seen in Figs. 3.4 a and 3.4b).

The SEM uses the detection of the secondary electrons to produce the images. The generated secondary electrons depend on the energy of the incident beam, material and the surface of the sample. In the SEM images, the contrast is due to the morphology of the sample or due to a different compound in the sample. The resolution of the image obtained ranges between 3 and 20 nm.

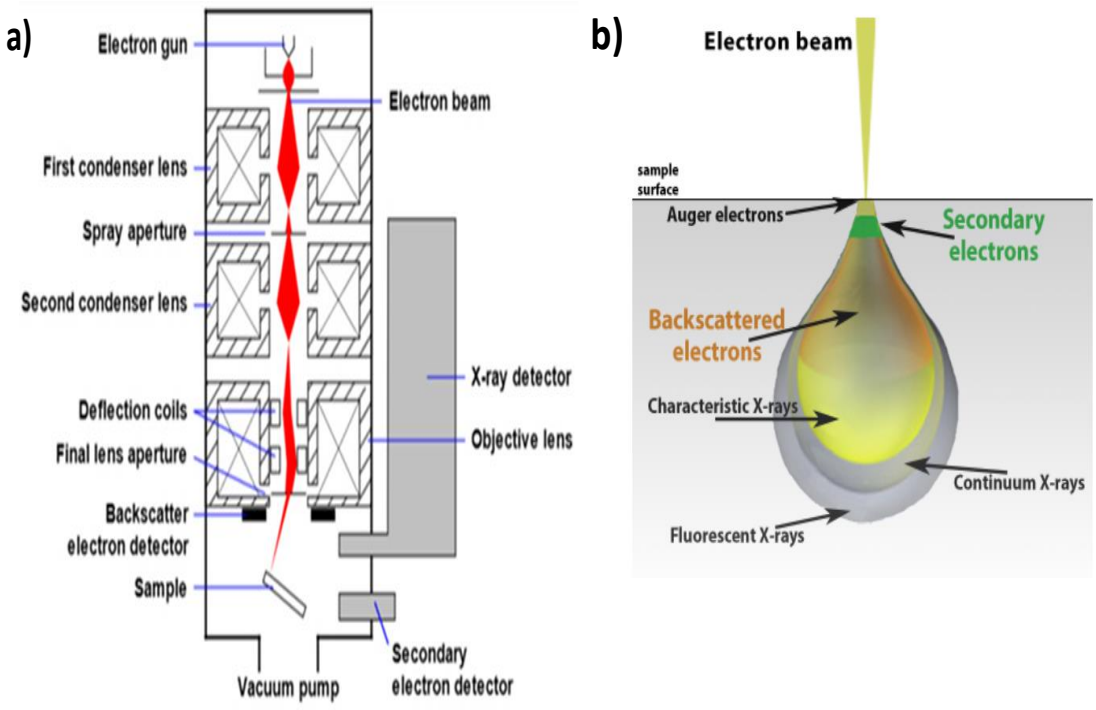


**Figure 3.4**: a) Schematic of a Scanning Electron Microscope and b) Schematic of electron beam interaction [87].

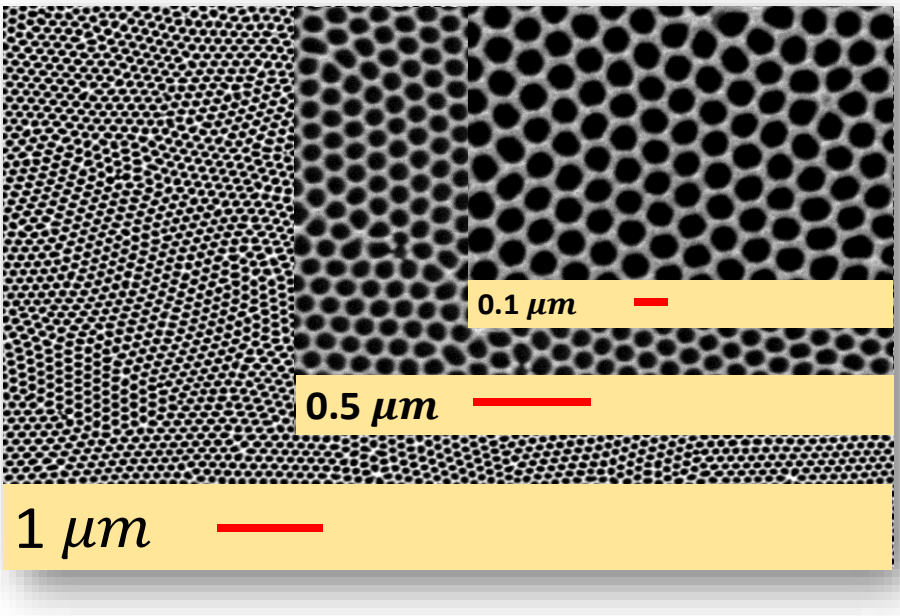


**Figure 3.5:** SEM image of the antidot arrays thin films with hole diameter, d = 85 nm, and interpore distance, $D_{int}$ = 105 nm, with different magnifications: 1 μm, 0.5 μm and 0.1 μm.

Figure. 3.5 shows an example of the SEM images obtained with different magnification scale. In the specific case of the nanomaterials synthesized and presented in this thesis, its topographic and compositional characterization has been carried out using a commercial model of SEM, (JSM 5600, JEOL, Akishima, Tokyo, Japan) which is allowable at Scientific and Technical Services of the University of Oviedo.

### 3.2.2 Energy Dispersive X-Ray Spectroscopy

Chemical information of particular samples was obtained by Energy Dispersive X-Ray Spectroscopy (EDS). Overall, the high energy of an incident beam ionizes the atoms then the X-ray photons are emitted; the energy of these photons is characteristic for each element (X-ray fluorescence). The EDS detector was embedded in a Field Emission Scanning Electron Microscopy and carried out using a commercial model of SEM, (JSM 5600, JEOL, Akishima, Tokyo, Japan) allowable at Scientific and Technical Services of the University of Oviedo.

### 3.2.3 Atomic Force Microscopy technique

The Atomic Force Microscopy, AFM, technique is a high-resolution (fractions of a nanometer) scanning probe microscope. The AFM consists on a cantilever with a sharp tip (probe) at its end used to scan, in this work, the thin films so as the antidot arrays sample surface. The interaction between the tip and the sample suface originates a deflection of the cantilever, measured through the deflection of an incident laser beam [88].

Two different modes can be used in the AFM system: contact mode, where the repulsion force between the tip and the sample is kept constant; and the dynamics mode, where the cantilever vibrates at resonance frequency and the amplitude is used as the feedback parameter. The tip can generate artifacts in the images, so a special care must be taken in the analysis of the results. The system used is a Cervantes system from Nanotec Electrónica at the Materials Science Institute of Madrid-CSIC. From the AFM images, the average size of the in-plane crystals were measured by the calculus of the "auto-correlation" [89]. This operation evaluated the integral convolution of a multiplied photo by itself, with a certain displacement in the axes X and Y. The auto-correlation image G is defined as:

$$G(K_1, K_2) = \sum f(x,y) f(x + K_1 y + K_2) \qquad (3.1)$$

where f (x,y) is the initial image, and $k_1$ and $k_2$ is the displacement in the axes X and Y respectively, with respect to the center of the image [89].

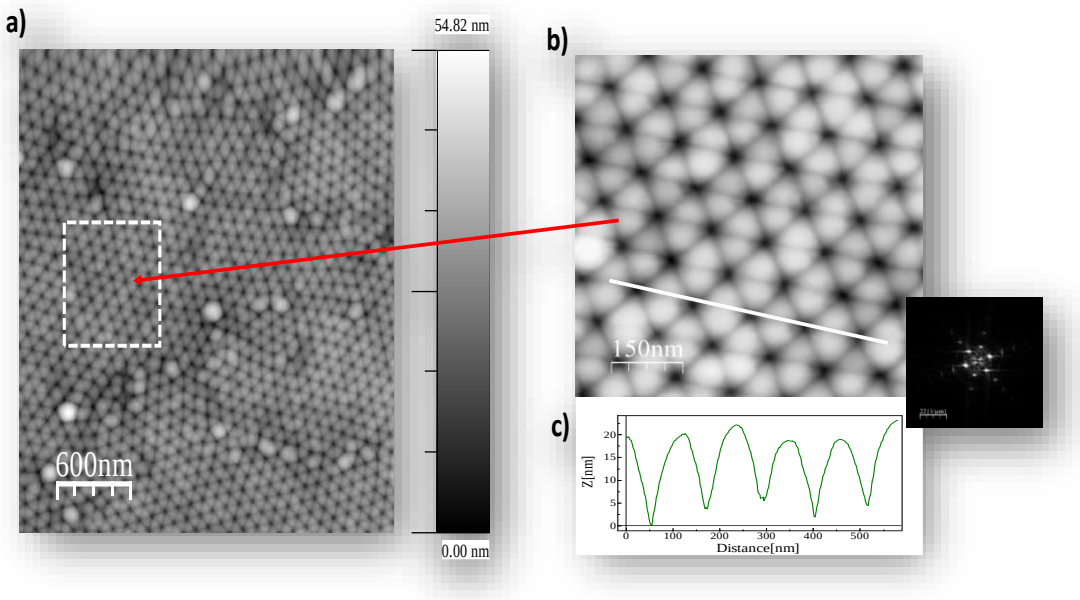


**Figure 3.6:** (a) AFM image corresponding to the topography of the Dy-Fe alloy antidot sample with 30 nm in thickness. (b) Image magnifications corresponding to the marked region in (a). Insets correspond to the FFT of each image. (c) AFM profiles obtained along the marked lines in (b).

Figure 3.6 shows the AFM image of the surface topography for the Dy-Fe antidot sample, with thickness of 30 nm. The nanometric hole structure of the magnetic film is clearly visible and replicates the hexagonal geometry of the nanoporous alumina membrane used as template. From the profile scan in (Fig.3.6 c), as well as from the FFT data shown in the inset of (Fig.3.6 b), the lattice constant of the hexagonal antidot arrangement is estimated to be around 110 nm. The AFM characterizations of antidot thin films shown in this thesis were performed by Dra. Agustina Asenjo from the Nanomagnetism and Magnetization Processes Group (GNMP) led by Prof. M. Vázquez at the Materials Science Institute of Madrid ICMM-CSIC.

### 3.2.4 Transmission electron microscopy

The operating principle of the Transmission Electron Microscope, TEM, is similar to that of the transmission optical microscopes, but it uses electrons instead of photons to

form the image. An outline of the principle of TEM operation is shown in Figure 3.7. Electrons are provided by an electron gun and accelerated by a high voltage (in the order of hundreds of kV).

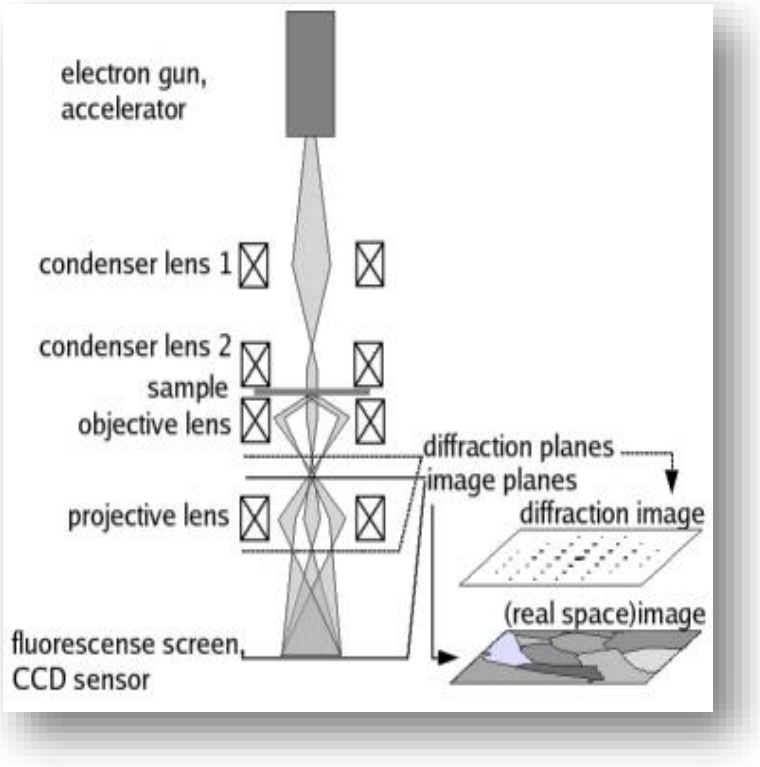


**Figure 3. 7**: Diagram of a transmission electron microscope.

The main difference with respect to the SEM is that in the TEM the electrons pass through the sample and are focused directly on a plate of a fluorescent material located at the base of the system as a screen. Also, the TEM allows the obtaining of images in the reciprocal space (electron diffraction images, SAED) that provide information on the crystalline or amorphous structure of the samples.

Since in the TEM microscopes the image is obtained by transmission mode, the sample must be sufficiently thin to allow to pass through it an appreciable amount of electrons. Depending on the atomic number of the material being studied and the energy

of the electrons, the maximum allowed sample thickness is usually of the order of tens to hundreds of nanometers. In order to solve this problem in our case, the antidot arrays samples were separated from the substrate, membrane or template that served as a support during its manufacture and then suspended in ethanol in the form of thin films to allow its observation.

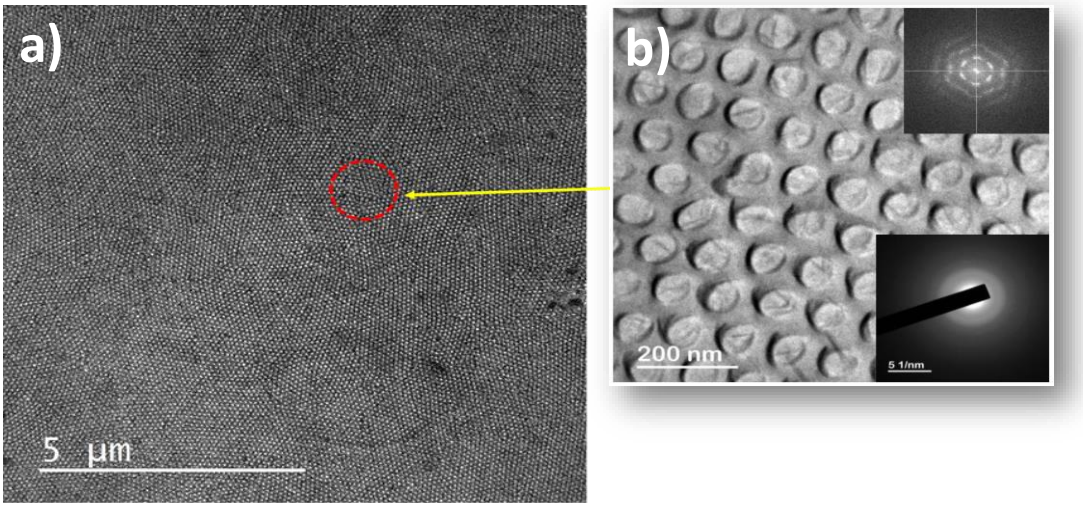


**Figure 3.8:** a) TEM image of antidots thin film after being released from the nanoporous alumina template. b) The FFT analysis shown in the upper inset reveals the highly hexagonal ordering degree of the antidots by replicating the nonporous structure of the patterned alumina membrane, while the electron diffraction pattern (SAED) displayed in the lower inset demonstrates the amorphous character of the deposited $Dy_{13}Fe_{87}$ alloy.

TEM micrograph of the Dy-Fe antidots thin film released from the nanoporous alumina membrane, which are displayed in Figure 3.8, demonstrates that the nanometric holes successfully replicate the structure of the highly hexagonal self-ordered nanoporous alumina template. The Fast Fourier Transform (FFT) shown in the upper inset of Fig. 3.8b, which is characteristic of a system with hexagonal periodic symmetry, reinforces this observation. In addition, SAED spectrum, shown as the lower inset in Fig. 3.8b, indicates the amorphous structure of the $Dy_{13}Fe_{87}$ alloy, evidenced by the presence of diffused rings and the absence of clear spots in the electron diffraction spectrum. The morphological and structural studies performed by TEM presented in this thesis report

have been carried out in several transmission microscopes (JEOL 2000 EXIIand JEOL-JEM 2100F), belonging to the SCTs of the University of Oviedo.

### 3.2.5 Determination of geometrical and parameters of the antidot arrays

The magnetic properties of antidot samples strongly depend on the geometrical parameters of the array, namely the interpore distance, $D_{int}$, and the antidot hole diameter, d, as well as the nanohole ordering. An efficient way to determine these parameters uses an top-view SEM or TEM images of the antidot array of interest, as presented in Figure 3.9, as a starting point for the subsequent analysis.

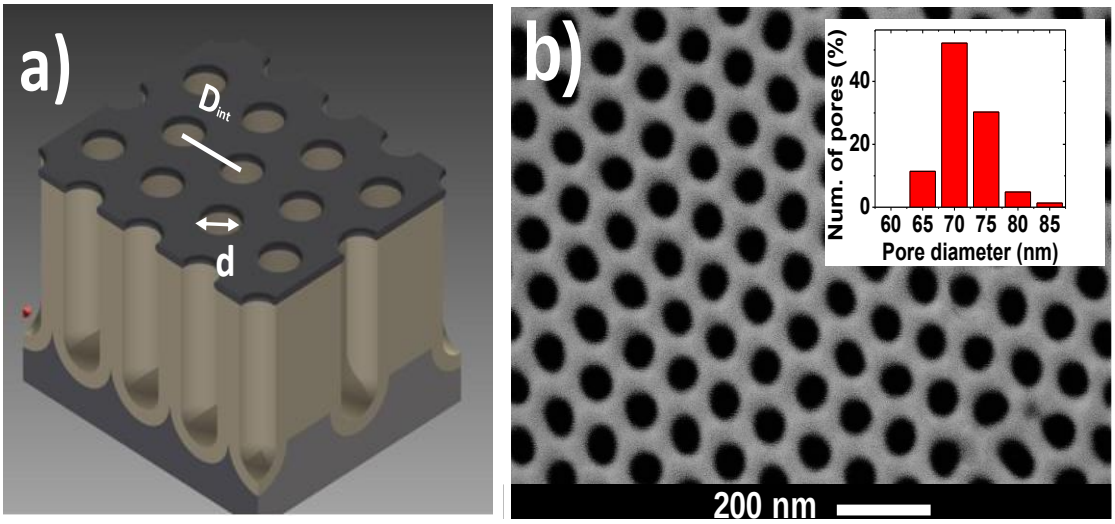


**Figure 3.9:** a) Three-dimensional sketch of antidot arrays thin film, where it is indicated the main geometrical parameters like the antidot hole diameter and the interpore distance. b) SEM image of a sample of antidot arrays. In the inset it can be seen the average pore diameter obtained with image J analysis.

In order to determine the hole diameters, the freely available software ImageJ, is used [90]. This software provides a routine which is able to identify the holes in the SEM micrograph ("Analyze Particles"). The threshold of the gray value. which associates a pixel to either thin film or hole can be adjusted. However, due to the clear contrast, this

setting has only a very minor influence on the results over a wide range of parameters, which makes the method very reliable.

## 3.3 Magnetic Characterization

### 3.3.1 Vibrating Sample Magnetometer: VSM

Most of studies on the volume magnetic characterization of CTF and antidot arrays samples presented in this work have been performed in a systematic way by using a Vibrating Sample Magnetometer (VSM-VersaLab, Quantum Design) equipped with superconducting coils that allow to apply a maximum magnetic field of ± 3 T measured in both, parallel (In-Plane, INP) and perpendicular (Out-of-Plane, OOP) directions to the film plane, respectively. Sensibility in the measurement of the magnetization in this equipment is less than $10^{-6}$ emu (effective value), which has proved sufficient in most of magnetic measurements of nanomaterials. The measurement temperature of the VSM-VersaLab can be adjusted in the range from 50 to 400 K, although the measurements performed in this work were carried out as a function of the applied magnetic field (magnetic hysteresis cycles) performed under isothermal conditions at room temperature (RT= 300 K). Figure 3.10 shows the operating scheme of a VSM. This technique, developed by Foner [91], is based on the change of magnetic flux in a coil when a magnetic sample vibrates near it. The sample is attached to one end of a rod which is placed in an area where a uniform magnetic field is created by an electromagnet, while the other end of the rod is attached to a mechanical oscillator which causes it to oscillate with a vibration frequency of the order of 40 Hz and with an oscillation amplitude of 0.1 to 5.0 mm. Around the sample are arranged the detection coils that measure the alternating electromotive force induced by the oscillatory movement of the sample and that is proportional to the magnetic moment of the sample.

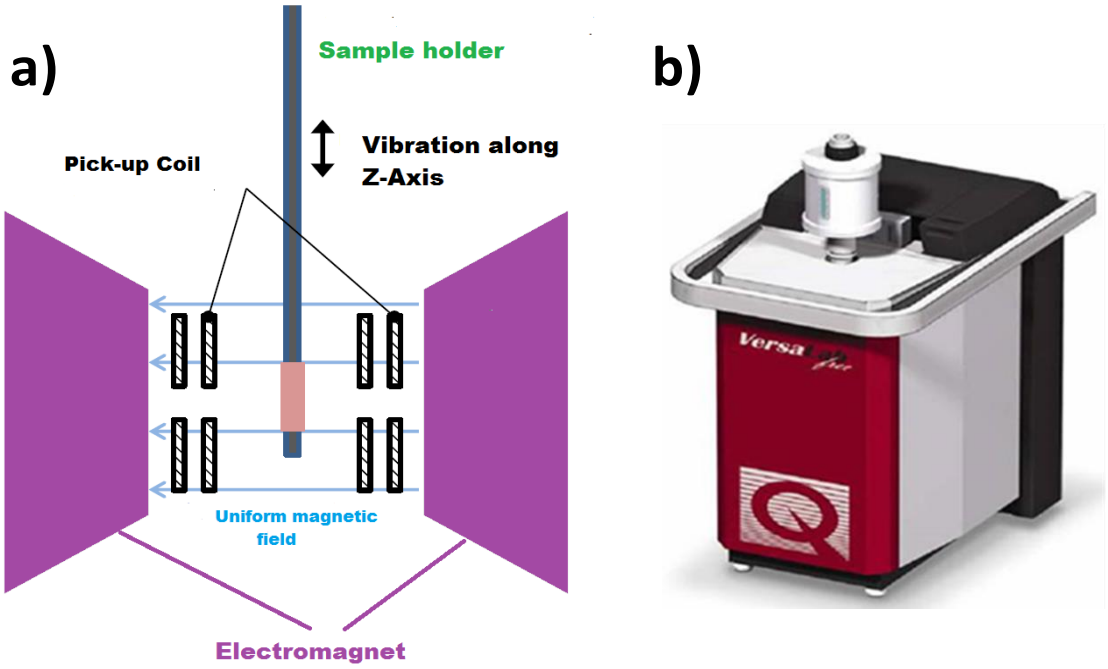


**Figure 3.10:** a) Schematic diagram of the operating mode of a Vibrating Sample Magnetometer and b) pictures in this image.

### 3.3.2 Magnetic Force Microscopy

The Magnetic Force Microscopy, MFM, is a Scanning Probe Microscope that maps the magnetic spatial distribution by the interaction between the tip and the sample. The MFM works in the dynamical mode with a magnetic tip (a standard AMF tip that is coated with a magnetic layer) [92]. The system is able to detect not only the atomic forces between the sample and the tip but also the magnetic interaction [93,94] The force between the sample and the tip is given by:

$$\vec{F} = (\vec{m}\cdot\nabla)\vec{H} \qquad (3.2)$$

where $\vec{m}$ is the magnetic moment of the tip and $\vec{H}$ is the magnetic field applied to the sample. The magnetic moment of the tip can affect the magnetic state of the sample, so the accurate kind of tip should be selected regarding the magnetic properties of the samples. The control detects the changes in the resonance frequency on the cantilever, which is induced by the magnetostatic interaction between the tip and the sample.

Generally, the tip has an OOP component of the magnetic moment, so the MFM signal corresponds mainly to the out-of-plane magnetization component/contribution of the sample. The MFM signal is related to the orientation of the magnetization along the sample. The resulting image consist of white color (repulsing interaction), for the magnetic moments of the domains that are in antiparallel direction relative to the magnetization of the tip; black color (attractive interaction), when the magnetic moments are parallel to the magnetization state of the tip sample; and grey color adscribed to the magnetic moments that are perpendicular to the moments of the tip (parallel to the plane of the sample). The study of the magnetic domain structure of the antidot sample surface was performed with a Magnetic Force Microscopy from Nanotec Electrónica [88]. The probes are commercial Nanosensors PPP- LM-MFMR cantilevers with a force constant of 2.8 N/m and a resonance frequency of 75 kHz. Before the experiment, the probes are magnetized along their pyramid axis. As usual procedure in AFM/MFM characterization, two images were recorded simultaneously, the topography, obtained at small tip–sample distance, and the frequency shift, which is obtained at a retrace distance of 30 nm.

### 3.3.3 Magneto-optical Kerr effect Magnetometer: MOKE

The use of Magnetic-Optical Kerr Effect Magnetometry, MOKE, technique has allowed the study of the surface magnetic behavior of antidot arrays thin films. This measurement technique is based on the interaction of a linearly polarized laser light beam and the magnetic material under investigation.

When a linearly polarized light beam is reflected in an immersed medium, the reflected beam has an elliptical polarization state (Kerr ellipticity) and undergoes a rotation of the polarization axis direction with respect to the polarization axis of the incident beam (Kerr rotation). These changes are proportional to the magnetization of the

medium. Depending on the sample relative orientation (palarell or perdicular to its plane) , the magnetization of the sample and the polarization plane of the incident light, three variants of the Kerr effect can be distinguished: polar, longitudinal and transversal (see Figure 3.11).

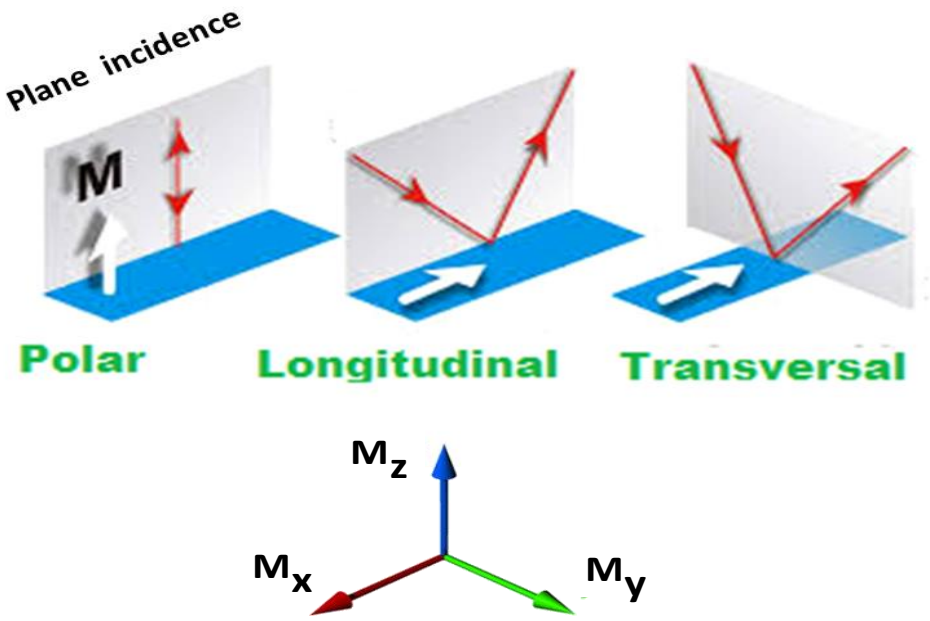


**Figure 3.11**: Schematic representation of MOKE geometries of measurement.

In the longitudinal configuration, the magnetization vector is parallel to both the reflection surface and the plane of incidence. The linearly polarized light incident on the surface becomes elliptically polarized after reflection; the change in polarization is directly proportional to the component of magnetization. Longitudinal geometry, within a first order approximation can provide information on the magnetization components $M_x$. In this case, both s- and p-polarized light produce a small rotation on the polarization plane of the reflected light, which depends on the magnetization of the sample.

In the transverse configuration, the magnetization is transversal to the plane of incidence and parallel to the surface. In this case, instead of measuring the Polarization of the light after reflection, the reflectivity is measured. This change in reflectivity is

proportional to the component of magnetization that is transversal to the plane of incidence and parallel to the surface, $M_y$. In this case, if the light is p-polarized, the electric field is parallel to the incidence plane, so the magnetic field is transversal to the incidence plane (parallel to the magnetization vector of the sample), as can be seen in Figure 3.11. Thus, the electric field of the light interacts with the orbital momentum of the electrons, giving rise to Kerr effect. The coupling L-S (angular momentum and spin momentum) is the responsible of the magnetic moment.

In the polar Kerr effect, the magnetization vector is perpendicular to the reflection surface and parallel to the plane of incidence. Polar geometry, within a first order approximation can provide information on the perpendicular magnetization component $M_Z$ to the sample plane. In this case, as in the longitudinal configuration, both s- and p-polarized light produce a small change on the polarization plane of the reflected light, which depends on the magnetization of the sample.

The MOKE measurements presented in this thesis were carried out on a NanoMOKE-3® magnetometer (Durham Magneto Optics Ltd., Durham, UK) belonging to the SCTs of the University of Oviedo. The schematic diagram and a picture of this measurement device is shown in Figure 3.12. The NanoMOKE-3® magnetometer being able to apply up to 0.125 T by using the quadrupole electromagnet option or 0.5 T, with the dipole electromagnet optionis matched with p-polarized laser beam and it is sensitive to the longitudinal (L-MOKE), transversal (T-MOKE), and polar (P-MOKE) components.

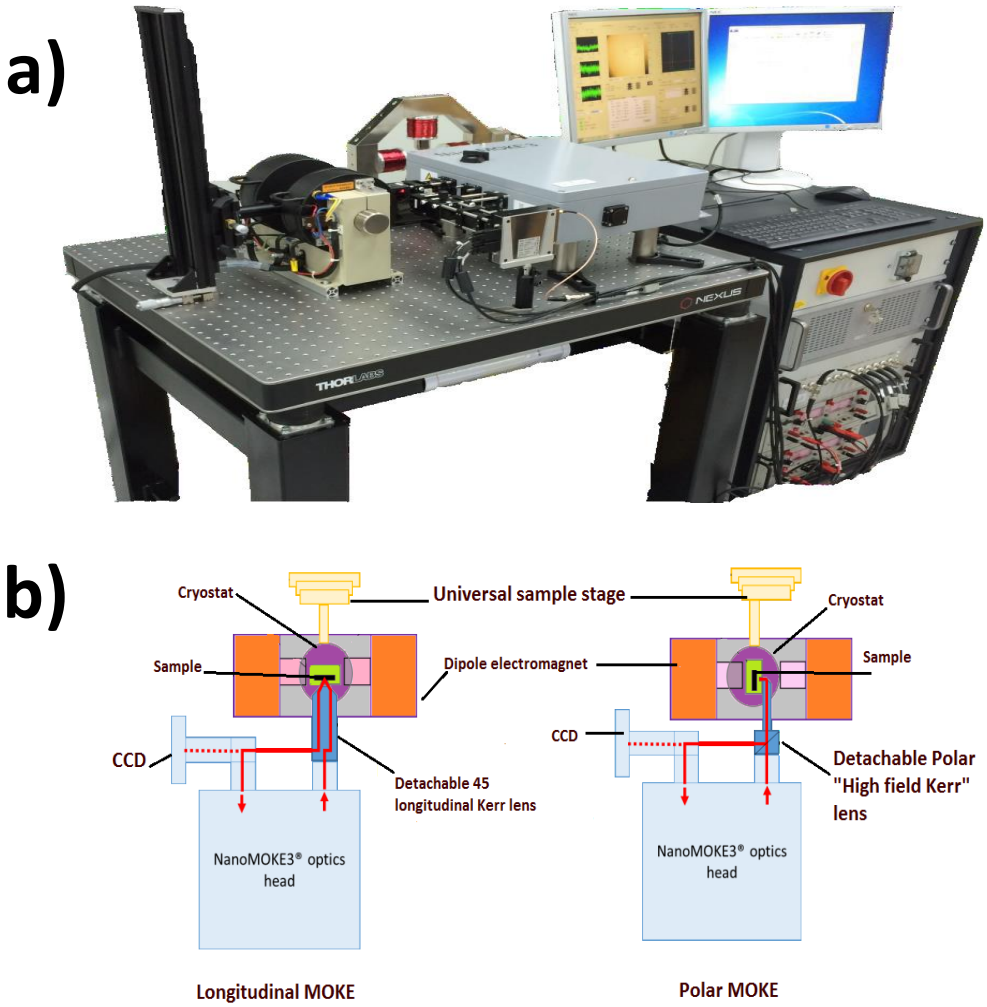


**Figure. 3.12:** a) picture of a NanoMOKE3® magnetometer and b) schematic diagram of the operating system.

### 3.3.4 Finite Element Micromagnetic Simulations by Mumax$^3$ software

Micromagnetic simulations provide detailed insight into the magnetization behavior of a magnetic system. There are several software solutions freely available in the market. Micromagnetic simulations of antidot arrays with different pore diameter have been performed in this thesis by using the GPU-accelerated Mumax$^3$ software. It allows calculating the space- and time-dependent magnetization dynamics in nano- to micro-sized ferromagnets using a finite-difference discretization. Mumax$^3$ is open-source software written in Go and CUDA and is freely available under the GPLv3 license on

[95]. This software package allows the calculation of the temporal evolution of the reduced magnetization based on the modified Landau-Lifshitz-Gilbert-Slonczewski (LLGS) equation of movement for the magnetization, $\overrightarrow{m}((\vec{r}),t)$. Its time derivative has to consider three contributions: Landau-Lifshitz torque, Zhang-Li spin-transfer torque and Slonczewski spin-transfer torque. A finite difference discretization allows for the magnetostatic field to be evaluated as a discrete convolution of the magnetization [96]. Figure 3.13a displays an example of a hysteresis loop of Ni antidot arrays with d = 60 nm and $D_{int}$ = 105 and Figure 3.13b shows the image of magnetic domain structure at remanent state.

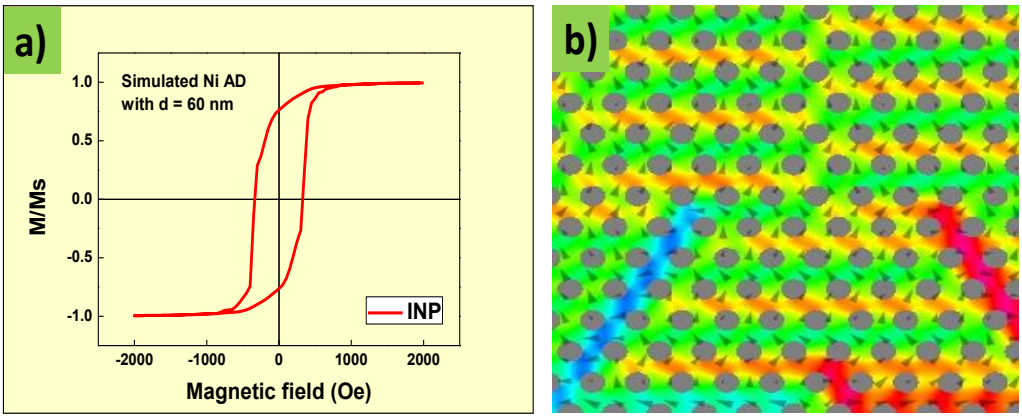


**Figure. 3.13:** a) Simulated hysteresis loop of Ni antidot arrays with hole diameter around 60 nm and interhole distance of 105 nm. b) Simulated magnetic domain structure at remanent state for the same antidot sample.

# Part I: Ferromagnetic Antidot Arrays

# Chapter 4: Dependence of magnetization process on layer thickness of Ferromagnetic antidot arrays

In this Chapter, the magnetic properties of hexagonally ordered antidot arrays made of Fe and Co are studied and compared with corresponding ones of continuous thin films with the same layer thicknesses, varying between 10 nm and 100 nm. Both samples, the continuous thin films and antidot arrays, were prepared by high vacuum e-beam evaporation of the alloy on the top-surface of glass and hexagonally self-ordered nanoporous alumina templates, which serve as substrates, respectively as described in the experimental part 3.1.1 and 3.1.2. A noticeable change in the magnetic properties has been observed by modifying the antidot layer thickness.

## 4.1 Morphological characterization of antidot thin film samples.

The morphological characterization of the samples is performed by means of (SEM) (JSM 5600, JEOL, Akishima, Tokyo, Japan) images. The resulting lattice parameters of the so synthesized nanoporous alumina membrane which employed as a starting template for the thin film deposition are around 85±3 nm of pore diameter and 104±2 nm of the interpore distance, $D_{int}$. Fig. 4.1(a to i) shows the SEM images of Fe antidot arrays with hexagonal symmetry. We should point out that as the thickness of the film increases, the diameter of the nanoholes reduces due to the deposition of magnetic material in the top of the hole until it closed to tally at layer thickness 100 nm (Fig. 4.1h).

Fig. 4.2 shows the correlation between the resulting nano-holes diameters, d, and the edge-to-edge antidot distance, $W = D_{int} - d$, with the antidot layer thickness, t, of the Fe antidots same result obtain for Co antidot arrays. This change in the nano-hole diameter is due to the deposition of magnetic material in the upper part of the wall of the pore. From Fig. 4.2 we can distinguish two regimes depending on the edge-to-edge

antidot distance value. One for W is smaller than the antidot hole diameter i.e. (thinner samples) and later for W is bigger than antidot diameter i.e. (thicker film).

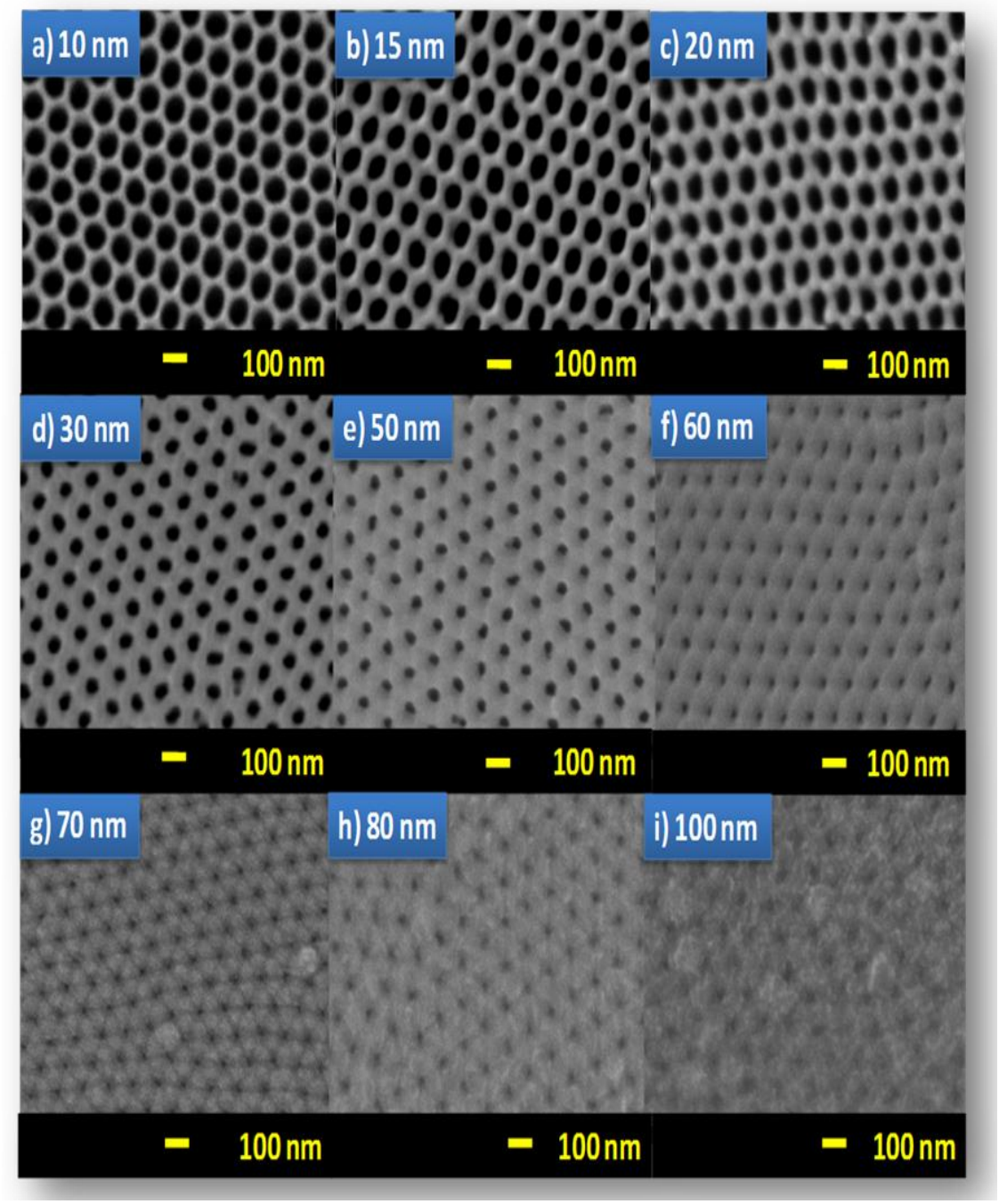


**Figure 4.1:** SEM top-view surface of Fe antidot thin films with thicknesses ranging from 10 nm up to 100 nm. Scale-bars indicate 100 nm.

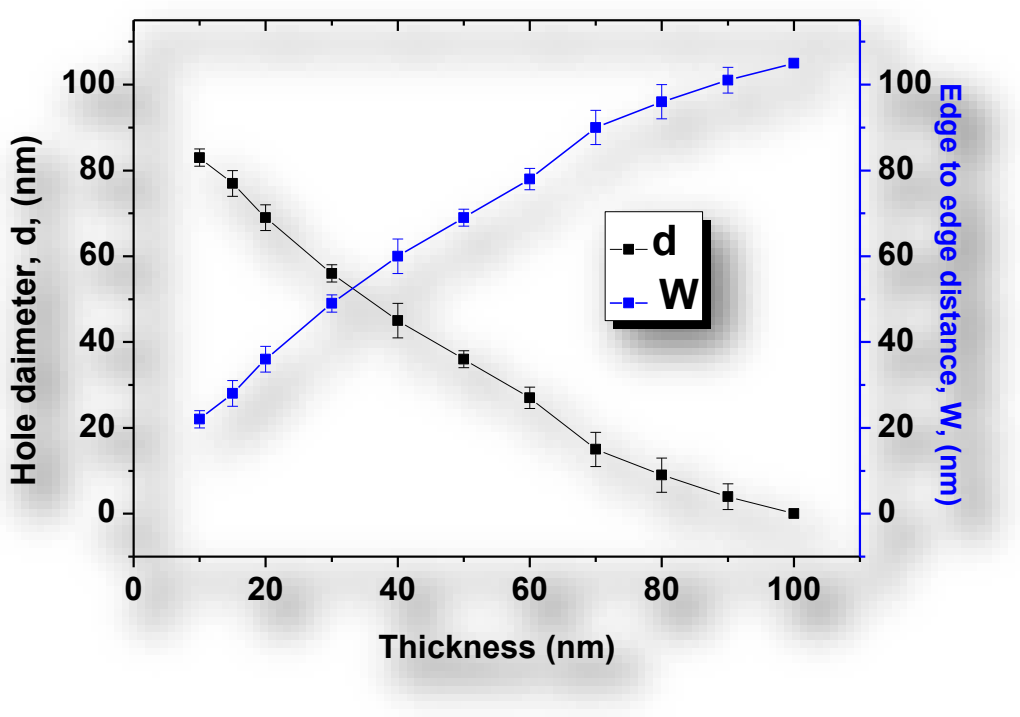


**Figure 4.2:** Dependence of the resulting nanoholes diameter, d, and the edge-to-edge antidot distance, W, of the Fe antidot arrays with the film thickness grown.

## 4.2 Magnetic properties of Fe thin films and antidot arrays

Magnetic properties of Fe and Co antidot arrays, AD, and their corresponding continuous thin films, CTF, have been determined through the hysteresis loops at room temperature by the magneto-optical Kerr effect (MOKE) with magnetic field applied up to ± 0.50T, using the NanoMOKE-3 magnetometer, (Durham Magneto Optics Ltd.). In addition, we also obtained hysteresis loops using vibrating sample magnetometer, (VSM-QD-Versa lab) with applied magnetic field to ±3T. The magnetic field is applied in the plane of the film, INP, and perpendicular to the plane (out-of-plane), OOP, directions.

Hysteresis loops were obtained for both types of samples CTF and AD films. By rotating the samples every 5 degrees at film plane; we can get the MOKE hysteresis loops, with magnetic field parallel to the plane of the sample. To avoid the translation movement due to the sample rotation we first identified a feature or particle on the sample surface

using the scanning laser microscopy option of Nano-MOKE. Then we start measurement at a well-controlled position located at fixed distance which is about 10 µm from this point. Therefore, we correct the sample translation that happen because of stage rotation for every measurement angle by using the same procedure.

### 4.2.1 Magnetic characterization of continuous thin films

The Fig. 4.3 (a, b) show the INP MOKE hysteresis loop of selected Fe CTF with thickness range from 15 nm. A clear in-plane uniaxial anisotropy has been observed for all CTF samples, where the in-plane coercivity, $H_C$, angular dependence shows two-fold symmetry. This uniaxial anisotropy appears because of the angle incidence of the evaporation beam in the substrate which performed a residual stress on the surface of the film after the deposition, or dispersion of magnetic field used to focus the electron used for the materials heating [77,97]. Therefore, we called this anisotropy ¨induced intrinsic anisotropy¨ of CTF, which is, in turns, induced during the thin film deposition. Its values range from $3\times10^7$ to $8\times10^7$ (erg/cm$^3$). Also, this in-plane intrinsic anisotropy is found for all continuous thin films from 10 to 100 nm and it flow two-fold symmetry.

The thickness dependent roughness is strongly related to the film growth modes and the type of material being deposited. For the same film thickness, the rougher the surface the larger is the coercivity [98]. Consequently, by increasing the film thickness, $H_C$ rises due to the surface roughness and grain size increase, which results in an increase of the magnetic shape anisotropy for these thin films [99]. This observation agrees well with our experimental data, as shown in Fig. 4.4. The thickness of the Fe continuous thin film, CTF, increases from 10 up to 100 nm, giving rise to in-plane $H_{C//}$ values between 68 and 160 Oe, respectively. Therefore, the magnetic behavior is dominated by the layer

thickness of the Fe thin films, where the larger coercivity is obtained for the thin film with the higher thickness.

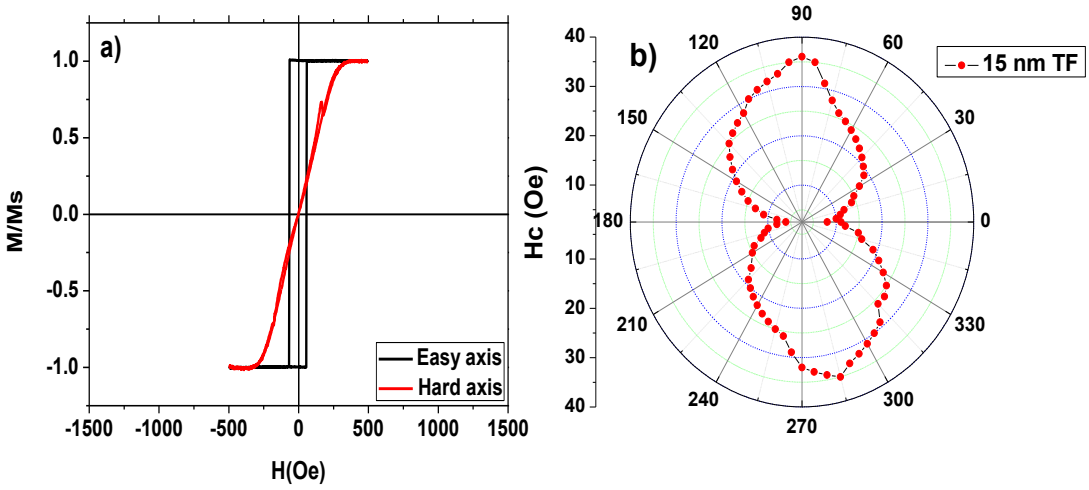


**Figure 4.3**: a) In-plane hysteresis loops of Fe continuous thin film and b) related INP angular coercivity dependence for samples with layer thickness 15 nm.

### 4.2.2 Magnetic characterization of antidot arrays thin films

The in-plane surface magnetic properties of Fe and Co antidot arrays, AD, samples with pore diameter 60 nm and interpore distance 105 nm and layer thickness 25 nm are plotted in the Fig. 4.5. Several differences in the in-plane magnetic properties of Fe and Co antidot have been found comparing to their corresponding CTF. Firstly, the nanostructuring significantly affects the shape of hysteresis loops and drastically changes the magnetic behavior. As it can be seen in Fig. 4.5, a magnetic anisotropy with in-plane easy magnetization direction is derived for Fe and Co antidots arrays due to the nanoholes induce a strong local shape anisotropy that tends to align the magnetization parallel to their edges [100]. The intrinsic nature of such in-plane magnetic anisotropy is due to the shape of the specimens. Consequently, in-plane magnetization process is due to domain wall displacements giving rise to hysteresis loops with high squareness (S) ratio, while magnetization rotation processes are responsible for the out-of-plane magnetization

reversal direction [77,80,93]. In addition, the $H_C$ (θ) angular dependence show four-fold symmetry for thinner antidot samples where d > W, meanwhile the AD samples with d < W show two-fold symmetry like the CTF as plotted in Fig. 4.5c and Fig. 4.5d, respectively. The change in $H_C$ for the AD samples can be due to the competition between the intrinsic anisotropy and the shape anisotropy, which is induced by nanoholes. Thus, the shape anisotropy decreases with increase the layer thickness of AD samples.

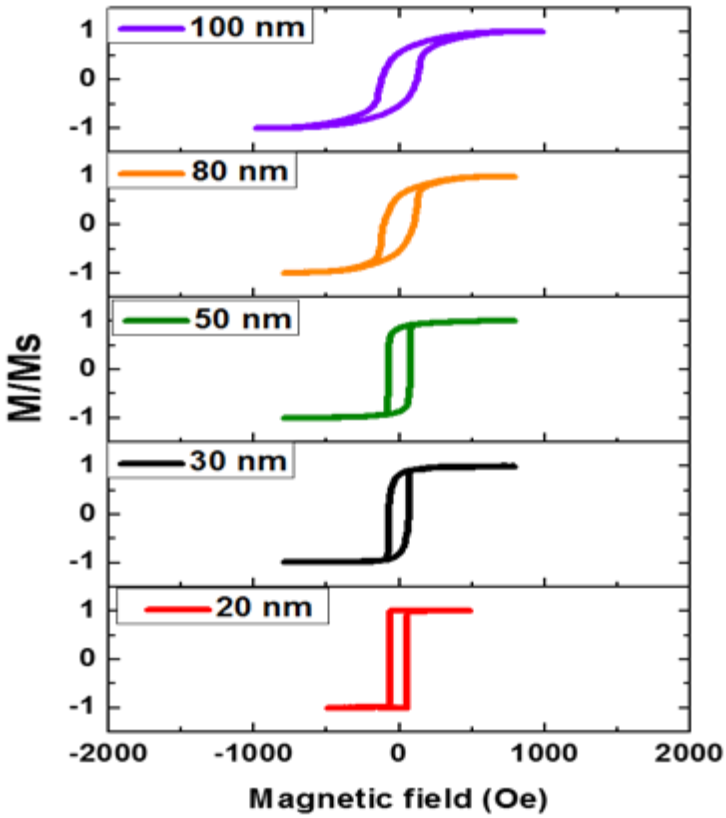


**Figure 4.4:** Longitudinal Kerr hysteresis loops for Fe CTF with different thicknesses (20, 30, 50, 80, and 100 nm).

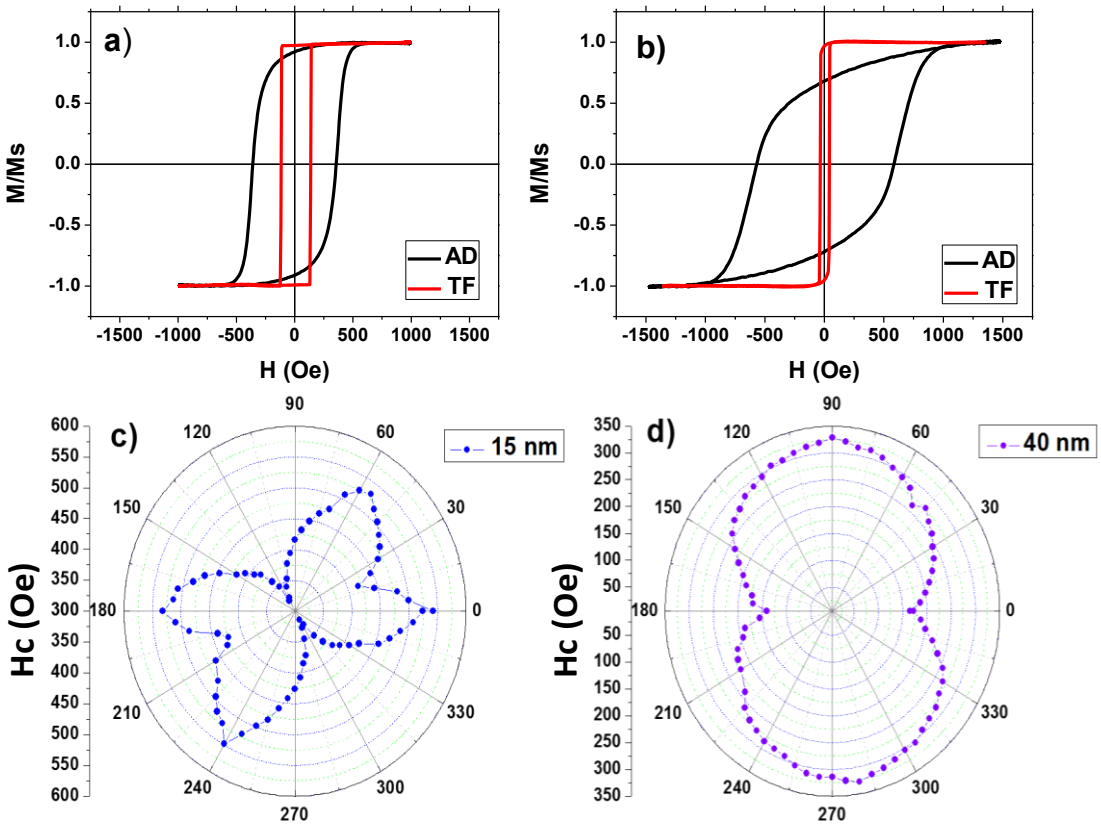


**Figure 4.5**: In-plane hysteresis loops for antidot, AD, arrays and corresponding CTF with film thickness 25 nm a) Fe and b) for Co. c) $H_C(\theta)$, angular dependence of coercivity for Fe AD with layer thickness 15 nm i.e. d > W and d) for Fe AD with layer thickness 40 nm (d < W).

Secondly a sharp increase is observed in the $H_C$ for the INP and OOP directions of the antidot thin film comparing to the CTF. The maximum $H_{C//}$ value of 688 Oe has been obtained for Fe antidot samples with layer thickness 10 nm and 750 Oe for Co antidot arrays with layer thickness 20 nm. This value of coercivity is approximately 11 or 18 times larger than the corresponding one for Fe and Co CTF, respectively. These differences between AD and CTF can be explained because of a change in the mechanism of magnetization reversal and local shape anisotropy induced by the nano-holes arrangement [48,101,102]. It's worth noting that by increasing the layer thickness of AD samples, the in-plane $H_{C//}$ decreases and a magnetic behaviour similar to that of CTF is observed for thicker antidot thin films as show in Fig. 4.6.

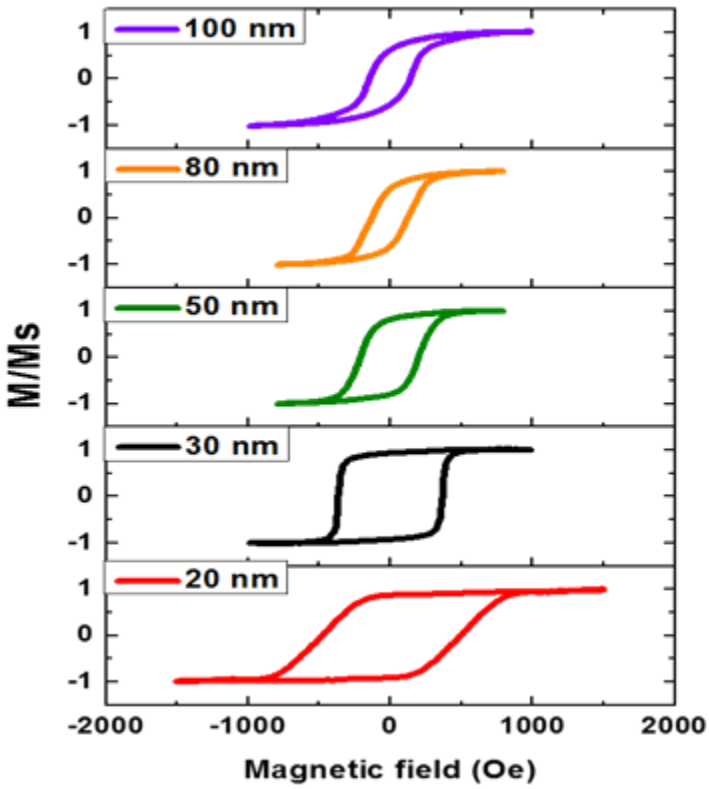


**Figure 4.6:** Longitudinal Kerr hysteresis loops for Fe AD films with different thicknesses (20, 30, 50, 80, and 100 nm).

By direct comparison between Fig. 4.4 and Fig. 4.6, corresponding to samples of CTF and the thin films of antidot arrays, respectively, higher values of $H_{C//}$ are found in the Fe antidots than the corresponding ones for the CTFs with the same layer thickness, which can be associated to an additional pinning effect originated by nanoholes. This pinning effect induced by nanoholes is hindering the domain wall propagation through the film plane, which makes to increase the coercivity of the antidots samples respect to the continuous thin films. Additionally, the magnetostatic dipolar interaction among the holes gives rise to a demagnetizing field in the opposite direction to magnetization [103]. Furthermore, for the antidot samples we found an opposite thickness dependent behavior of $H_{C//}$, as illustrated in Fig. 4.6, where it is clearly shown that coercivity decreases with increasing the Fe antidots thin film thickness. With increasing the layer thickness, the geometry of thin films of antidots arrays changes and the magnetic behavior becomes also

modified. The thickness increasing, adds soft and hard magnetic behaviors due to the decrease of the holes size on the one hand and the increase of the surface roughness of the film by the other side. The shape anisotropy of the thin film is strongly modified by the nanoholes and this enhances the uniaxial anisotropy in the film plane for the thinner samples (larger nanoholes sizes), due to the magnetostatic interactions among the accumulative magnetic poles of opposite sign at each side of the nanoholes that originates a pinning effect, which clearly decays when the nanoholes size diminishes with thickness layer increasing.

The pinning effect ascribed to nanoholes dominates above the roughness surface anisotropy for antidots thin films with smaller layer thickness giving rise to higher coercivity values than in continuous thin films and a decrease of $H_{C\,//}$ when the thickness of the Fe or Co antidots thin films increases. Vazquez et al. [104] propose a phenomenological law which predicts that the coercivity follows a linear relationship with the thickness for the Ni antidots thin films, $H_{C\,//} \alpha (1/t) (D_{int} - d)$, where $D_{in}$ is the inter distance between antidots centers, d is the antidot hole diameter and t the layer thickness. In our case, the parameter $(D_{int} - d)$ remains constant, so $H_{C\,//} \alpha 1/t$. This phenomenological law agrees well also with our experimental data, where it can be seen that $H_{C\,//}$ is inversely proportional to the Fe and Co antidots thin film thickness as plotted in Fig. 4.7b. Actually, this phenomenological law does not totally apply for thinner antidot samples of Fe and Co, meanwhile for thicker samples perfectly apply. So, we supposed a different magnetic behaviour for antidot arrays samples with thinner layer thickness led to decrease the in-plane coercivity. Thus, deeply study for thinner antidot samples will perform in next Chapters of this thesis.

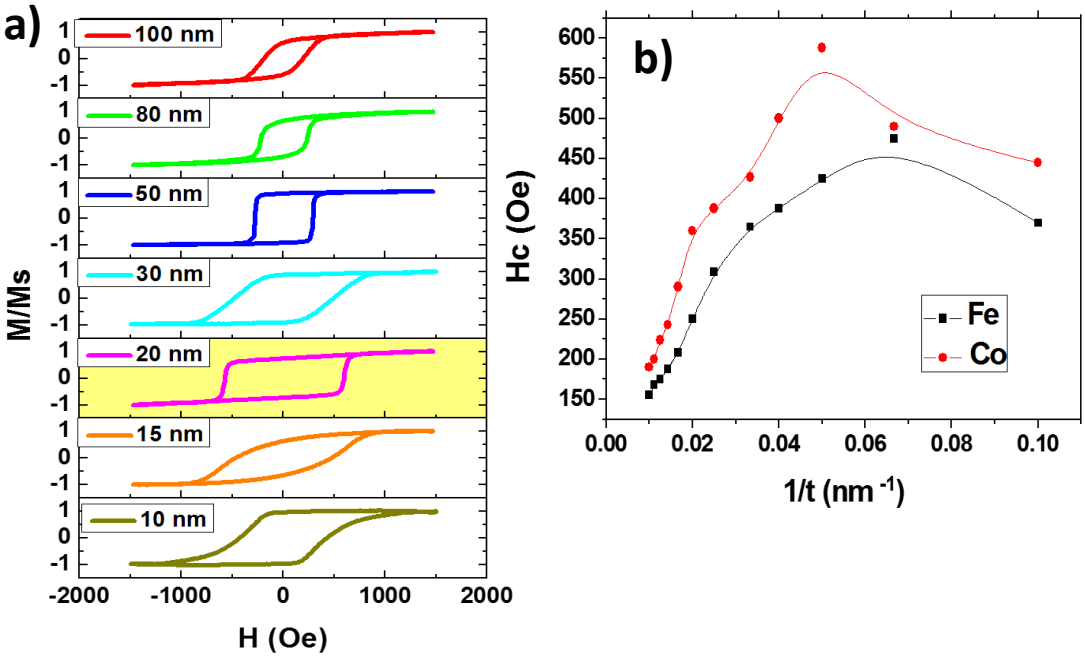


**Figure 4.7:** a) In-plane hysteresis loops for Co antidot arrays with different layer thickness ranging from 10 up to 100 nm and b) The in-plane coercivity behavior versus 1/t for Fe and Co antidot arrays thin films.

## 4.3 **Conclusion**

In conclusion, global and local magnetization behavior in Fe and Co-based antidot thin films is strongly dependent of holes diameter and layer thickness. For thinner AD samples the in-plane $H_{C//}$ show four-fold symmetry meanwhile the thicker AD samples show two-fold symmetry. Unexpected $H_{C//}$ tendency behaviour with 1/t has been observed which predict an interesting magnetic behaviour for AD samples with large hole diameter and thin layer thickness. Tailored design of these novel nanostructured ferromagnetic materials would be of huge interest for applications in many research fields such as high-density magnetic data storage devices, magneto-transport phenomena, logical devices and magnetic sensing.

# Chapter 5: Anomalous In-Plane Coercivity Behaviour in Hexagonal Arrangements of Ferromagnetic Antidot Thin Films

Understanding the nature of magnetism at the nanometer length scale is of interest from a fundamental perspective and for the development of next generation spin-based devices. Two dimensional (2-D) periodic ferromagnetic antidot lattices have emerged as potential candidates for magneto-photonic crystals, [105,106] ultrahigh density magnetic storage media, [42] magnonic crystals and biomedical application [107]. They bear several advantages over the conventional dots system, including the absences of a super-paramagnetic lower limit of the bit size, the preservation of magnetic properties, large-area fabrication at low cost, and the absence of damage caused by nanofabrication [108]. For all these applications, the ability to control the strength and orientation of magnetic anisotropy becomes essential, especially for the thermal stability and switching reliability of magnetic bits. Nevertheless, the astonishing development of nanofabrication techniques in the last decades has opened the door to a new strategy for the patterning of nanostructures, which allows for the modification of the local magnetization distribution in a controlled way [62,71,109–111]. The relevant length scale parameter for magnetic phenomena in thin films is the characteristic correlation length, $R_{Coh}= \sqrt{24A/\mu_0 M_s^2} = \sqrt{24}\, l_{exch}$ (where $A_{exch.}$ is the exchange constant or stiffness, $M_s$ the saturation magnetization, and $l_{exch}$ is the exchange length). This parameter refers to the maximum size of the ferromagnetic material for which its magnetization reversal takes place by quasi-uniform magnetization rotation process rather than domain wall movement [67][112]. Also, the antidot geometry can tailor the coercivity, $H_C$, and in many previous studies [82,102,104,113] they report on the empirical law according to which $H_C$

increases linearly with the inverse of the antidot edge-to-edge separation $W = D_{int} - d$, where d is the antidot hole diameter and $D_{int}$ the antidot array lattice constant.

In this Chapter, we demonstrate that by properly controlling the geometrical parameters of former alumina templates it can noticeable modify the magnetic properties of ferromagnetic (FM)-antidot arrays thin films. Anomalous in-plane coercivity dependence behaviour with W has been detected for Fe, Co and Ni-antidot arrays samples. Critical in-plane edge-to-edge distances, $W_{c//}$, of 18, 24 and 33 nm have been found for Fe, Co and Ni-antidots, respectively, where the in-plane coercivity starts decrease with decrease the W and the out of plane coercivity increase rapidly with decrease the W. In addition, another critical edge-to-edge distances, $W_{c\perp}$, around of 14 nm and 22 nm have been found for Co and Ni antidot, respectively, where the crossover of the magnetization from the in-plane to out-of-plane occurs.

## 5.1 Morphological characterization of antidot arrays thin films

After the thermal layer evaporation process, all samples were analysed using scanning electron microscopy (SEM, JSM 5600, JEOL, Akishima, Tokyo, Japan) to measure the nanohole diameter, d, and the inter-holes distance, $D_{int}$. Figure 5.1(a, b, and c) shows the top view images of selected Co antidot samples with small d i.e. large W around 73 nm, (Fig. 5.1a), and small W around 28 nm and 14 nm, (Fig. 5.1b), and (Fig. 5.1c). We observed for all samples a well-ordered hexagonal arrangement of holes with a constant periodicity of 103±2 nm, in good agreement with what is commonly obtained in the patterned alumina substrate after the two-step anodizing procedure in oxalic acid at 40 V. The samples with etching time = 53 min [114] shows the maximum pore diameter of 93±1 nm, i.e. minimum W ≈ 11 nm, and corresponding hole size around of 89 nm, i.e. W ≈ 13 nm, which can also be achieved for the Fe, Co and Ni-antidot thin film samples,

respectively, (Fig. 5.1c). Figure 5.1d summarizes the evolution of the edge-to-edge distance as a function of the hole diameter of Co antidot arrays film. Here, W takes values in the range from 73 nm up to 13 nm. A linear relationship is found between W and *d* as show in (Fig. 5.1d). It is worth to mention that the values of the hole diameter here reached are higher than the ones previously obtained with similar techniques [84,86,115–117].

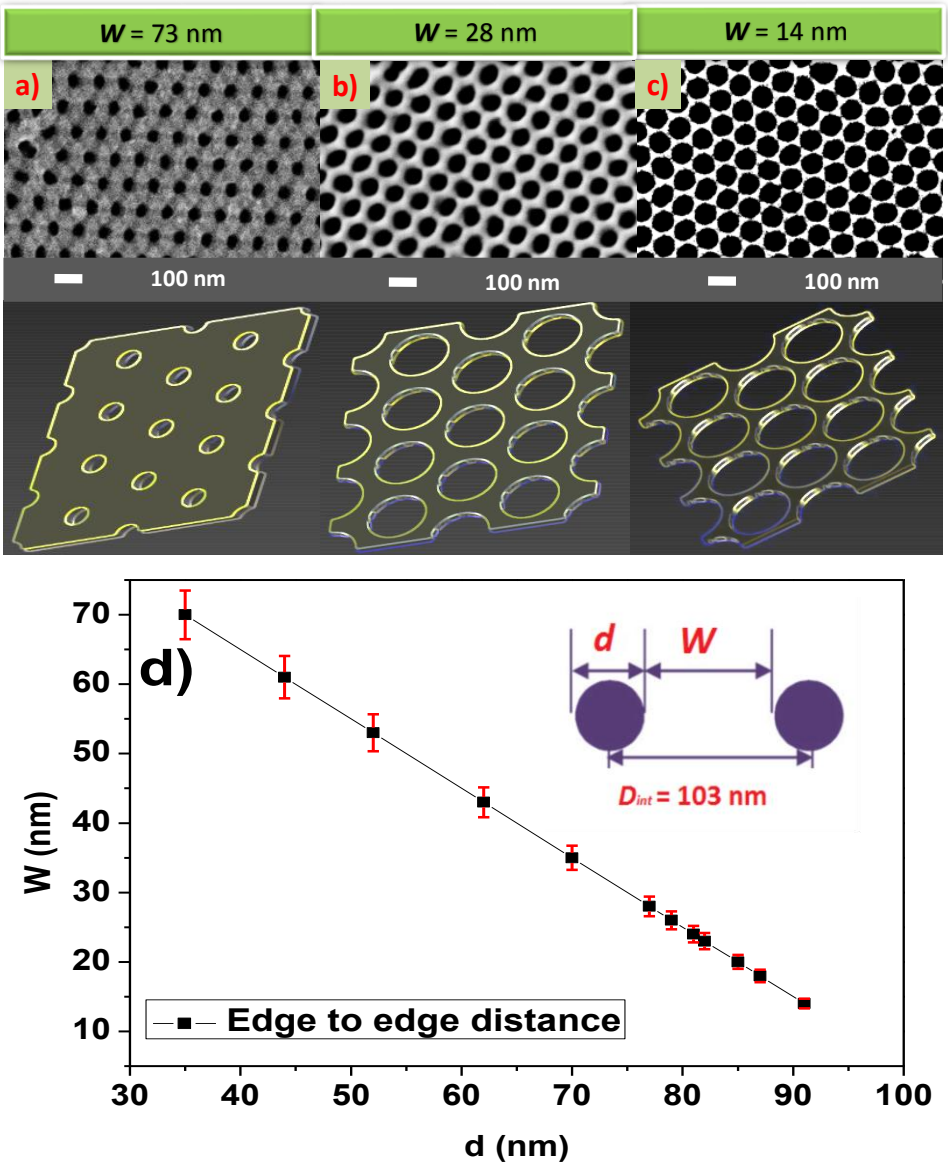


**Figure 5.1:** SEM images of Co layer deposited on the top of nanoporous alumina membranes with varying the edge to edge distance, W, (a) 73 nm, (b) 28 nm and (c) 14 nm. d) The edge to edge distance, W, versus hole diameter, d, of Co thin layer deposited on the alumina templates.

The surface magneto-optic properties of the Fe, Co and Ni-antidot array thin films were measured making use of a scanning laser Magneto-Optical Kerr Effect (MOKE) magnetometer as described in Chapter 3 (section 3.3.3).

## 5.2 Magnetic characterization of antidot arrays thin films

The surface magneto-optic properties of the Fe, Co and Ni antidot thin films were characterized along the In-plane, INP, and Out-of-plane, OOP, directions making use of the MOKE technique [38,114]. For the INP direction, we have been selected the INP easy magnetization axis, which corresponds to the hysteresis loop with highest INP coercivity, $H_{C//}$, and INP remanence.

Figure 5.2 represents selected INP and OOP hysteresis loops of Fe, Co and Ni antidot arrays thin films with W ranging between 73 and 14 nm, and the unpatterned Fe, Co and Ni continuous thin film, CTF, of the same layer thickness 20 nm which employed as a reference sample. Several differences INP magnetic properties of Fe, Co and Ni antidots have been found comparing to their corresponding CTF. Firstly; the in-plane hysteresis loops lose its squareness and become wider. This fact is consistent with the scenario where the antidots are acting as pinning centres for the displacement of magnetic domain walls and leads to increase the in-plane coercivity i.e. wider hysteresis loops [114,118]. Also, the INP loops with W= 18, 22 and 28 nm for Fe, Co and Ni antidot films show multi-step magnetization behaviour which indicates a strong pinning effect and complex magnetization reversal process as shown in Fig.5.2 (c, g and k). The possible reason of multistep magnetic behaviour is attributed to the fact that the material inside the walls of the pores can have a different magnetization orientation, OOP in this case, contributing to the harder magnetic step, while the material in between the pores shows INP magnetization, corresponding to the softer magnetic step [41,119,120]. Meanwhile,

the hysteresis loops of the small hole diameter i.e. large W samples exhibit a single magnetic behaviour as shown in Fig. 5.2(b, f and j). For FM-antidot samples with W ≤ 18 nm, a sharp drop of the $H_{C//}$ and increasing in the OOP coercivity, $H_{C\perp}$, have been observed as plotted in Fig. 5.2(d, h and i).

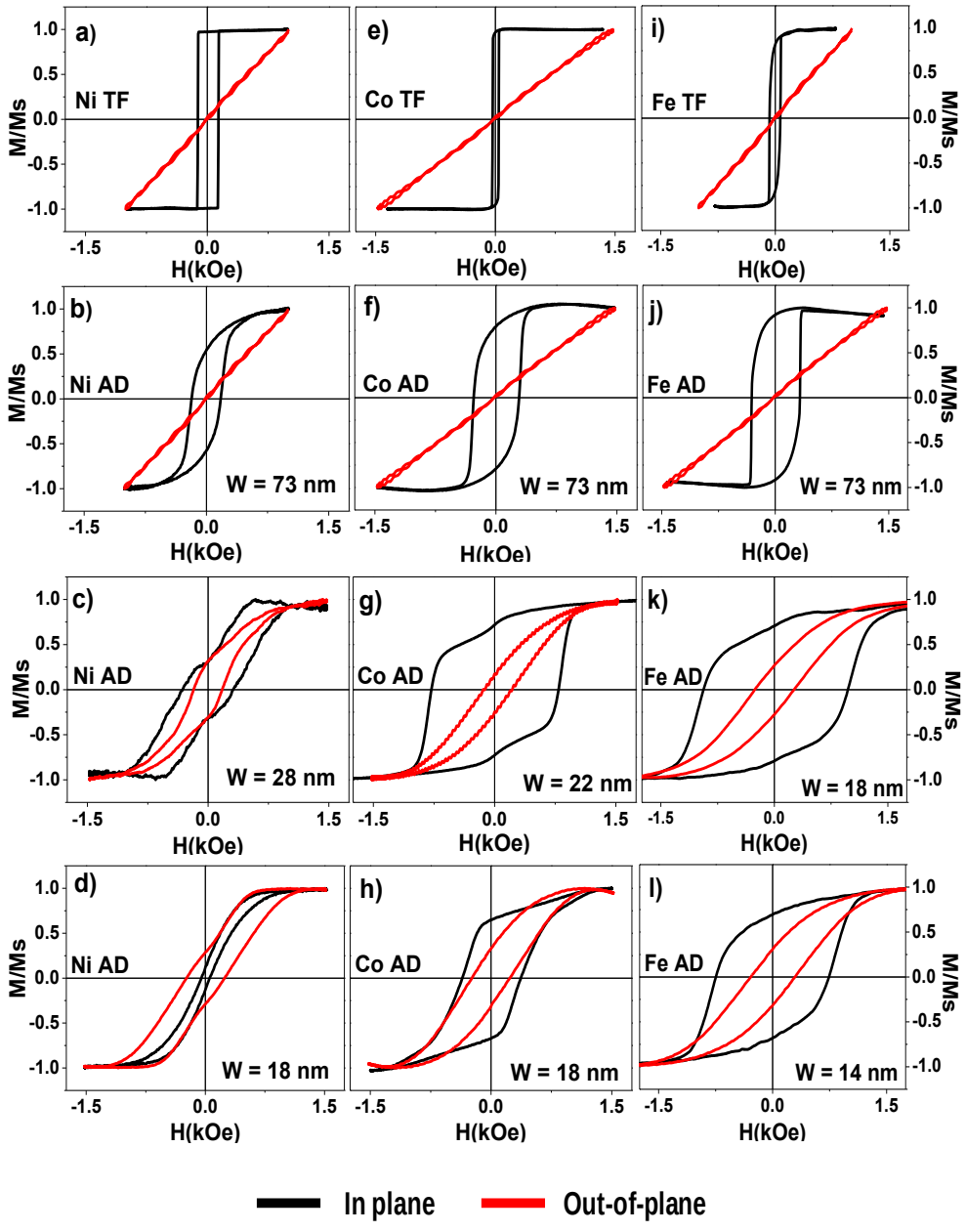


**Figure 5.2:** In-plane (black) and out-of-plane (red) hysteresis loops for antidot, AD, arrays with layer thickness 20 nm a) Ni TF, b), c) and d) for Ni AD arrays samples, e) Co TF, f), g) and h) for Co AD arrays thin film and i) Fe TF, j), k) and l) for Fe AD arrays films. The edge to edge distance for each sample was specified in the lower right corner of the graphs.

Figure 5.3 summaries the evolution of $H_{C//}$ and $H_{C\perp}$ of Fe, Co and Ni antidot arrays thin films with respect to W evolution. The maximum value of $H_{C//}$ about 570 Oe was obtained for the Ni antidot sample with W = 33 nm, which is approximately 8.5 times larger than the unpatterned film coercivity. Then, an unexpected $H_{C//}$ decreasing with W appears as indicated in Fig. 5.3a. The same tendency for $H_{C//}$ has been observed in Fe and Co-antidot arrays with decreasing the edge-to-edge distance, as plotted in Fig. 5.3a. Maximum $H_{C//}$ values of 1040 Oe with W = 18 nm and 765 Oe with W = 24 nm have been found for the Fe and Co-antidot samples, respectively. These $H_{C//}$ values are approximately between 15 and 17 times larger than the ones for unpatterned thin film, as shown in Fig. 5.3(a). Therefore, an in-plane critical edge to edge distance, $W_{c//}$, has been detected for Fe, Co and Ni-antidot samples, where $H_{C//}$ starts to decrease with W decreasing while the out of plane coercivity, $H_{C\perp}$, increase rapidly with W decreasing. Thus, it can be found that the $H_{C//} \alpha 1/W$ for antidot samples above the $W_{c//}$ and the $H_{C//} \alpha W$ for antidot samples below the $W_{c//}$.

A sharp increase in $H_{C\perp}$ for antidot samples with $W < W_{c//}$ has been observed as plotted in Figure 5.3. In fact, antidot arrays thin films deposited on the top-surface of nanoporous alumina templates reproduce the intrinsic surface roughness of the patterned templates and develop a crescent shape during the thin film deposition process [97,119–122]. These two morphological features can determine the magnetic anisotropy of the material. Thus, the magnetic moments between nanoholes remain aligned parallel within the film plane, while magnetic moments along the walls of the nanoholes are perpendicularly aligned to the film plane [114]. The effect on the magnetization component along the perpendicular direction to the sample surface becomes higher and stronger as the W decreases [41,80]. In addition, as W is further decreased, the interdistance between adjacent holes becomes narrower, and the film area that has to be

nucleated is very small, therefore the magnetization reversal is more favourable via the coherent rotation rather than domain wall movement, which may lead to decrease the $H_{C//}$ [118].

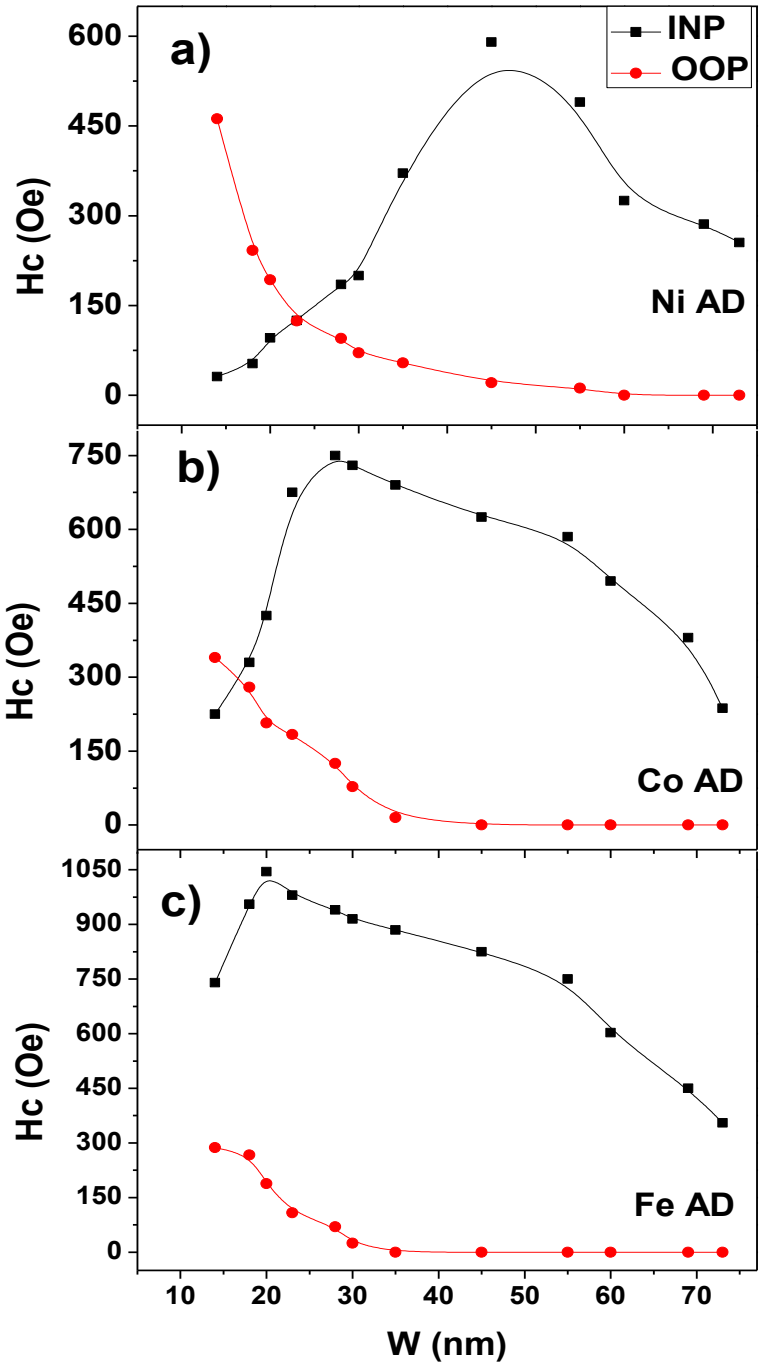


**Figure 5.3:** INP coercivity and OOP coercivity dependence of a) Ni AD, b) Co AD and c) Fe AD thin films with 20 nm layer thickness and different edge-to-edge separation.

Simultaneously, the $H_{C\perp}$ is increasing rapidly until it reaches the value of $H_{C//}$ at W = 22 nm for Ni antidot and W ≈ 17 nm for Co antidot, as show in figure 5.3a and figure 5.3b. Therefore, the well-known phenomenological law ($H_{C//} \propto \frac{1}{D_{int}-d} \propto \frac{1}{W}$) [80,100,102,104,123–127] is found to be not valid for all cases; but it has a limitation corresponding to the current results, where ($H_{C//} \propto \frac{1}{W}$ for $W \geq W_{c//}$ and $H_{C//} \propto W$ for $W < W_{c//}$.

It is worth noting the relationship between the W of the Fe, Co and Ni antidot array thin films and the coherence radius ($R_{Coh} = \sqrt{24A/\mu_0 M_s^2} = \sqrt{24}\, l_{exch}$) [67] for Fe, Co and Ni, since the later refers to the maximum size of a uniformly magnetized particle, where magnetization reversal takes place by coherent rotation rather than domain wall movement [67,68]. Therefore, the reported values of the coherence radius for the magnetic materials within the scope of present study are listed in table 5.1.

**Table 5.1**: Room temperature magnetic parameters and coherence radius for ferromagnetic materials and comparing with critical edge to edge distance, $W_c$.

| Materials | $l_{exch}$ (nm) | $R_{Coh}$ (nm) | $W_{c//}$ (nm) | $W_{c\perp}$ (nm) |
|---|---|---|---|---|
| **Fe** | 2.4[67] | 12[67] | 18 | - |
| **Co** | 3.4[67] | 17[67] | 24 | 14 |
| **Ni** | 5.1[67] | 25[67] | 33 | 22 |

From comparison between W and $R_{Coh}$ values, it can be found that the $W_{c//} > R_{Coh}$ for Fe, Co, and Ni antidot arrays samples. When $R_{Coh}$ is similar to the value of W, the $H_{C\perp}$ is increasing rapidly until $H_{C\perp} \geq H_{C//}$ for antidot samples with $W \leq R_{Coh}$, as plotted in Figure 5.3. Those indicate that for antidot arrays thin film with W close to the $R_{Coh}$ value, where the magnetization reversal mechanism changes from magnetic domain wall movement (for AD with large W) to magnetization rotation of single domain (for AD with short W) [68,114,118,128]. Thus, the crossover of the easy magnetization axis from the INP to OOP direction has been detected at critical edge-to-edge distance, $W_{c\perp}$, for Ni and Co antidot with $W_{c\perp}$ = 22 nm and 14 nm, respectively. Unfortunately, we could not be able to reach the $W_{c\perp}$ for Fe antidot thin films due the lowest value of W for antidot samples that could be obtained in current work was 14 nm, which is higher than the $R_{Coh}$ of Fe.

## 5.3 Conclusion

In summary, the magnetic properties of FM-antidot arrays are strongly dependent on the geometrical parameters of the former nanoporous alumina template. The current results suggest a unified description of the magnetic behaviour of FM-antidot arrays thin films along the change of $H_{C//}$ behaviour with W that takes place at the critical edge-edge distance ($W_{c//}$ = 18 nm, 24 nm and 33 nm) for Fe, Co and Ni-antidot arrays samples, respectively. At the critical edge-edge distance, the maximum $H_{C//}$ have been obtained due to two different complex domain wall pinning mechanism, between the neighbouring holes and inner wall of the holes. The multistep magnetic behaviour observed for antidot samples with $W < W_{c//}$ reveals the strong contribution of the OOP component in the magnetization reversal mechanism of the FM-antidots thin films. The magnetization crossover from the INP to OOP directions has been detected for antidot samples with $W_{c\perp}$

$< R_{Coh}$ at 22 nm and 14 nm for Ni and Co antidot arrays samples, respectively. The dual behaviour of the INP/OOP coercivity points towards a new nanotechnological strategy of fabrication arrays of magnetic bits, i.e., basic elements for magneto-optic perpendicular recording patterned media, embedded into a continuous 2D structural system.

# Chapter 6: Tuning Nanohole Sizes in Ni Hexagonal Antidot Arrays: Large Perpendicular Magnetic Anisotropy for Spintronic Applications

Ferromagnetic thin films with perpendicular magnetic anisotropy (PMA) become a key driving force in the development of magnetic random-access memory (MRAM) devices, spintronic devices and logic chips with high thermal stability [129–131]. The traditional approach for PMA engineering is to use Ferromagnetic (FM)/oxide interfaces [132,133] or multilayer structures comprising two FM or FM/nonmagnetic metal interfaces [134–136], and amorphous rare earth-transition metal alloys [137,138]. However, there is still a challenge to enable the large magnetic anisotropy, especially PMA, in commonly used 3d transition metals such as Fe, Co and Ni (and their alloys) thin films. Here, we propose a Ni thin film with hexagonally antidots arrangement having large PMA that might be of huge importance for nanostructured antidot arrays based spintronics application. The choice of antidot arrays system is governed by its ability for tuning the physical properties of various host-patterned materials by varying the holes parameters in the nanoscale, as they are the nanohole size and their neighboring inter-distance [139,140]. Therefore, if large PMA can be realized, Ni antidot array architectures can be very promising for bit patterned media and spin transfer torque magnetic random-access memories (STT-MRAM) application [130,141]. Moreover, the proposed antidot−Ni thin film system is unique in view of the long-standing challenge to promote PMA in spintronic devices, comprising materials with a weak spin-orbit coupling (SOC) [142]. This is extremely important since the presence of heavy-ions elements in the system increases damping constant and strongly reduces spin diffusion lengths, thus limiting magneto-resistance and precluding low critical currents for magnetization reversal, two initial key factors for STT-MRAM applications [141,142].

In this work, we demonstrate that controlling the geometrical parameters of alumina templates of Ni-antidot arrays thin films can greatly enhance the PMA that is not displayed by continuous Ni thin film, taken as the reference sample. A critical hole diameter, $d_c$, around of 80 nm has been found, where the crossover of the magnetization from in-plane to out-of-plane occurs. The highest value of the effective perpendicular magnetic anisotropy energy density observed for the Ni antidot thin film with d = 90 nm and t = 20 nm is around 1.44 erg/cm$^2$, which it is larger than that obtained by traditional approaches for Ni thin films with PMA (0.03-0.2erg/cm$^2$). These findings point toward the tailoring of large perpendicular magnetic anisotropy for the Ni antidot arrays, which stands as a hallmark for future bit patterned magneto-optic perpendicular recording media and advanced spintronic applications based on template-assisted deposition techniques.

## 6.1 Fabrication of Ni antidot arrays thin films

The controlled deposition of the metallic film formed by highly pure metal pieces of Ni (Goodfellow Limited, England, 99.99% purity) was performed by high vacuum thermal evaporation technique (see Fig. 6.1b) using an E306A thermal vacuum coating unit (Edwards, Crawley, UK) with an ultimate vacuum better than $4.1 \times 10^{-7}$ mbar [38]. The pure Ni metal pieces were put inside a water-cooled copper crucible and have been heated by magnetically focused electron beam, 3.1 kV and electric energy 2.7 kW. The evaporated Ni metal was deposited on the top-surface of the NPAAMs, which served as templates to obtain the thin film antidot arrays (Fig. 6.1c) [83]. The layers film thickness was checked by using a quartz crystal controller that monitored the deposition rate of the evaporation source. The distance between the evaporation source to substrate sample holder was fixed at about 18 cm. The deposition rate of Ni metal was around (0.10–0.15) nm/sec, and it was performed with a deposition angle of about 15º measured between the metal target and the normal direction to the sample surface.

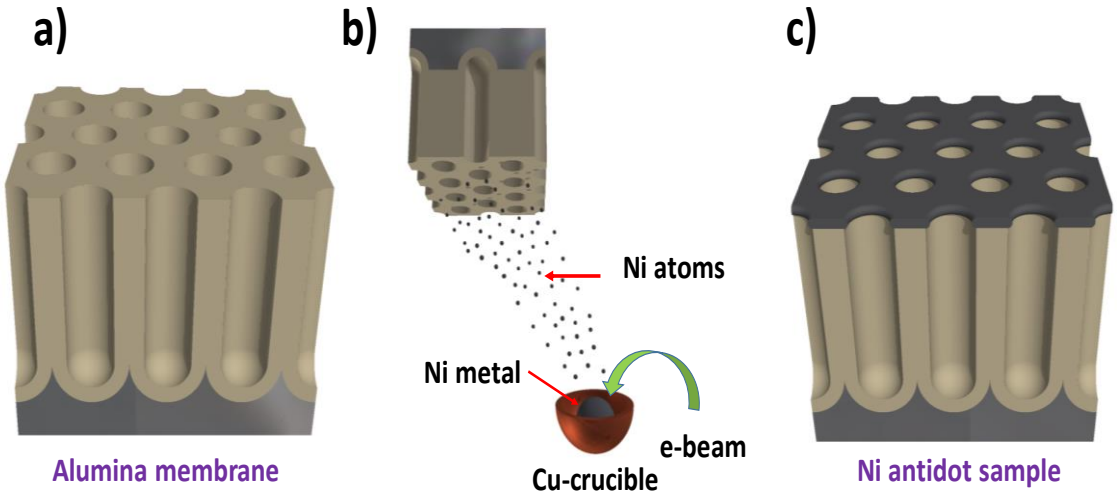


**Figure 6.1**: Schematic drawings of a) hexagonally self-ordered nanoporous anodic alumina membrane, NPAAM, as starting substrate, b) Ni vacuum thermal evaporation process on top surface of the NPAAM template and c) Ni antidot thin film sample by replicating the nanoholes structure of the NPAAM template.

## 6.2 Morphological characterization of antidot arrays samples

After the thermal layer evaporation process, all samples were analyzed using scanning electron microscopy (SEM, JSM 5600, JEOL, Akishima, Tokyo, Japan) to measure the nanohole diameter, d, and the inter-holes distance, $D_{int}$. Fig. 6.1 shows the top view images of nine selected antidot samples having different d values. We observed for all samples a well-ordered hexagonal arrangement of holes with a constant periodicity of 103±2 nm in good agreement with what is commonly obtained in the patterned alumina substrate after the two-step anodizing procedure in oxalic acid at 40 V.

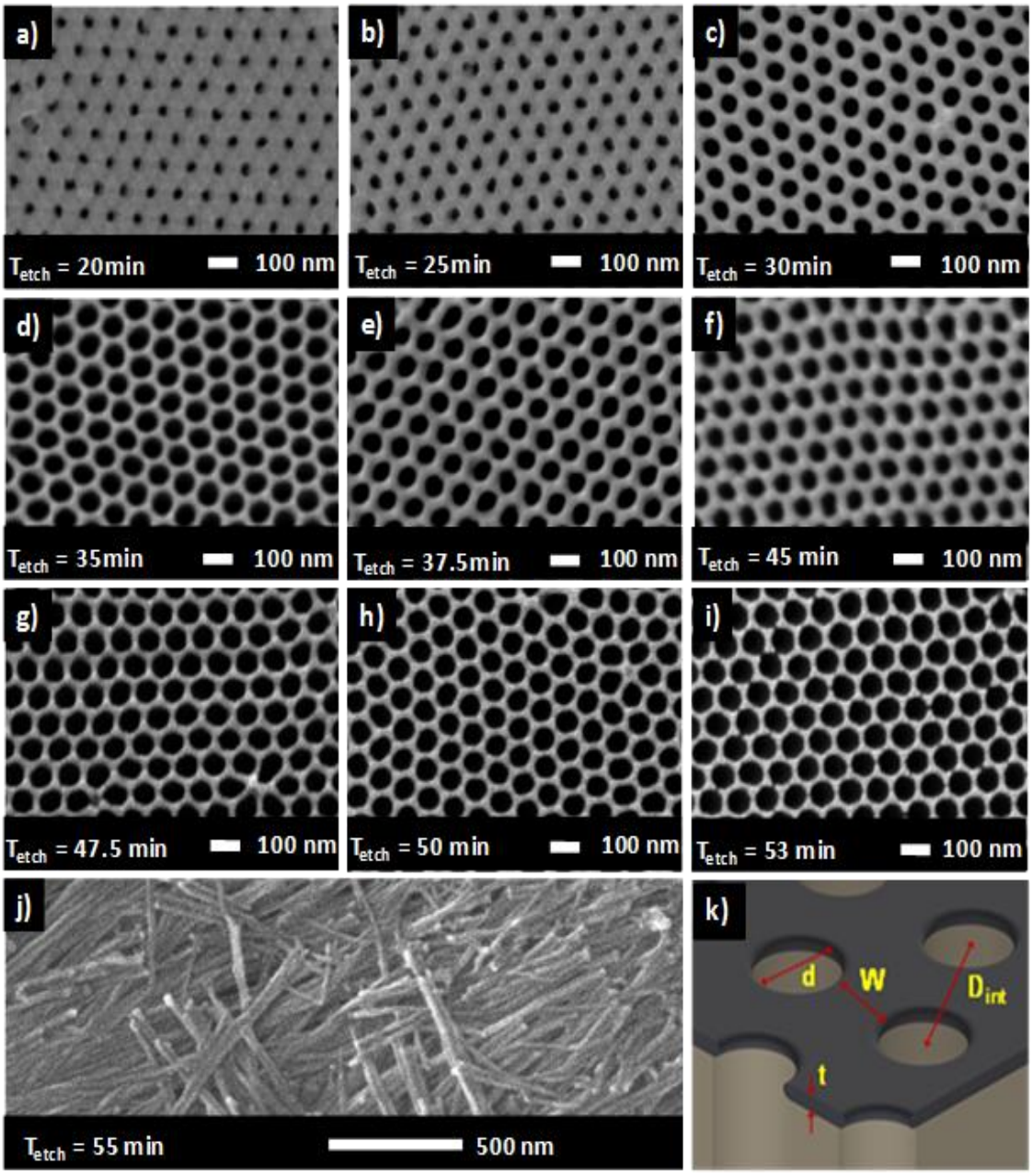


**Figure 6.2:** a) to i) SEM images of Ni layer deposited on the top-surface of the NPAAM after being submitted to pore widening process under different chemical etching time, $T_{etch}$. j) SEM image of the alumina membrane showing the collapse of the hexagonal pores symmetry for $T_{etch}$. = 55 min. k) 3d sketch of Ni antidot arrays on top surface of the NPAAM, indicating the main morphological lattice parameters of the sample, namely: d = hole diameter, $D_{int}$ = interhole distance, t = thickness, and W = $D_{int}$-d.

The sample with $T_{etch}$ = 53min. shows the maximum pore diameter of 93 nm and corresponding hole size around of 89 nm that can be achieved for both, the alumina template and antidot thin film samples, respectively (Fig. 6.1i). Also, for higher $T_{etch}$ = 55

min. the hexagonal pores ordering of the alumina membrane is found to become totally destroyed, as shown in Fig. 6.1j.

Figure 6.3 summarizes the evolution of the hole diameter, d, and the edge-to-edge distance, W, where ($W = D_{int} - d$), as a function of the etching time for the pores widening. Here, d takes values in the range from 35 ± 3 nm up to 89 ± 1 nm, which is plotted as a function of $T_{etch}$. Therefore, W decreases from 67 nm down to 14 nm, while $D_{int}$ keeps constant at 103 nm, respectively. A linear relationship is found between d and $T_{etch}$ with an inflection point for $T_{etch}$ = 37.5 min, at which the rate of the hole size increases with etching time changes. Pore wall oxide in the early stage is etched at a higher rate ($T_{etch}$ < 37.5 min., with slope = 1.12 nm/min.), than that in the later stage ($T_{etch}$ > 37.5 min., with slope = 0.84 nm/min.). The retarded rate of chemical etching in the later stage can be attributed to the relatively purer Al oxide nature of the inner pore wall, as compared to the less dense Al oxide of the outer pore wall due to the incorporation of anionic species [82,143]. The linearity of pore diameter increasing with pore widening time has been already previously described for many studies [38,77,82,83]. As the center-to-center distance between two adjacent pores (and therefore holes also) remains constant at about 103 nm, the edge-to-edge distance, W, decreases consequently with d increasing, as shown in Fig. 6.3b.

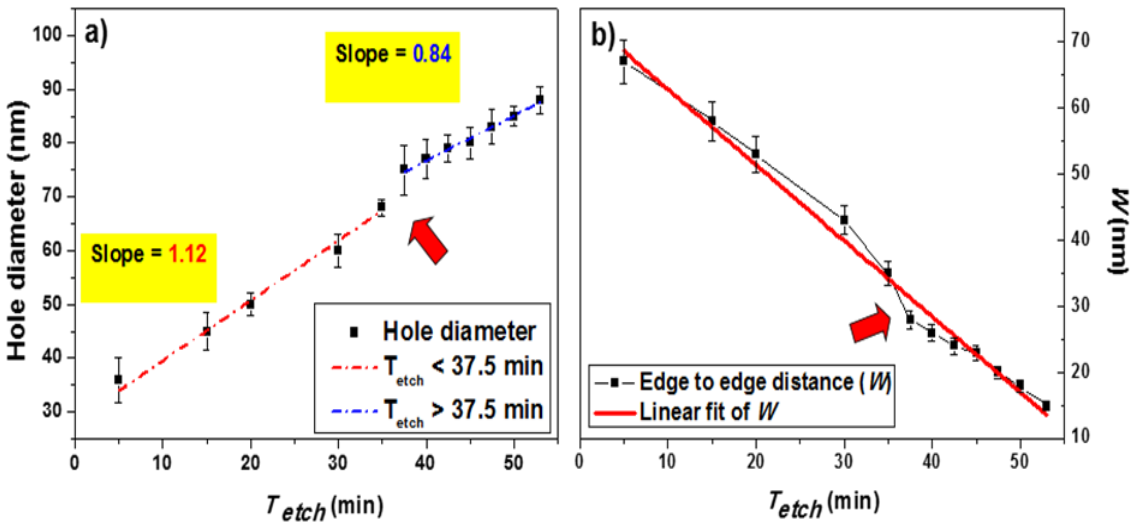


**Figure 6.3**: a) Nanoholes size, d; and b) the edge-to-edge distance, W, versus etching time $T_{etch}$ for the Ni thin layer deposited on NPAAM templates. The red arrows indicate the inflection point at $T_{etch}$ = 37.5 min.

In our study, a limit value of the nanohole diameter seems to be reached at the high $T_{etch}$ regime equal to 53 minutes, evidenced by the destruction of the hexagonal ordering of the nanoporous structure, as shown in Figure 6.2 j. Indeed, the main reason that may lead to a limit value of the nanohole diameter is the available area between two adjacent holes, which is $D_{int}$-d, where $D_{int}$ is near to 103 nm. By increasing d and keeping constant $D_{int}$, this distance is reduced down to its minimum value. Consequently, d reaches a maximum value for a network with a fixed $D_{int}$ parameter, around d = $D_{int}$ ≈ 103 nm. Here, the maximum d value reaches ≈ 93 nm, indicating that the stabilization of the hexagonal network is stabilized up to 90.3% of the maximum value for pores of the alumina membrane and 88 % for Ni antidot thin film with thickness around of 20 nm. This value here reached is higher than the ones previously obtained with similar techniques [84–86,144].

## 6.3 Magnetic characterization of antidot arrays samples

The surface magneto-optic properties of the Ni continuous thin film and antidot array thin films have been obtained making use of a scanning laser Magneto-Optical Kerr Effect (MOKE) magnetometer. Complementary bulk magnetic measurements of Ni antidot arrays thin films were carried out by using a vibrating sample magnetometer (VSM-QD-Versalab, San Diego, CA, USA), with applied magnetic fields up to ±3 T, measured at room temperature (RT) and in both, parallel (In-Plane, INP) and perpendicular (Out-of-Plane, OOP), directions to the film plane, respectively. The micromagnetic simulations of Ni antidot arrays with different hole diameter have been performed using the Mumax$^3$ package software. It allows the calculation of the temporal evolution of the reduced magnetization, $\overrightarrow{m}$, based on the modified Landau-Lifshitz-Gilbert-Slonczewski equation of motion for the magnetization, $\overrightarrow{m}((\vec{r}), t)$. A finite difference discretization permits the magnetostatic field to be estimated as a discrete convolution of the magnetization [96].

For survey, the induced PMA by nanoholes of the antidot arrays thin films, we have selected a set of samples having a wide range of hole diameters as summarized in Figure 6.3a and fixed lattice parameters for $D_{int}$ and layer thickness, t, of the thin film with averaged values of 103±2 nm and 20 nm, respectively. Also, we divide the antidot samples into two groups according to their W/t ratios, the first group with W > t and the latter group having W ≤ t.

The surface magneto-optic properties of the Ni antidot thin films were characterized along the INP and OOP directions making use of the MOKE technique. For the INP direction, we selected the INP easy axis, which corresponds to the hysteresis loop with highest $H_{C\,//}$ and $m_{r//}$. In Figures 6.4(a, b) there are represented both, the transversal and

polar MOKE hysteresis loops of the Ni antidot thin films for the first group of samples with W > t. The results are plotted in Figure 6.4 for the antidots with nanohole diameters ranging between 35 ± 3 and 75±2 nm, besides for the unpattern Ni film of same thickness employ as a reference sample. As plotted in Figure 6.4a, the magnetization is initiate to be INP oriented for all samples, as indicated by the large $m_{r//}$ magnetization and large values of the coercivity. In contract, we detected remnant magnetization near to zero and high saturating field measured along the OOP orientation (Fig. 6.4b). It can also be seen in the Figure 6.4, that the increase in the antidot hole diameter, d, which indicates an increase in the antidot arrays density, leads to an in-plane hysteresis loop with larger coercivity, $H_{C//}$. This fact is consistent with the scenario where the antidots are acting as pinning centers for the displacement of magnetic domain walls [118].

The maximum of $H_{C//}$ value of around 590 Oe was obtained for the Ni antidot sample with d = 70 nm, which is approximately 8.5 times larger than the coercivity value of continuous thin film. Also, the enhancement of the out of plane coercivity, $H_{C\perp}$, has been noticed as a consequence of the increase of the hole diameter from zero for the reference sample (continuous thin film) up to $H_{C\perp}$ =77 Oe for the antidot sample with d = 70 nm. This fact indicates that for antidots thin films with large nanoholes diameter, the magnetization does not totally lie in the INP direction, but some magnetization component appeared along the out of the sample plane induced by the holes nanostructuring can be also observed [116].

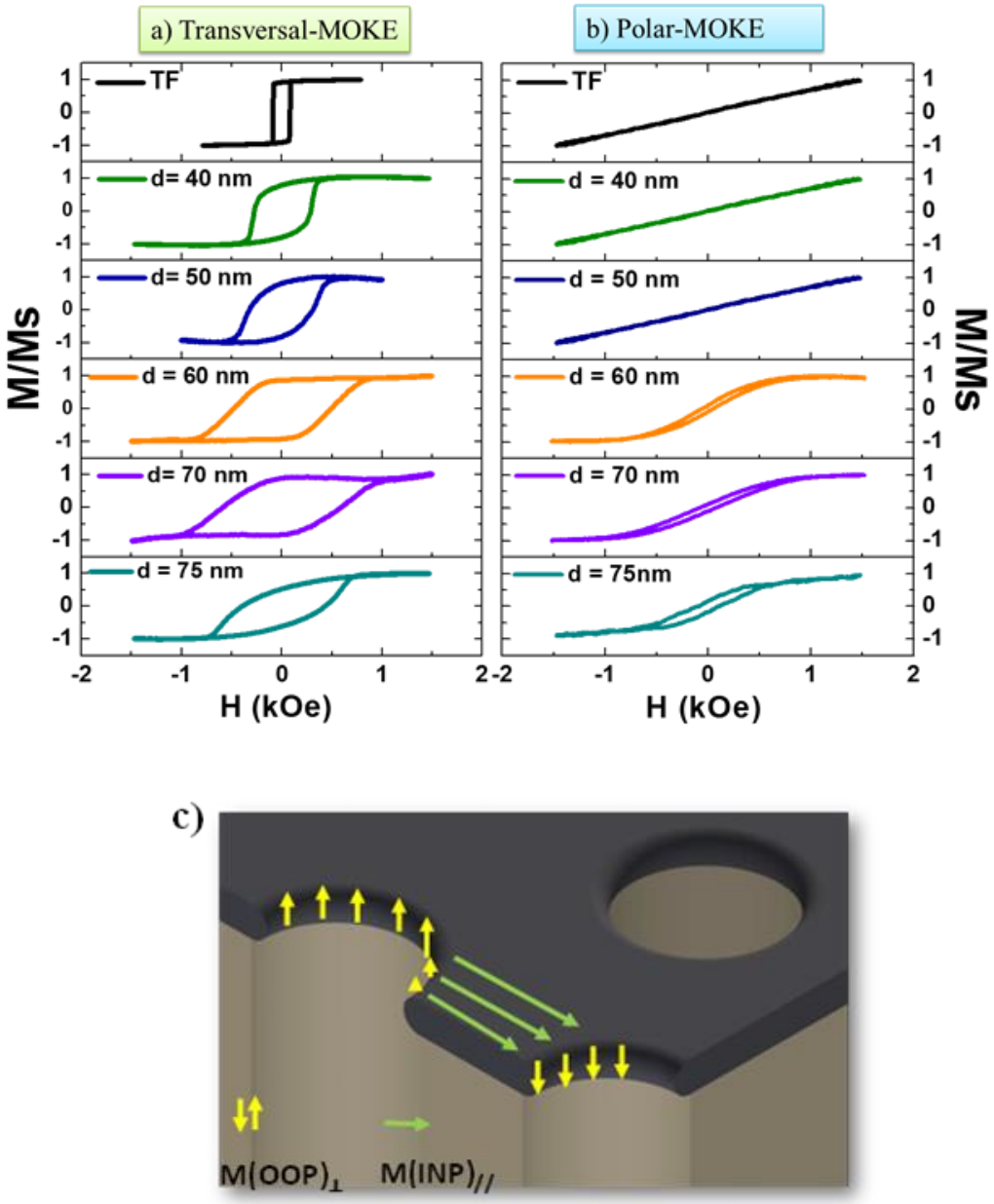


**Figure 6.4:** a) Transversal and b) Polar MOKE hysteresis loops for the 20 nm thick continuous Ni thin film (black loop) and Ni antidot arrays samples with different hole diameter ranging from 40 nm up to 75 nm and 103 nm of interpore distance. c) Three-dimensional sketch of the Ni antidot arrays. The arrows indicate the magnetization directions along the magnetic thin films at remanence state for antidot samples with d < 80 nm and $D_{int}$ = 105 nm.

For antidot sample with d = 75 nm, a sharp drop of the INP coercivity, $H_{C//}$, and reduced remanence, $m_{r//}$, has been observed, as $H_{C//}$ and $m_{r//}$ decreased from 590 to 351Oe and 0.75 to 0.35, respectively. Meanwhile, the OOP coercivity, $H_{C\perp}$, and remanence, $m_{r\perp}$,

increase from 77 Oe to 107 Oe and 0.08 to 0.21, respectively. It seems that increased OOP magnetization distribution obtained for this sample with 75 nm of hole diameter is related to the underlying surface morphology of the patterned substrate of the NPAAM. In fact, AD thin films deposited on top-surface of NPAAM templates reproduce the intrinsic surface roughness of the patterned templates, [117,121,122] but they also develop crescent shape during the thin film deposition process, as sketched in Fig. 6.4c [41,120,145,146]. These two morphological features can determine the magnetic anisotropy of the material. Thus, the magnetic moments between nanoholes remain parallel aligned within the film plane, while magnetic moments along the walls of the nanoholes are perpendicularly aligned to the film plane, as schematically shown in Fig. 6.4c. The effect on the magnetization component along the perpendicular direction to the sample surface becomes higher as the nanoholes diameter increases, i.e. W decreases [41,85,86,147].

Figure 6.5 shows the INP and OOP hysteresis loops for the second group of Ni antidot samples where $W \leq t$ with hole diameter ranging from 80 to 89±1 nm. Surprisingly, a crossover of the easy magnetization axis from the INP to OOP direction has been detected as shown in Figure 6.5 (c, d). This crossover started with a balance between the INP and OOP coercivity for the sample with nanohole diameter around of 80 nm ($H_C \approx 127$ Oe) for both applied field directions (Figure 6.5a). Then, a balance between the INP and OOP $m_r$ for samples with nanoholes diameter of 83 nm can be observed, together with a dominated OOP coercivity, as shown in Figure 6.5b. Finally, a dominant magnetization component along the perpendicular to the plane of the sample surface has been observed as plotted in Figure 6.5(c, d).

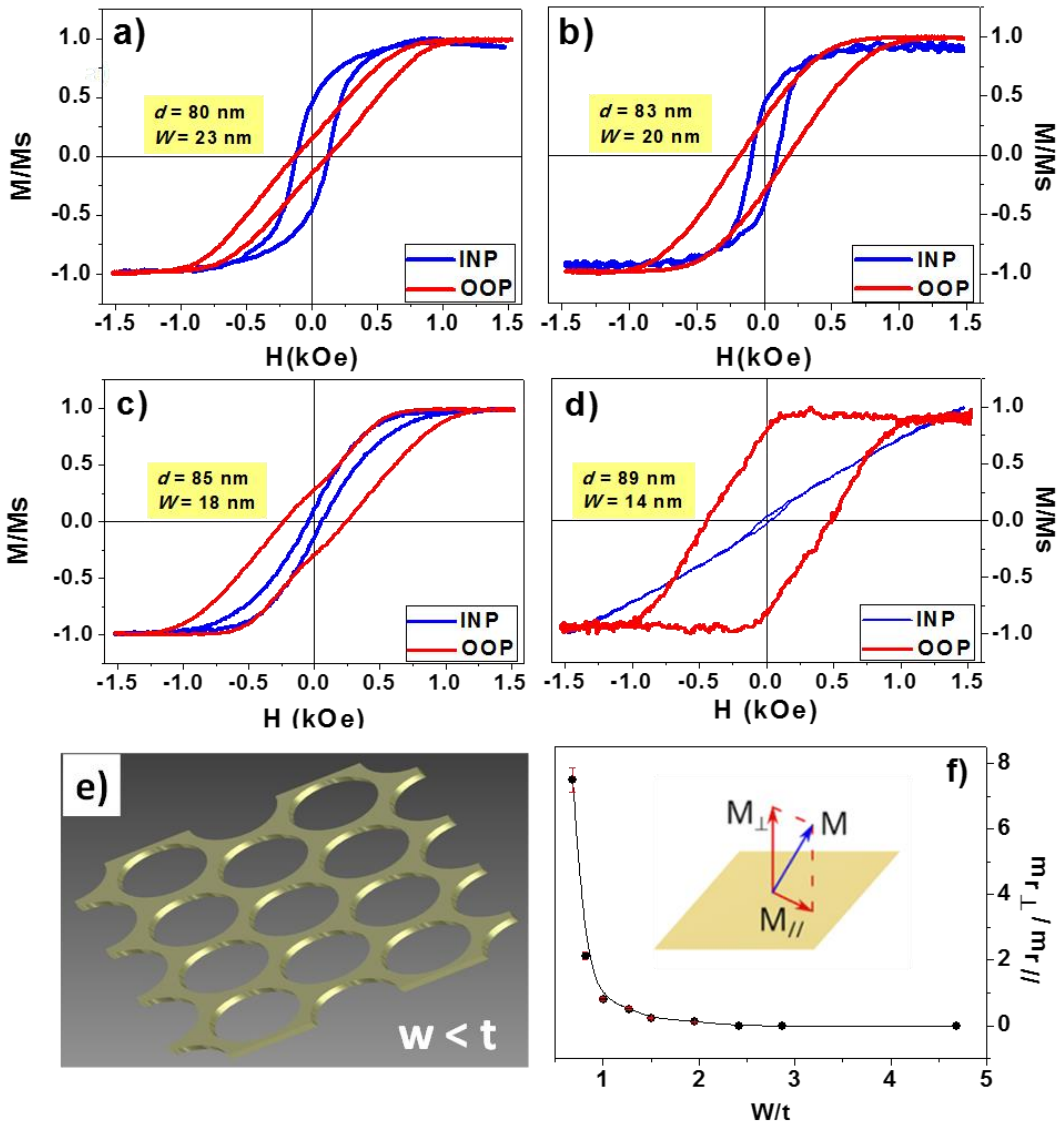


**Figure 6.5:** The INP (blue color) and OOP (red color) Kerr hysteresis loops of Ni antidot arrays thin films with 20 nm in layer thickness and different hole diameter of a) 80 nm, b) 83 nm, c) 85 nm, d) 89 nm and 103 nm of interhole distance. e) 3d sketch for antidot arrays with W ≤ t. f) reduced remanence ratio from OOP to INP directions, $mr_{\perp}/mr_{//}$, calculated from the MOKE hysteresis loops for the Ni antidot samples with different W/t ratio.

From the analysis of the INP and OOP hysteresis loops for a given Ni antidot hole diameter, we calculate the ratio between the component of reduced remanence perpendicular to the sample surface, $m_r\,(OOP)_{\perp}$, and the reduced remanence component parallel to the film surface, $m_r\,(INP)_{//}$. When the ratio between $m_{r\perp}/m_{r//} = 0$ means that magnetization is mainly lying in the INP direction, while $m_{r\perp}/m_{r//} \gg 1$ means that

magnetization is essentially pointing towards the OOP direction [142]. Accordingly, the antidot sample with the maximum size of hole diameter around of 89±1 nm (i. e.: W/t << 1) shows high $mr_{\perp}/mr_{//}$ ratio of 7.5, thus indicating a strong perpendicular anisotropy for this sample. Meanwhile, the other sample showed intermediate perpendicular anisotropy with $m_{r\perp} / m_{r//} = 2$. On the contrary, the continuous thin films and samples with small nanohole diameter show an in-plane magnetic anisotropy with $m_{r\perp}/m_{r//}$ ratio ≈ 0, as plotted in Figure 6.5f.

It should be also of great interest to investigate the dependence of the effective magnetic anisotropy coefficient, $K_{eff}$, and the effective perpendicular magnetic anisotropy energy density ($K_{eff} \times t_{Ni}$) with varying the size of holes diameter. The effective magnetic anisotropy $K_{eff}$, determined from the difference between the areas of the INP and OOP hysteresis loops and that can be calculated by the given expression:[38,114]

$$K_{eff} = K_{OOP} - K_{INP} = \int_{0-OOP}^{M_S} HdM - \int_{0-INP}^{M_S} HdM \qquad (6.1)$$

Where M is the magnetization, $M_S$ denotes the saturation magnetization and H is the applied magnetic field.

A clear trend of $K_{eff}$ depending on the hole diameter can be seen, in Figure 6.6. The larger the INP magnetic surface coverage i.e. continuous thin films and antidot with small d, the greater the effective magnetic anisotropy coefficient. This trend can be explained by a simple model based on the influence of nanoholes edge defects, which reduce the value of the INP magnetic anisotropy locally [71,148,149]. The unpatterned Ni thin film shows an INP effective magnetic anisotropy that is mainly due to the shape anisotropy of the sample. The INP $K_{eff}$ decreases with the increase of nanohole diameter which means that the hard magnetization axis displayed by the continuous unpatterned

thin film that is pointing along the out of plane direction, turns into softer for the antidot samples with larger holes diameter and lower W/t ratios [80,150]. Different "local" shape anisotropy is thus expected, with a stronger contribution of the OOP anisotropy with increasing the size of nanoholes diameter [93]. Navas et al, [93], and Jafaar et al,[93], also reported a decrease in the INP effective anisotropy of Ni continuous thin film from $1.2 \times 10^6$ erg/cm$^3$ to $0.4 \times 10^6$ erg/cm$^3$ for Ni antidots with largest hole diameter (70 nm), with strong contribution of local perpendicular magnetic anisotropy, but still the magnetization lies along the INP direction, which is ascribed to a positive value of $K_{eff}$. Wherever the critical hole diameter is found to be around $d_c \approx 80$ nm, the value of effective magnetic anisotropy decreased to the lowest value ($0.15 \times 10^6$ erg/cm$^3$) and a counterbalance between the parallel and perpendicular components of the magnetic anisotropy contributions takes place. Moreover, a dramatic change in the easy magnetization axis of the sample occurs when the nanohole diameter crossed above its critical size (for a determined value of the ratio W/t ≈ 0.8 and 0.65, and d ≈ 85 and 90 nm, respectively), rotating from the INP toward OOP direction (negative values of $K_{eff}$), when the value of nanoholes diameter overcomes its critical size, $d > d_c$ [41,85].

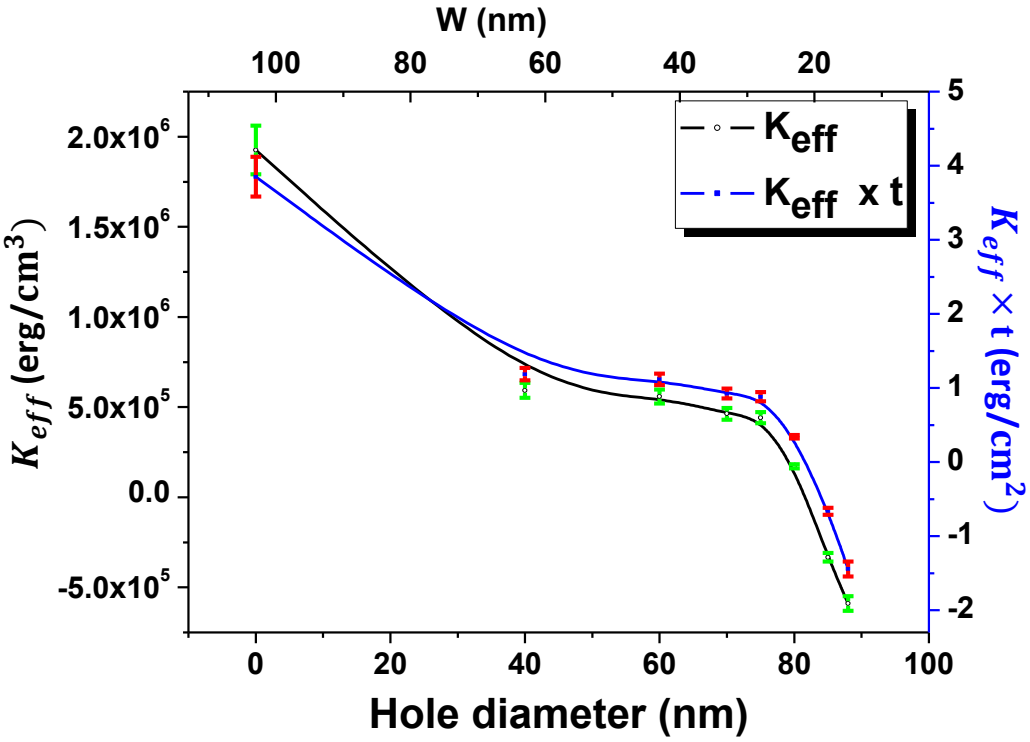


**Figure 6.6:** Effective anisotropy, $K_{eff}$, (left axis), and effective anisotropy energy density, $K_{eff} \times$ t, (right axis), as a function of antidot hole diameter (down scale) and the edge-to-edge distance, W, (top scale) for Ni antidot thin film. Negative values of $K_{eff}$ and $K_{eff} \times$ t correspond to antidot samples with perpendicular (OOP) effective anisotropy. The lines are guides to the eye.

The highest value of the effective perpendicular magnetic anisotropy energy density observed for the Ni antidot thin film with d = 90 nm and t = 20 nm is around ( $K_{eff} \times t \sim 1.44$ erg/cm$^2$), that is more than (7.5-48)-times stronger than that observed for Ni/Pt (0.18 erg/cm$^2$), or Co/Pt (0.2 erg/cm$^2$) and Ni/Pd (0.03 erg/cm$^2$), multilayer thin films with PMA, respectively[136,151,152]. This larger PMA value is also higher than those obtained in Ni/Cu (0.1 to 0.67 erg/cm$^2$) and Fe/MgO (0.1 erg/cm$^2$) continuous thin film with thickness 0.1 to 8.5 nm deposited on epitaxial single crystal exhibiting PMA [148,153,154]. Thus, the high value of the effective perpendicular magnetic anisotropy energy density that has been obtained in this work for the Ni antidot thin film with largest nanoholes diameters, make them as excellent candidates for spintronics applications, bit

patterned magneto-optic perpendicular recording media and magnetic sensors based on template-assisted deposition methods.

By studying the complete magnetic behaviour of the INP and OOP coercivity of the two groups of samples with d and W that are plotted in Figure 6.7, we can distinguish between two main regimes of antidot densities:

Low-Density Antidot (LD-AD) regime: $d < 75$ nm $\Rightarrow W > 28$ nm. The antidots array are well separated from each other, and the expected tendency of the in-plane coercivity, $H_{C//} \propto d$, are followed as plotted in Figure 6.7. Also, the OOP coercivity exhibits the same tendency of the INP coercivity with d but with a slow rate, because of the dominating in-plane magnetization and the magnetization reversal occurs by domain walls movement [44,112].

High-Density Antidot (HD-AD) regime: $d > 75$ nm $\Rightarrow W < 28$ nm. When the distance W among antidots array is small, a change in the dependence of the $H_{C//}$ on nanoholes geometry has been shown, as it sharply decreases with d increasing, in contrast to detected for the linear increase in the LD-AD regime. It is worth noting that the HD-AD regime represents an intermediate state between antidot and dot regimes, as previously reported by other authors [118,128,155]. In this intermediate regime (i.e. HD-AD) the evolution of magnetic parameters such as $m_{r//}$, $K_{eff}$, and $H_{C//}$ changed, as shown in Figures 6.5f, 6.6 and 6.7, respectively, in good agreement with previous works [118,128]. This change is an indication of a change in the magnetization reversal mechanism in the antidot samples, which transfers from domain wall propagation to magnetization rotation of single domain structures [118,128,155]. The reduction of the INP coercivity in this antidot regime is mainly due to the reduced magnetic anisotropy for these samples as shown in Figure 6.6. In addition, as d is further increased (i.e. W

decreases), the inter-distance between adjacent holes becomes narrower, and the film area that has to be nucleated with a reversed domain is smaller [118]. Consequently, $H_{C//}$ decreases. At the same time, the OOP coercivity is increasing rapidly until equals the value of INP coercivity at W = 22 nm, when the hole diameter reaches the critical size, $d_c$.

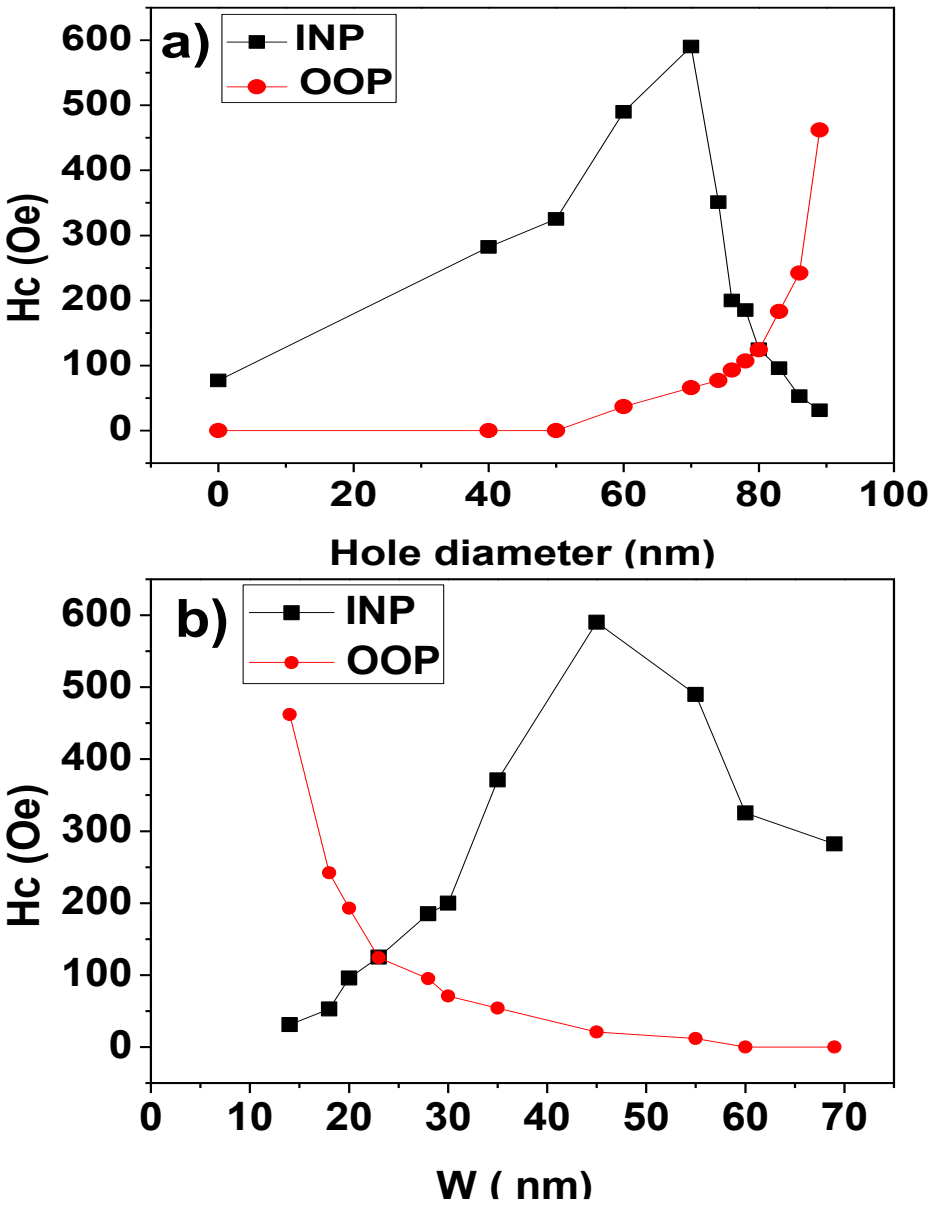


**Figure 6.7:** Coercivity, $H_C$, dependence for the OOP and INP directions of Ni antidot array as a function of a) antidot hole diameter, b) edge-to-edge nanoholes separation, W.

## 6.4 Micromagnetic simulations

Micromagnetic simulations of the Ni thin films and the antidot arrays samples were performed using the 3D object-oriented micromagnetic framework by Mumax$^3$ package with finite element discretization [96]. Under this frame, the ferromagnetic system is divided into cubic cells with a uniform magnetization inside each cell. For the micromagnetic simulations, a grid has been taken as the hexagonally ordered antidots array lattice of 2×2 μm$^2$ with 512×512×16 cells in the x, y and z axes, respectively, with dimensions for the unit cell along each axis of 3.9 nm (x), 3.9 nm (y) and 3.125 nm (z). The ordered Ni antidot arrays are defined by a layer thickness. t = 20 nm, the interspacing distance between neighbouring holes measured centre-to-centre (105 nm), and the nanohole diameter was varied from 40 to 100 nm. Typical values of the magnetic parameters here employed for Ni were: saturation magnetization $M_S$(Ni) = 485 emu/cm$^3$ exchange constant $A_{exch}$ (Ni) = $10^{-6}$ erg/cm and damping coefficient constant of 0.01 [68]. Because of the polycrystalline structure of the Ni thin film, the magnetocrystalline anisotropy at room temperature is negligible, so we set this parameter to zero in the simulations. Through the above micromagnetic simulations, it is considered an external magnetic field applied parallel to the film plane in (x) and (y) directions, as well as in the out of plane direction (z), in order to detect the easy magnetization axis (inset Figure 6.8a), ranging from saturation 4500 Oe to -4500 Oe, passing through the remanent state for both, the INP loops and perpendicular to the film plane for the OOP loops.

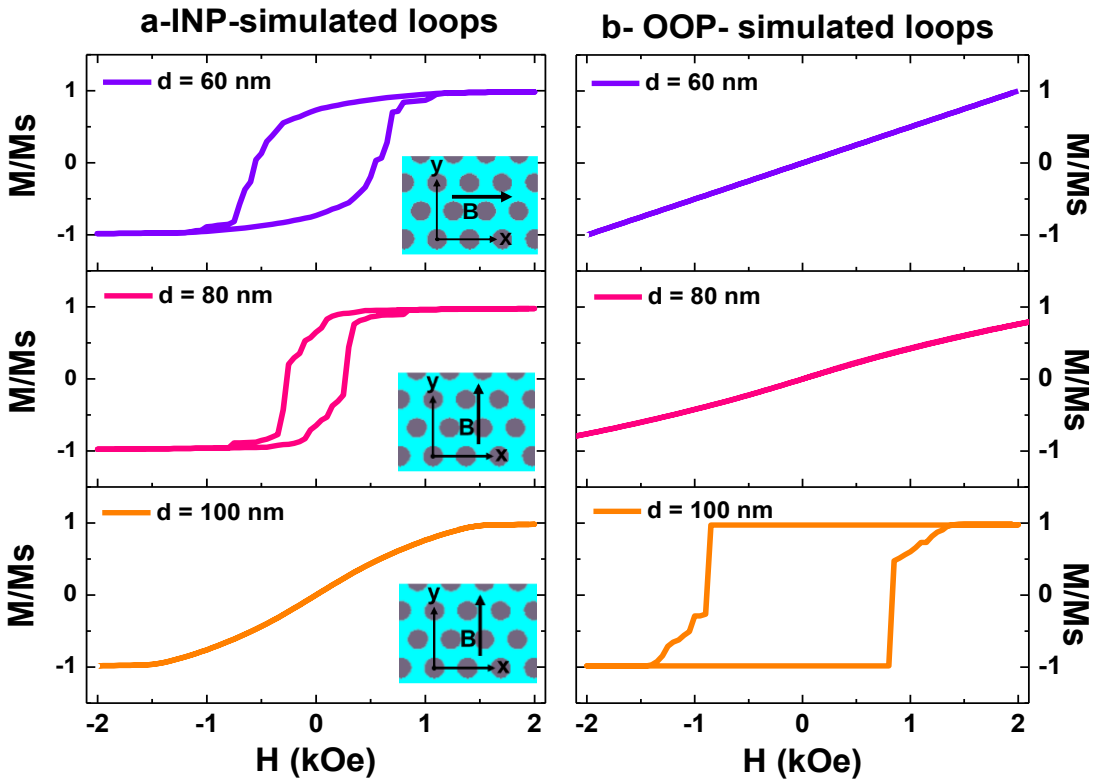


**Figure 6.8:** Micromagnetic simulations of hysteresis loops for a) In-plane (inset: 2×2 μm$^2$ ordered Ni antidot arrays with applied external magnetic field along the x or y direction as indicated in the pictures) and b) Out of plane directions to the Ni antidot arrays thin film plane and with different holes diameter ranging from 60, 80 and 100 nm, but keeping constant the inter-nanohole distance of 105 nm.

Figure 6.8 shows selected INP and OOP hysteresis loops for Ni antidot arrays with W > t (blue loops), W near to t (red loops) and W < t (orange loops) obtained by micromagnetic simulations with the above selected parameters. The simulated hysteresis loops match well within the experimentally measured by MOKE. However, the magnetic parameters derived from the simulated hysteresis loops, such as coercive field and remanence are higher than that extracted from the experimental results. These quantitative differences can be explained in the frame of the micromagnetic model employed for simulations: First, our micromagnetic simulations do not take into consideration thermal disorder effects whereas the experiments were performed at room temperature; second,

for saving computational time, the simulations have been performed by considering only a small portion of the whole system corresponding to an area of 2×2 $\mu m^2$, while our experimental measurements consider the whole sample dimensions of 2×2 $mm^2$. Finally, the differences between experimental data and micromagnetic simulations may be explained by the morphological topography (surface roughness of remaining continuous thin layer between the holes), in addition to the presence of microstructural defects in the samples, such as local hexagonally-ordered hole domains separated by boundaries, which are not included in the simulated, ideally ordered flat surface area. Therefore, the value of the critical size for the nanohole diameter, $d_c$, obtained through micromagnetic simulations, at which the magnetization transition from the INP to the OOP occurred, is 100 nm, that is 11 nm larger than the experimental one. For the simulated loop with hole diameter of 100 nm, the value of perpendicular coercivity $H_{C\perp}$ ~ 820 Oe is almost twice larger than the experimental value of OOP coercivity, $H_{C\perp}$ ~ 445Oe, meanwhile, the $H_{C//}$ is almost zero for both cases. Also, the out of plane reduced remanence obtained from micromagnetic simulations shows a higher value of 0.99 than compared to the experimental one of 0.82 obtained from the measured hysteresis loop of the sample with PMA.

Figure 6.9 shows selected micromagnetic simulation images of magnetic domain structure for Ni antidot samples. The images have been taken at remanent state after saturating the samples along the in-plane easy direction. For samples with d = 40 nm and 60 nm the in-plane easy axis lies in the x direction (i.e. near neighbour holes) where the highest values of $H_C$ and $m_r$ are obtained. Meanwhile, the hard magnetization axis in these samples lies along the y direction (i.e. next near neighbour direction), which shows the lowest values of $H_C$ and $m_r$.

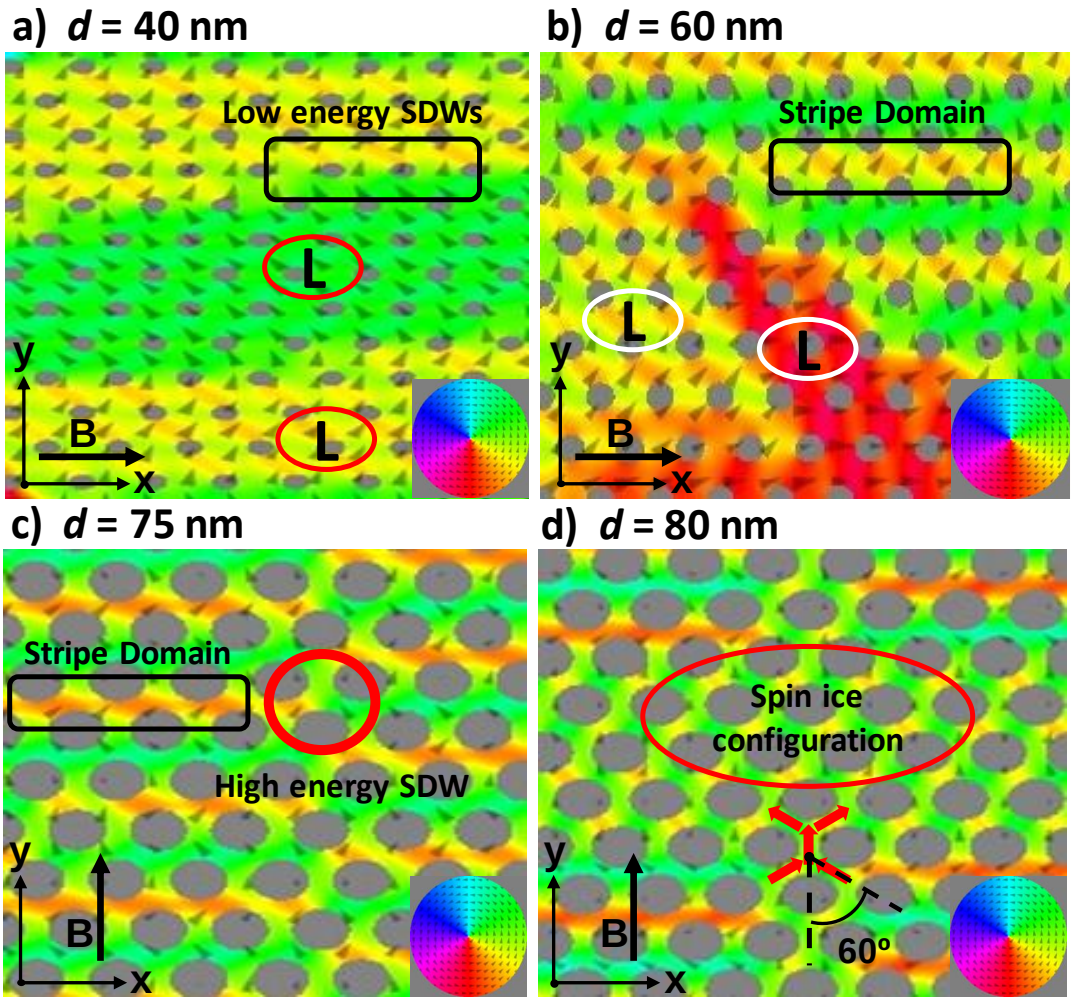


**Figure 6.9**: Micromagnetic simulations of magnetic domain structure at remanent state for Ni antidot samples with nanohole diameter, d, of: a) 40 nm, b) 60 nm, c) 75 and d) 80 nm. The colored maps represent the angle between the INP magnetization component and the x-axis or y-axis, and the arrows provide a qualitative view of the magnetization orientation.

In addition, each two L-structure with different magnetization direction, i.e. different colour, are connected with Low energy super domain wall, LE-SDWs [44]. These LE-SDWs are mainly formed when head-to-tail or tail-to-head configurations of the average magnetization vector take place with low stray field divergence and lower exchange energy terms [44]. For antidot samples with d = 60 nm the magnetic domain structure shows the stripe magnetic domain beside the L-structure [41,44,147,155] as

plotted in Figure 6.9b. For samples with d = 75 nm the magnetic domains with L-structure disappeared, and a stripe domain structure prevails, as show in Figure 6.9c. These magnetic strips domain extended for many hexagonal cells. Also, the strip magnetic domain is connected horizontally with high energy super domain wall, HE-SDWs [44]. These HE-SDWs are mainly form when head-to-head or tail-to-tail configurations of the magnetization vector exist and create a high divergence of stray field and high exchange energy density resulting in local out-of-plane easy magnetization direction in these regions [44]. In addition, the in-plane loops for applied field on x and y direction are approximately the same. By increasing the hole diameter, the magnetic domain structure totally modifies, and the stripe domains tend disappear. As indicated in Figure 6.9d, the magnetic unit cell consists of five domains in accordance to the five bridges between neighbouring holes. The magnetization of the central domain points towards the next nearest neighbour direction, while the other four domains have their magnetization vectors oriented to the next nearest neighbour directions enclosing angles of 60° with respect to the magnetization of the central bridge. As a consequence, the in-plane easy magnetization axis shifts from near neighbour (x direction) to next near neighbour (y direction) [155]. This magnetic state is supposedly very stable, as it not only minimizes the energy of each single vertex in conformance with the spin-ice rules [156], but also the interaction energy between neighbouring vertices. In addition, it is also responsible for the occurrence of a magnetic component perpendicular to the applied magnetics field [157] (i.e., out of plane direction). Therefore, the induced spin-ice magnetic domain structure is causing a reduction of $H_{C//}$ and $m_{r//}$ and an increase of $H_C \perp$ and $m_{r\perp}$, as proved with the experimental result where the $H_{C//}$ reduced above the $d_c$ point.

## 6.5 Conclusions

In summary, the previous results suggest a unified description of the magnetic properties of Ni antidot arrays thin films along the crossover of magnetization from the INP to OOP directions that takes place at the unexpected critical hole diameter $d_c$ = (80 nm). The magnetostatic energy associated to the antidot array, increases with the antidot hole diameter. When the hole diameter is large enough to counterbalance the energy associated to the magnetic poles on the film surface, the preferred direction of magnetization should change from the INP to OOP direction. The magnetization crossover between the INP and OOP direction has been studied for two antidots densities regimes, LD-AD and HD-AD. In addition, the INP effective anisotropy coefficient approaches to zero as there is equivalent energy between the in-plane and out of plane loops. For antidot diameters above $d_c$, a strong effective PMA has been observed. The highest values of effective perpendicular magnetic anisotropy energy density of Ni antidot arrays that have been obtained in this work (1.44 erg/cm$^2$) are more than (7.5-48)-times stronger than that observed for Ni/Pt (0.18 erg/cm$^2$) and Ni/Pd (0.03 erg/cm$^2$) multilayer thin film with PMA, respectively. Furthermore, these findings point toward possibilities to engineer ferromagnetic metal antidots with large perpendicular magnetic anisotropy more than 2-times larger than compared with conventional multi-layered systems. Taking into account the long-standing challenge to promote large PMA in small size spintronic devices, antidot based nanomaterials constitute a benchmark for future spintronic information processing technologies and magneto-optic perpendicular recording patterned media.

# Part II: Ferrimagnetic Antidot Arrays

# Chapter 7: Influence of the array antidot geometry on the magnetic properties of Dy-Fe antidot array thin films.

Both, ferrimagnetic crystalline and amorphous rare-earth transition metal (RE-TM) compounds and their alloys, in either the bulk material or the thin films, have attracted great attention in the past as a potential medium for thermo-magnetic recording and applications in modern ultrafast storage media [158–161]. The importance today of amorphous materials (RE-TM), is found mainly in the field of partial exchange heterostructures [162] giving place to fields of giant exchange bias [163] all-optical switching, magnetic data applications of storage and spintronic due to the fact that they meet all the requirements for an effective magneto-optical material [161,164].The materials most commonly used for these applications are RE-TM alloys, (RE (Tb, Gd, Dy) and TM (Fe, Co, Ni)) [162].Magnetic studies of amorphous $RE_x$-$Fe_{(100-x)}$ thin films indicate that, for the heavier rare-earth metals, these films show a ferromagnetic behaviour [165]. Recently, RE-TM nanostructure based antidots have a strong potential for energy-assisted recording on nanometre-scale magnetic media, magneto-optic perpendicular recording patterned media based on template-assisted deposition techniques and ultrafast spintronic technology [34,37,38,166]

In this Chapter, we pay special attention to the basic magnetic properties (magnetic anisotropy) of Dy-Fe alloy antidot arrays by studying the effect of geometrical parameters as they are, shape of hole, holes ordering and antidot film thickness at room temperature. In addition, the influence of hexagonal symmetry on the thermal magnetic behaviour compared to the continuous thin film samples has been investigated.

## 7.1 Experimental procedure

### 7.1.1 Fabrication of Dy-Fe alloyed antidot thin films

Two series of hexagonally ordered (HAD) and disordered (DAD) antidot arrays of Dy-Fe alloy thin films having an interhole distance $D_{int}$ = 105nm, hole diameter, d, 80±3nm and film thickness varying between 15 nm ≤ t ≤ 60 nm (with increasing steps of each 5 nm), were grown by high-vacuum thermal evaporation technique. The continuous Dy-Fe thin films, CTF, were also deposited on a glass substrate, with the same thicknesses than for the antidots samples, to compare the obtained results.

In order to prepare hexagonally ordered antidot arrays nanoporous alumina membranes were produced by the two-step anodization process [82]. High purity Al foils (99.999%, Goodfellow, Huntingdon, UK), with 0.5 mm of thickness, were cleaned by sonication in ethanol and isopropyl alcohols, then they were electropolished at 20 V in perchloric acid and ethanol solution (1:3 vol., 5 °C) for 5 min. The polished Al foils were employed as starting specimen for the anodic synthesis of nanoporous alumina templates. The two steps electrochemical anodization procedure was done in 0.3 M oxalic acid, at a temperature between 1–3 °C and under a potentiostatic applied voltage of 40 V, measured versus a Pt counter electrode. To obtain the highly ordered nanoporous alumina templates, the samples were immersed in 0.2 M $CrO_3$ and 0.6 M $H_3PO_4$ aqueous solution. This selective chemical etching step leads to the selective removal of the first grown anodic alumina layer, which contained randomly disordered nanopores at its top surface, as shown in Figure 7.1a. For the alumina templates with hexagonal lattice, the second anodization step has been performed during 5 h., allowing the nanopores growth by following a highly self-ordered hexagonal symmetry. In contrast, the disordered nanoporous alumina samples were only submitted to a single anodization step, and

therefore the sample surface remains with randomly distributed nanopores grown during the first stages of the anodization procedure (Figure 7.1a).

Finally, the controlled deposition of the metallic Fe-Dy alloy film formed by highly pure metal pieces of Fe (Goodfellow Limited, England, 99.9% purity) and Dy (Ventron GMBH, Germany, 99.99% purity) was completed by a high vacuum thermal evaporation technique using an E306A thermal vacuum coating unit (Edwards, Crawley, UK) with an ultimate vacuum better than $5.2\times10^{-7}$ mbar, having a diffusion pump backed by rotary pumping together with a liquid nitrogen trap [145]. The pure element metal pieces were placed inside water cooled copper crucible and have been heated by magnetically focused electron beam, 3.1 kV for Fe (crucible1) and 4.5 kV for Dy (crucible2) and electric energy 2.7 kW (Fe) and 2.5 kW for (Dy). The evaporated target metals were deposited on the top-surface of both, the hexagonally ordered and randomly disordered nanoporous alumina membranes, which play the role as templates to obtain the thin films of antidot arrays [77,167]. The control of the film thickness was achieved by using two independent quartz crystal controllers that monitored simultaneously the deposition rates of each evaporation source. The source to substrate distances were maintained constant at about 18 cm and the deposition rate of the Dy-Fe alloy was around 0.1–0.15 nm $s^{-1}$. The experimental details about the deposition conditions have been already reported elsewhere [38,114].

## 7.2 Morphological characterization

### 7.2.1 Scanning Electron Microscopy analysis

The morphological characterization of samples was performed by means of Scanning Electron Microscopy technique (SEM) (JSM 5600, JEOL, Akishima, Tokyo, Japan). Figure 7.1(c to h) shows SEM images for sample surfaces of Dy-Fe antidot arrays

with same hexagonal symmetry and starting values of lattice parameters (d, $D_{int}$), but varying the thickness layer. We should point out that as the thickness of the film increases, the apparent diameter of the nanoholes reduces due to the deposition of magnetic material in the top of the hole until it totally collapses for layer thickness above 60 nm (Figure 7.1h).

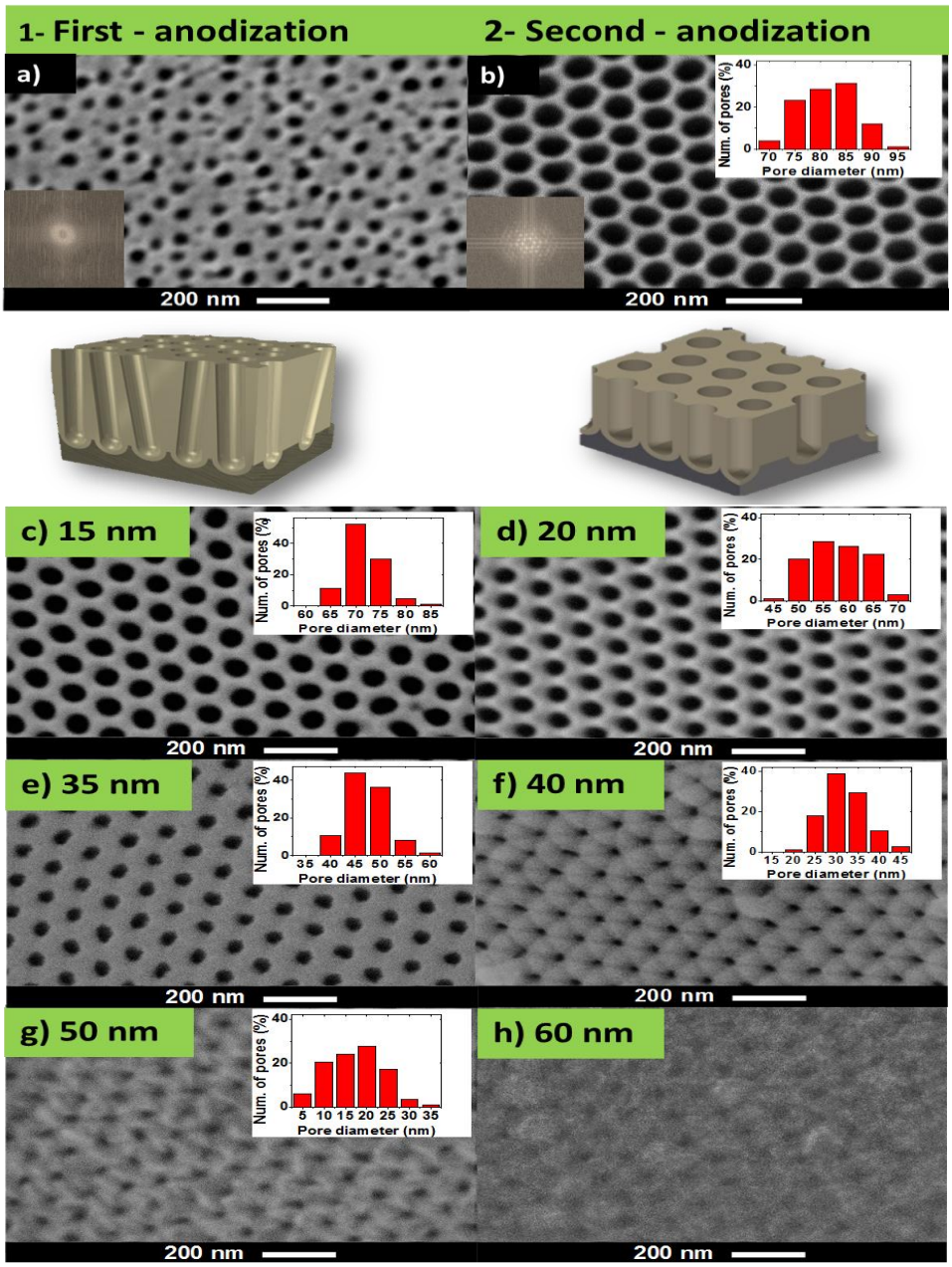


**Figure 7.1:** a) and b) show SEM images for the first anodization the second anodization to obtain the showing only a halo that corresponds to the starting alumina membrane with disordered nanopores and b) illustrating the hexagonal ordering of nanopores). c) to h) SEM images of series from Dy-Fe antidot arrays with layer thickness varying from 15 nm up to 60 nm.

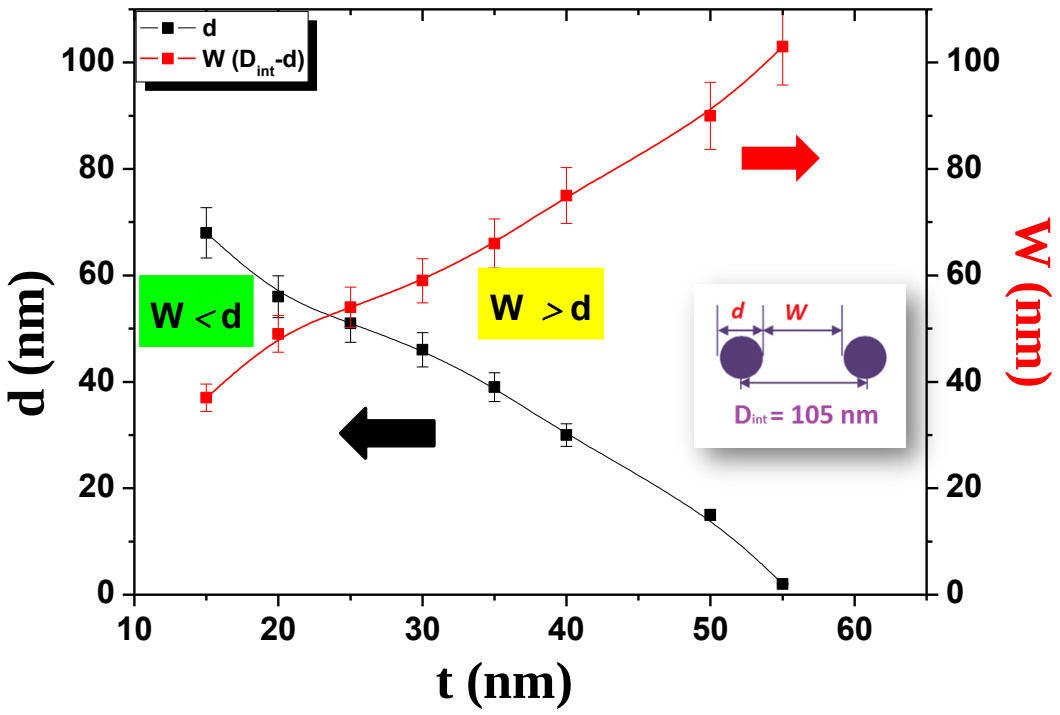


**Figure 7.2:** Dependence of the apparent nanoholes diameter, d, and the edge-to-edge antidot distance, W, of the Dy-Fe antidot arrays with the film thickness grown between 15 nm and 55 nm.

Figure 7.2 shows the correlation between the apparent nano-holes diameters, d, and the edge-to-edge antidot distance, $W = (D_{int} - d)$, with the antidot layer thickness, t, of the Dy-Fe alloy antidots. This change in the apparent nano-hole diameter is due to the deposition of magnetic material in the upper part of the wall of the pore. From Figure 7.2, it can be distinguished two regimes depending on the edge-to-edge antidot distance value. First one corresponds to the case when W is smaller than antidot hole diameter i.e. (thinner samples), and later when W is bigger than the antidot diameter i.e. (thicker films).

Microscopically, the nanoporous alumina templates show a well-defined hexagonal lattice with geometric properties that have been characterized by SEM measurements as shown in Figure 7.1. The hexagonal geometry of the antidot arrays allows distinguishing some characteristic main directions in the samples surface. Firstly,

choosing any particular antidot as the origin, the direction from the origin to the nearest neighbouring antidot, (NN), and secondly, the direction from the antidot of origin to the second nearest neighbour, (NNN), as shown in Figure 7.3a. These directions alternate every 30° all around, with symmetry of 60º. Thus, it can be detected an - angular magnetic anisotropy dependence in the plane of antidot arrays films, related to these two main directions, as it will be discussed in section 7.5.2.1 and also reported elsewhere, [50].

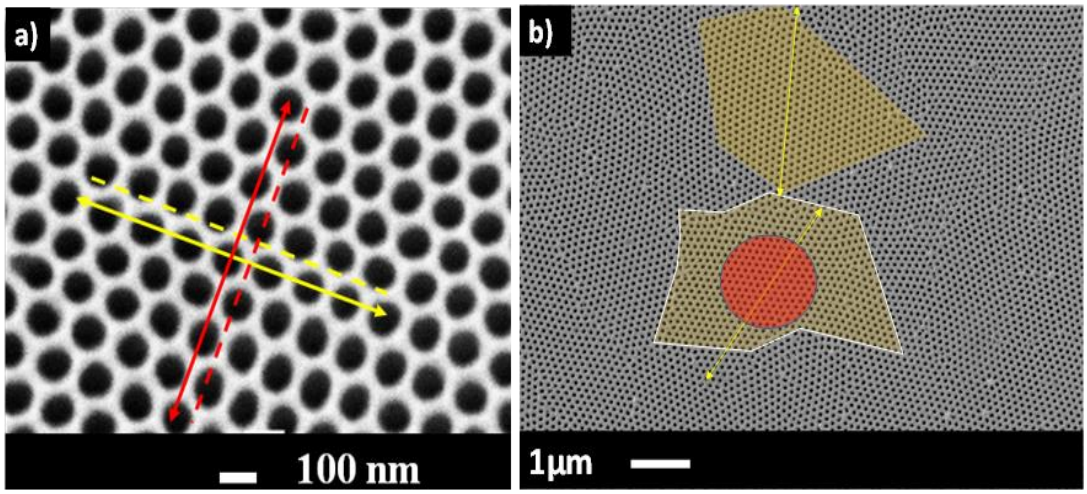


**Figure 7.3:** a) SEM images of antidot substrate illustrating the near neighbour, NN, (double arrow continuous yellow line) and its parallel line (dashed yellow line) along the edges of nanoholes and a next near neighbour, NNN, direction (double arrow continuous red line) and its parallel line (dashed red line). b) SEM image of the surface of an antidots thin film with low magnification.

Macroscopically, at low magnification the nanoporous alumina templates present a hexagonal order of circular holes, divided into geometric hexagonal domains separated by dislocation-like boundaries as shown in Figure 7.3b. The typical size of the hexagonally ordered pore domains is in the range of 4-6 micrometers, as highlighted in different colors in Figure 7.3b. In addition, this figure represents two NN directions, one in each domain, showing the different orientation of the hexagonal order in them. Both NN directions differ in 25º, while if they belonged to the same hexagonal order should match or differ in 60° or 120º. When comparing the lithographed antidot arrays [101]

with the ones obtained using anodic alumina membranes, the latter displays smaller holes sizes and lattice parameters. However, the main drawback relies on the presence of geometric hexagonal domains, while lithographed arrays are mono-domain.

### 7.2.2 Chemical composition

The chemical composition of Dy-Fe antidots thin films and their corresponding continuous thin film are initially calculated from the measurements provided by the controls of crystal quartz balance at the end of the film deposition, used to calculate the ratio of RE/TM in the alloy. To confirm the nominal composition of the alloy, we make a subsequent analysis by energy dispersive x-ray spectroscopy (EDX). The chemical analysis of the spectra of three of these films shows a $Dy_{13}Fe_{87}$ averaged composition as summarized in the Table 7.1 and the measurements agree with the obtained values from the quartz crystal balance.

**Table 7.1:** Atomic percentage of Fe and Dy elemental composition in Dy-Fe thin film.

| EDX Spectrum | Fe (at. %) | Dy (at. %) |
|---|---|---|
| Spectrum1 | 86.9 | 13.2 |
| Spectrum2 | 87.7 | 12.3 |
| Spectrum3 | 87.2 | 12.8 |
| Average | **87.3** | **12.7** |

## 7.3 Microstructural characterization by Transmission Electron Microscopy analysis.

The microstructure of the samples has been studied by high-resolution transmission electron microscopy (HR-TEM) (JEM 2100, JEOL, Akishima, Tokyo, Japan) operating at 200 kV, which was employed to obtain high magnification images of the antidots thin films. For that purpose, the nanoporous alumina membrane that acts as the template for the fabrication of the antidot arrays was previously and selectively dissolved in a 0.5M NaOH solution, thus releasing free-standing flakes of the nanostructured thin film, which were then washed with distilled water and ethanol, deposited into conventional transmission electron microscopy (TEM) copper grid sample holders and dried in air. Selected area electron diffraction (SAED) spectrum was performed to study the microstructure of antidot arrays samples.

The TEM micrograph of the Dy-Fe antidots thin film after being released from the nanoporous alumina membrane is displayed in Figure 7.4, which demonstrates that the nanometric holes successfully replicated the structure of the highly hexagonal ordered nanoporous alumina template, in agreement with the findings revealed by the SEM images. Also, the SAED spectrum, shown as the inset in Figure 7.4a, indicates the amorphous structure of the Dy-Fe alloy, evidenced by the presence of diffused rings and the absence of clear spots in the electron diffraction spectrum.

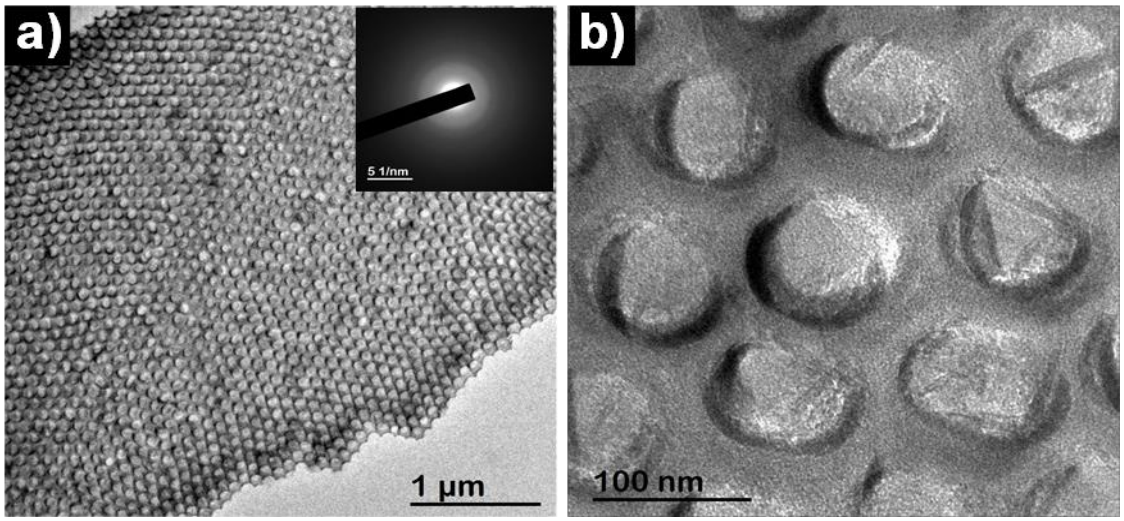


**Figure 7.4:** HR-TEM images of Fe-Dy antidot arrays with 15 nm in layer thickness taken at low (a) and high (b) magnification. The inset in (a) shows the SAED spectrum.

## 7.4 Characterization of magnetic properties

Magnetic properties of Dy-Fe alloy antidot arrays and their corresponding CTF have been determined from the hysteresis loops measured at room temperature on samples surface by the magneto-optical Kerr effect (MOKE), with applied magnetic field of up to ± 0.50T, using the NanoMOKE-3 magnetometer, (Durham Magneto Optics Ltd.). In addition, we have also obtained hysteresis loops of the bulk samples using vibrating sample magnetometer, (VSM-QD-Versalab) with applied magnetic field up to ±3T. In both cases, the magnetic field is applied in the plane of the film, INP, and perpendicular to the film plane (out of plane), OOP, directions. NanoMOKE-3 magnetometer allows obtaining local measurements of the magnetization of the sample by employing a focused laser beam covering an area smaller than 2 microns of diameter, as show in Figure 7.3b. Alternatively, a defocusing lens can be employed in order to widen the laser beam, covering an area of about 0.5 mm radius, thus widening the area of measurement. In other words, it is possible to obtain information from the magnetization of the sample at the microscopic or macroscopic level.

First, we choose the local, microscopic, settings for NanoMOKE-3 magnetometer. We make the measurements for different orientations of the INP applied field. Hysteresis loops were obtained for both types of samples, CTF and antidot arrays films. The angular dependence of the magnetic properties was studied by rotating the samples every 5 degrees in the plane of the sample. To avoid the translational movement due to the sample rotation we firstly localized a specific feature of the sample surface by using the scanning laser microscopy option of Nano-MOKE. Then we start measurement at a well-controlled position located at fixed distance, which is about 10 µm from this point. Therefore, we correct the sample translation displacement that happens because of stage rotation for every measurement at each angle by using the same procedure.

## 7.5 Magnetic behaviour of Dy-Fe continuous thin films and antidots arrays.

### 7.5.1 Magnetic properties of continuous thin films

The INP MOKE hysteresis loop of selected Dy-Fe alloy CTF with thickness ranging from 15 to 60 nm are shown in Figure 7.5 (a, c and e). A clear in-plane uniaxial anisotropy has been observed for all CTF samples, where the angular dependence of the in-plane coercivity, $H_C$ ($\theta$), shows a two-fold symmetry. Actually, amorphous RE-TM alloy possess an anisotropic microstructure when prepared by physical vapor deposition procedure onto room-temperature substrate that is called as *columnar* structure [168,169]. Usually, this columnar micromagnetic structure induces an in-plane uniaxial magnetic anisotropy in the thin films [169]. Therefore, we called this anisotropy as "deposition intrinsic anisotropy" of CTF, which induced during the film deposition. Its values range from $3\times10^6$ to $8\times10^6$ (erg/cm$^3$). Also, this in-plane intrinsic anisotropy is found for all continuous thin films from 15 to 60 nm and it follows two-fold order symmetry. By

increasing the layer thickness of Dy-Fe CTF, the coercivity multiplied by the thin film thickness, $H_C \times t$, increase from 0.75 kOe nm up to 22 kOe nm for samples with layer thickness 15 and 60 nm, respectively. Actually, the parameter ($H_C \times t$) is related to the local domain wall pinning force within the alloy and this observed change with film thickness may well indicate the onset of associated changes in the film morphology [170].

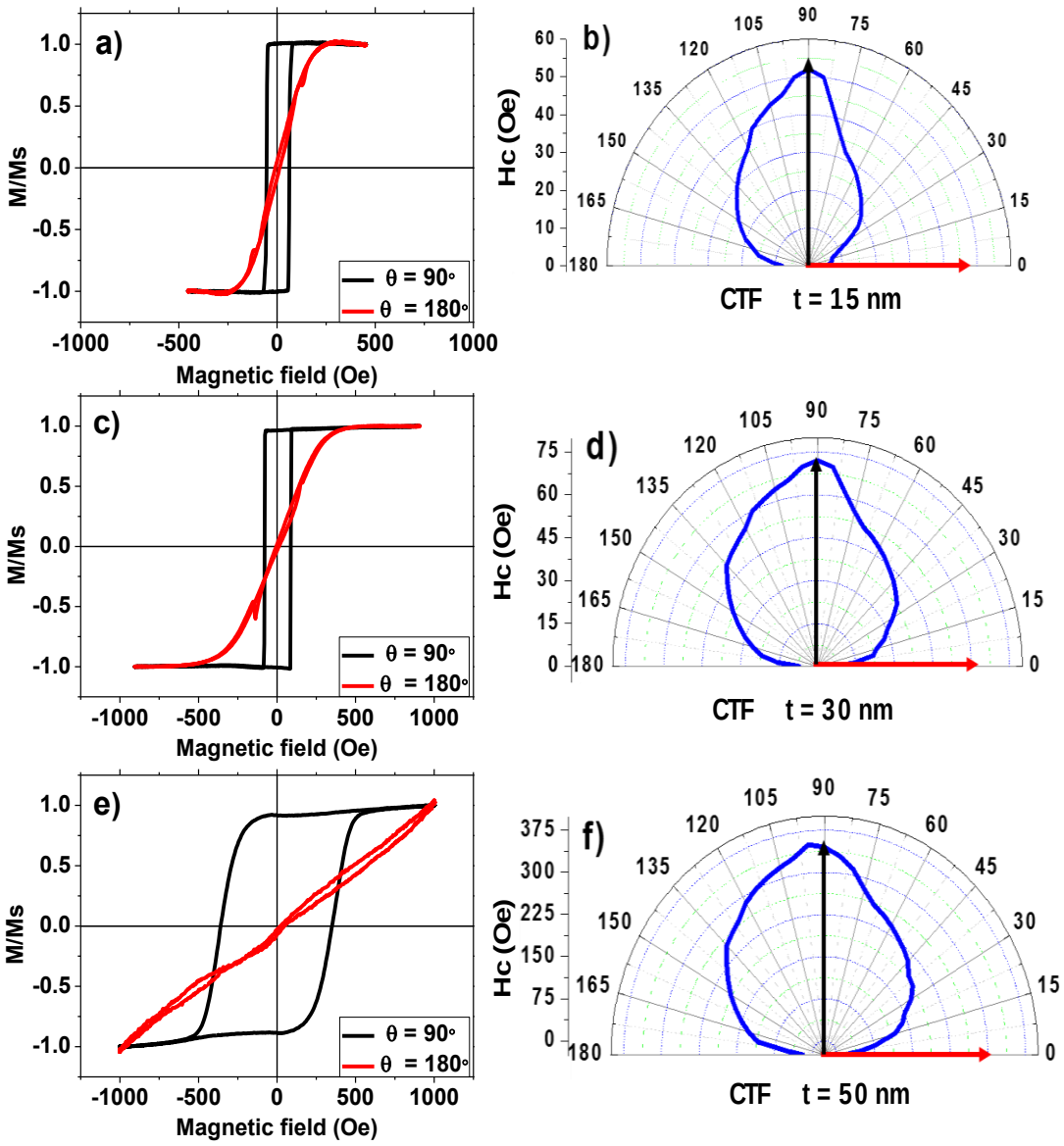


**Figure 7.5:** In-plane hysteresis loops of Dy-Fe alloy continuous thin film and related INP angular coercivity dependence for samples with different thickness: a) and b) 15 nm, c) and d) 30 nm and e) and f) 50 nm, respectively.

### 7.5.2 Antidot arrays thin films

#### 7.5.2.1 Antidots with hexagonal symmetry

The in-plane surface magnetic properties of Dy-Fe antidot arrays samples with different layer thickness are plotted in the Figure 7.6. Several differences in the in-plane magnetic properties of Dy-Fe antidots have been found comparing to their corresponding CTF. Firstly; the in-plane hysteresis loop loses its squareness and becomes wider. Also, the INP loops show multi-step magnetization behaviour which indicates a strong pinning effect and complex magnetization reversal process as shown in Figure 7.6(a, c). This multi-stepped magnetic behaviour indicates that there is a contribution of the out of plane component in the magnetization reversal mechanism [41,119]. Meanwhile, the hysteresis loops of the thicker samples exhibit a single magnetic behaviour as shown in Figure 7.6(e, and g). Secondly, a sharp increase in the $H_C$ for the INP and OOP directions is observed for the antidot thin film comparing to the CTF. The maximum $H_C$ value of 848 Oe has been obtained for antidot samples with layer thickness of 15 nm. This value of coercivity is approximately 17 times larger than the corresponding one for CTF. These differences between CTF and HAD can be explained because of a change in the magnetization reversal mechanism from domain wall movement to super domain wall pinning, as reported in [44], which induced by the nano-holes arrangement, respectively [101,115].

For a best understanding of the magnetic properties of Dy-Fe antidot arrays, we study the angular dependence of the in-plane coercivity and remanence that can be extracted from the INP hysteresis curves. Figure 7.6 (b, d, and f) represents the angular dependence of $H_C$ ($\theta$) for an antidot array thin film with 15, 20, 30 and 50 nm in thickness. We observe for the lower film thicknesses (15 and 20 nm) a six-fold order symmetry of $H_C$ ($\theta$), where the easy anisotropy axis, E. A., (highest values of $H_C$) repeated every 60˚

and the difference between the E.A. and hard anisotropy axis, H.A., is 30˚ as it has been reported also in the case of lithographed antidot arrays [101]. For antidot samples with layer thickness of 30 nm and 35 nm they exhibit an out-of-plane anisotropy (see section 8.6), but when we restrict the study to the in-plane magnetization hysteresis loops a four-fold symmetry of the $H_C$ (θ) has been detected, where the E.A repeated every 90˚ and the difference between the E.A and the H.A is 45˚ as show in Figure 7.6 f. Finally, for thicker antidot samples (50 nm), two-fold symmetry of $H_C$ (θ) was observed, where the E. A. repeated every 180˚ and the difference between the E. A. and the H.A. is 90˚ i.e. the same behaviour of CTF as show in Figure 7.6 h and Figure 7.5. Consequently, we can deduce that there is a critical geometric parameter where the six-fold order symmetry for DyFe antidot thin film can be affected. For HAD samples which size of lattice parameters are below this critical geometrical point, the effective INP local magnetic anisotropy, induced by holes, is dominating and causes the local six-fold order anisotropy for antidot arrays with hexagonal symmetry. Whereas, for antidot samples with $\boldsymbol{W > d}$ i.e. higher than the critical point of the geometrical parameter, the effective in-plane local magnetic anisotropy becomes weaker because of the increasing contribution of intrinsic magnetic anisotropy of the continuous thin film area between the adjacent holes. Therefore, different magnetic anisotropy contribution and symmetry appeared. It is known, that the coercivity of the antidot arrays thin film is determined as a balance between the intrinsic magnetic anisotropy of thin film and the shape anisotropy induced by the arrays of holes [41][50] [114].

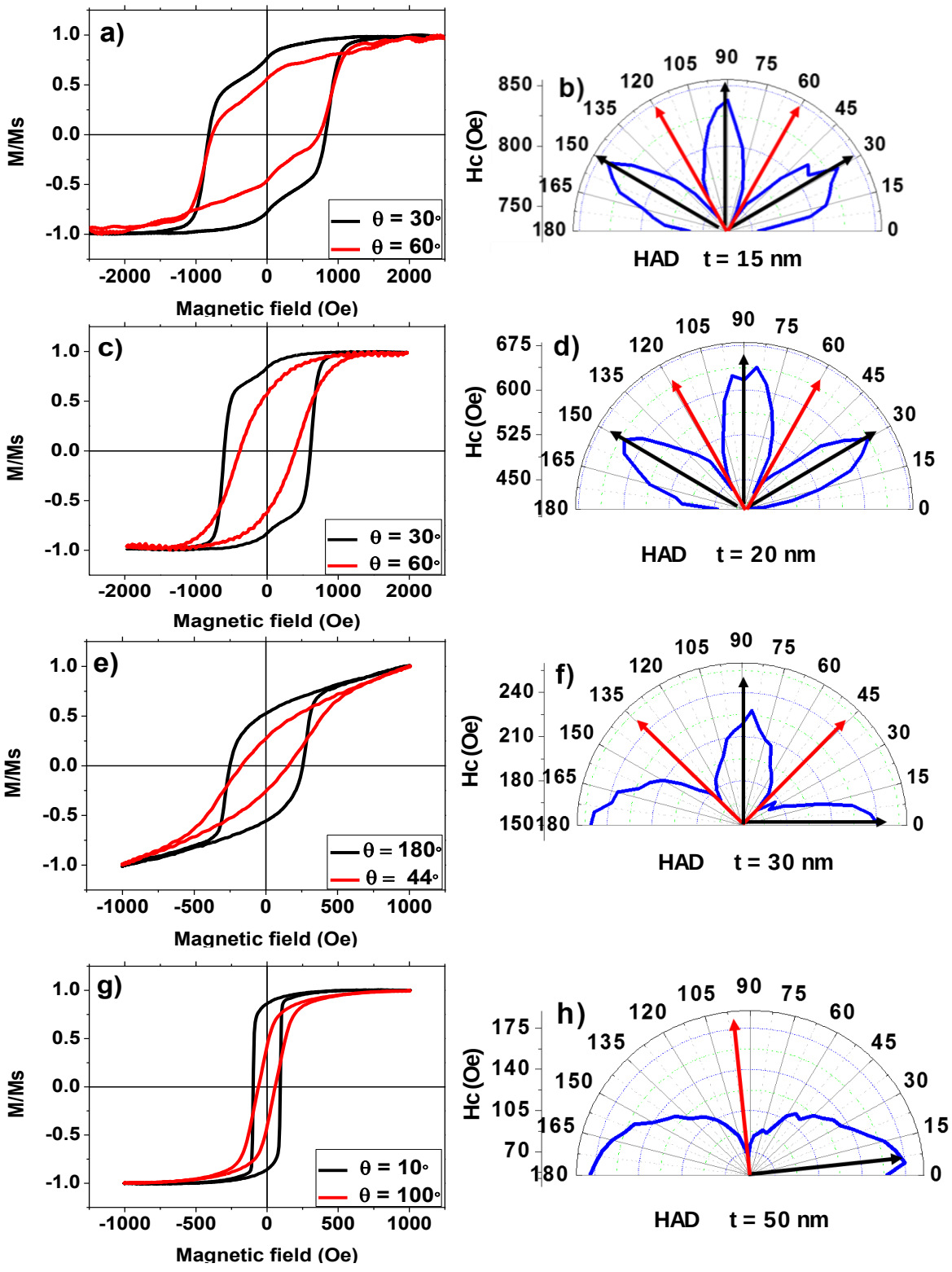


**Figure 7.6:** In-plane hysteresis loops of Dy-Fe alloy antidot thin films with different thicknesses and their related INP angular coercivity dependence for: a) and b) 15 nm, c) and d) 20 nm and e) and f) 50 nm.

If we now choose the macroscopic, or non-local, configuration for the laser beam of the NanoMOKE-3 magnetometer, the area of sample surface covered by the laser beam has a diameter of the order of 0.5 mm. Under these conditions, the MOKE signal is not proportional to the magnetization of only one single domain of antidots with hexagonal ordering, but it is the result of the sum of the MOKE response in multitude of hexagonally ordered domains of antidots. Since the orientation of the hexagonal ordering of antidots will change from one domain to another, the six-fold order symmetry observed in the magnetic properties, i.e. angular dependence of $H_C$ or $m_r$, of a single domain of hexagonal order is not found when using the macroscopic configuration of the laser beam for studying bigger sample surface areas, as shown in Figure 7.7(a, b). These results fit better within two-fold order symmetry, likely due to an in-plane uniaxial anisotropy.

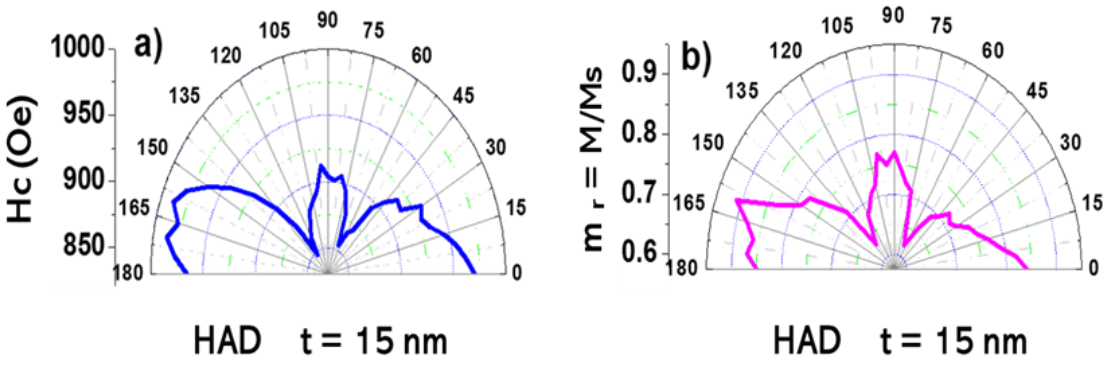


**Figure 7.7:** In-plane angular dependence of, a) $H_C$ and b) $m_r$, for an antidot array thin film with layer thickness 15 nm, when using the macroscopic configuration of the laser beam of NanoMOKE-3 magnetometer.

### 7.5.2.2 Antidot arrays with disordered nanoholes arrangement.

In the case of a DAD array with no hexagonal ordering of nanoholes and therefore no geometric configuration of hexagonal domains of antidot arrays, the local six-fold

order anisotropy is lost. As previously mentioned in the experimental section, the nanopores arrangement obtained at the sample surface after the first anodization process is randomly disordered. The dislocations are inexistent in this kind of arrays, and the sample can be compared to an amorphous packing of antidots with a broad distribution of holes diameter. Figure 7.8(a, c) represents the surface magnetic characterization of DAD with layer thickness of 15 nm and 20 nm, respectively. Firstly, the hysteresis loops of DAD show single step magnetic behaviour in contrast to the multistep magnetic behaviour for the HAD the same layer thickness, as show in Figure 7.8 a, c. Also, the $H_C$ value of DAD is lower than the $H_C$ of the antidot with hexagonal ordering, but still larger than the corresponding value for a CTF with same thickness. This should be due to the domain wall pinning from disordered nanoholes. Secondly, the angular dependence of HC shows a random distribution as shown in Figure 7.8b, because there is not any spatial ordering symmetry in the antidot structure, as shown in Figure 7.1a. However, the $H_C$ angular dependence for the DAD samples with 20 nm show a two-fold order, such as in the case of the symmetry of CTF as show in Figure 7.8d. This means that the induced shape anisotropy by disordered arrays of holes isn't big enough to overcome the intrinsic magnetic anisotropy of CTF.

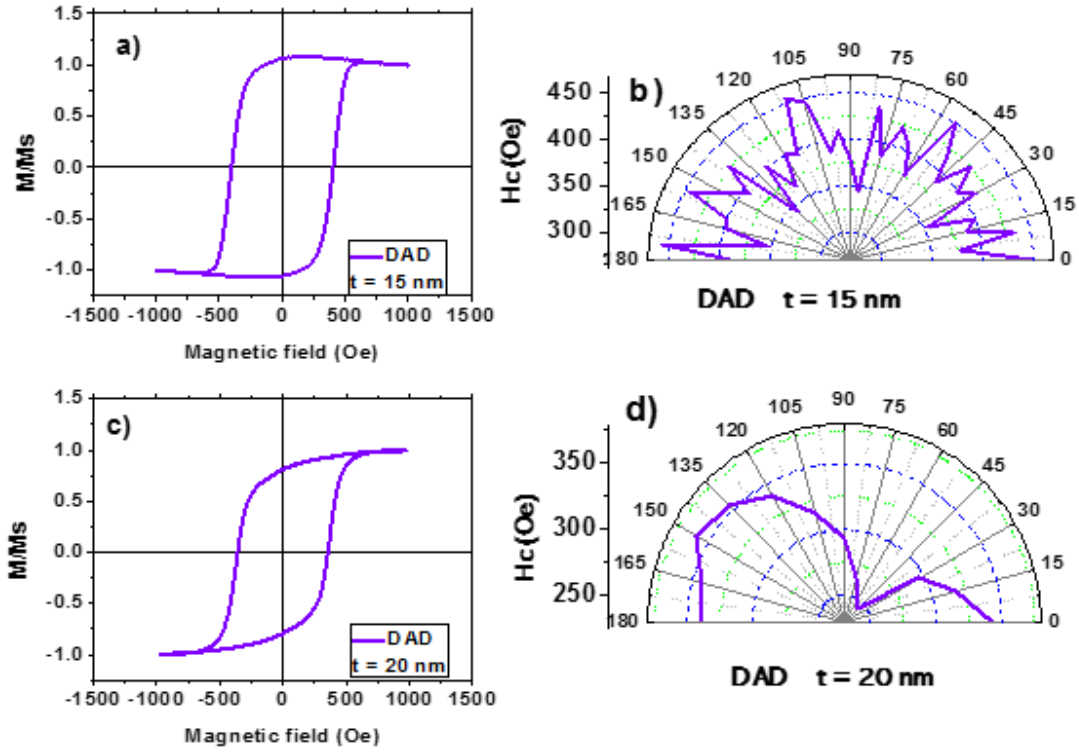


**Figure 7.8:** a) The in-plane hysteresis loops of Dy-Fe alloy disordered antidot array thin film with different thickness and related INP angular coercivity dependence for a) and b) 15 nm, c) and d) 20 nm, respectively.

## 7.6 Effect of hexagonal arrangement of Dy-Fe antidots on Curie temperature.

The effects of thermal activation on the magnetic properties of the Dy-Fe antidot arrays and the continuous thin film, have been studied through the measurements of temperature dependence of the magnetization, M(T), in the temperature range between the room temperature, RT, and 1000 K.

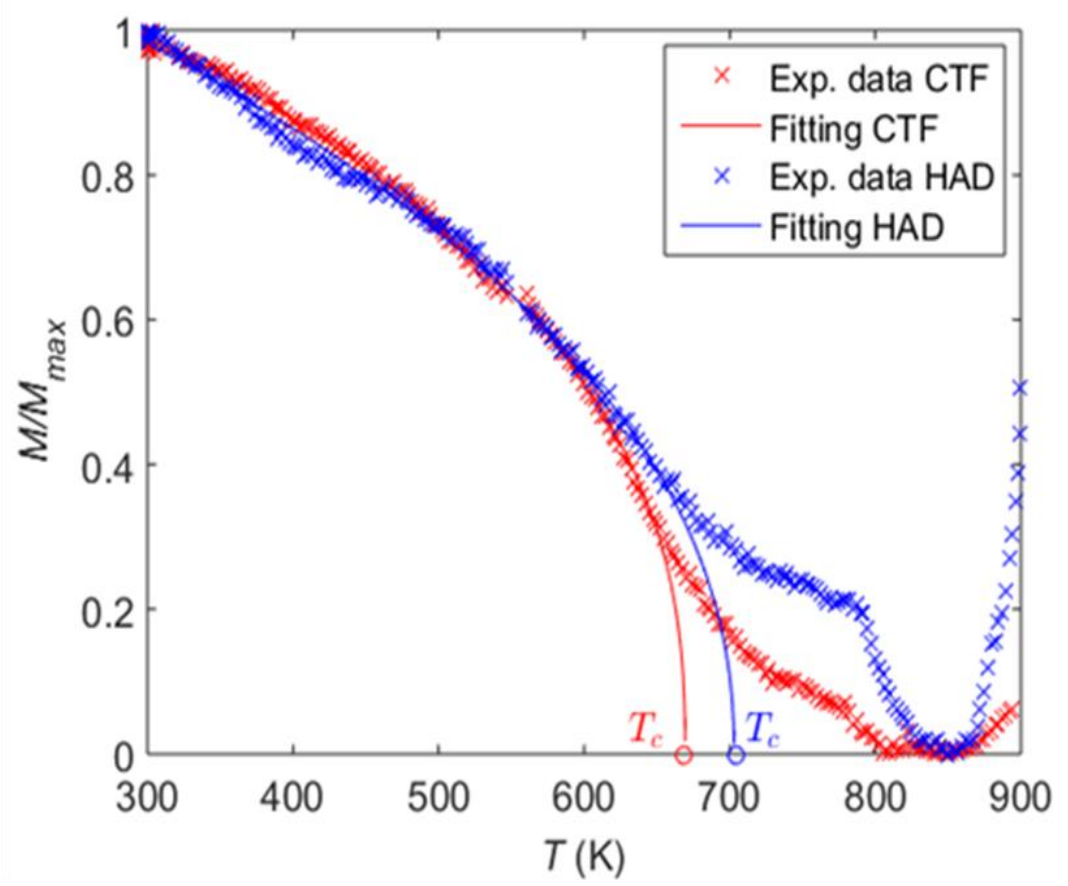


**Figure 7.9:** Temperature dependence of the magnetization in Dy-Fe alloys for both, CTF and HAD samples with layer thickness of 15 nm, measured at constant applied field of 20 kOe along the INP direction.

Figure 7.9 shows the normalized magnetization, M(T)/M(RT), as a function of temperature of Dy-Fe CTF and corresponding antidot arrays film sample with layer thickness of 15 nm obtained by VSM technique. The magnetization curves for HAD and CTF have been obtained after subtracting from the measurements the signal of the corresponding substrates, glass in case of CTF and alumina for HAD. As show in Figure 7.9, from 300 K to 550 K the magnetization behaviour for antidot arrays and CTF shows quite similar trend. An increase in the slope of magnetization curve for the CTF sample with temperature increasing can be observed comparing to HAD sample, ascribed to the existing hexagonal arrangement of antidots which may increase the thermal stability of hosting magnetic materials compare to CTF [171]. A sharp drop in the magnetization

curve of HAD sample has been observed around 785 K because of damage of the supporting alumina membrane when temperature rises. From 820 K to 860 K the magnetization curve for HAD and CTF samples reach the lowest value. Further increasing of temperature, leads to the HAD sample to show a strong paramagnetic phase due to the crystallization under the effect of high temperature annealing for T > 860 K. In order to obtain an accurate value of Curie temperature, $T_C$, a fitting of the magnetization curves plotted in Figure 7.9 was performed according to $[M(T,H) = M_0(\frac{T-T_c}{T_c})^{\beta}]$ [172]. The $T_C$ increases from 669 K for CTF to 710 K in case of antidots array. This increase in the $T_C$ is attributed to the strong pinning effect [33,173] that is induced by the nanoholes of the HAD sample. In addition, the hexagonal arrays of antidot have high thermal stability due to three-dimensional magnetization profile where, the out-of-plane component plays a more important role due to the misaligned magnetic moments at the edge and at the inner wall of the nanoholes [41][80] [120]. Meanwhile, the continuous thin film has only two-dimensional magnetization in-plane components, so the magnetic moments will need more thermal energy to overcome the ordered structure in the case of sample with HAD arrays.

## 7.7 Effect of hexagonal antidot arrays on the temperature compensation point.

The critical properties of the Dy-Fe alloy include the temperature compensation point, $T_{comp}$, near room temperature, RT, where the magnetic moments of the two opposite Dy and Fe sublattices compensate each other. At $T = T_{comp}$, vanishing of magnetization could be achieved for a wide range of compositions. Due to the existence of this compensation temperature, the Dy-Fe alloys continue to attract great interest for

applications in high-density low-current spintronic devices and ultrafast magnetic recording [166].

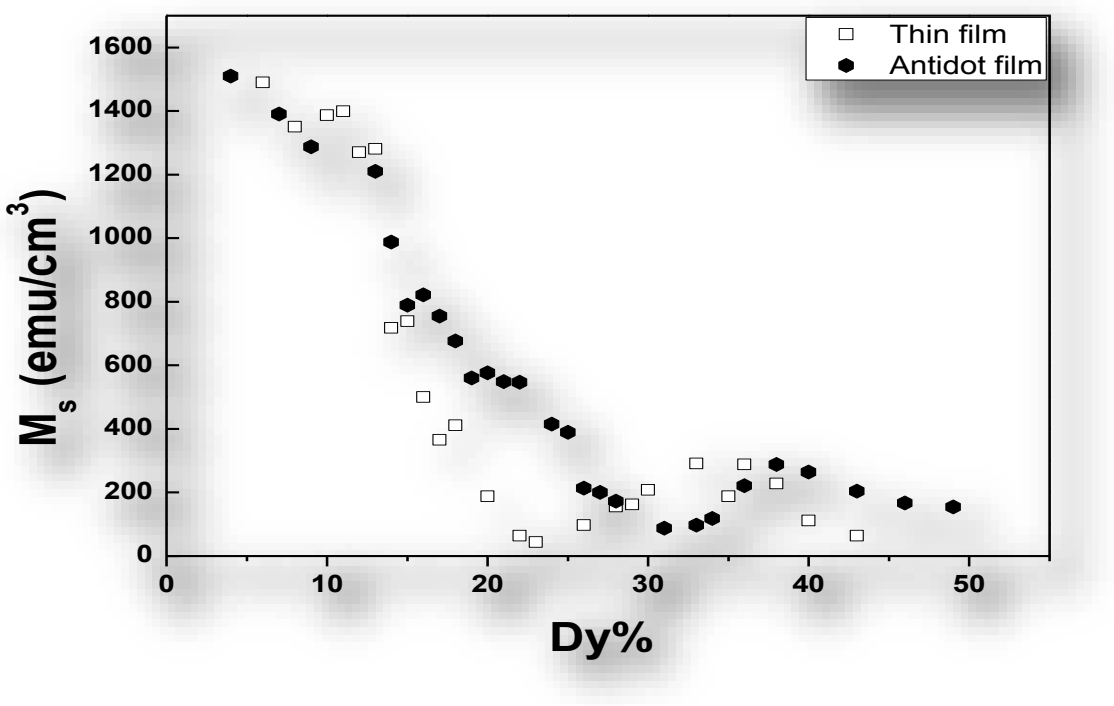


**Figure 7.10**: The magnetization saturation of continuous thin film and antidot arrays film with different Dy percentage measured by VSM at room temperature.

Fig. 7.10 show the compositional dependence of the room temperature saturation magnetization, Ms, obtained from the M-H loops measurements for HAD samples and their corresponding CTF with layer thickness 20 nm. The compensation composition, at which the Ms becomes minimum, is reached at x ≈ 23.5±2 % for the $Dy_xFe_{100-x}$ CTF and 33.5±2 % for the corresponding HAD, respectively. We attribute this shifting in the compensation temperature, $T_{comp}$, in the case of antidot arrays samples to the hexagonal structure of nanoholes and the high surface roughness of alumina template, which influence on the asymmetric composition distribution of Dy and Fe elements around and areas between the nanoholes, and therefore on the resulting magnetic anisotropy.

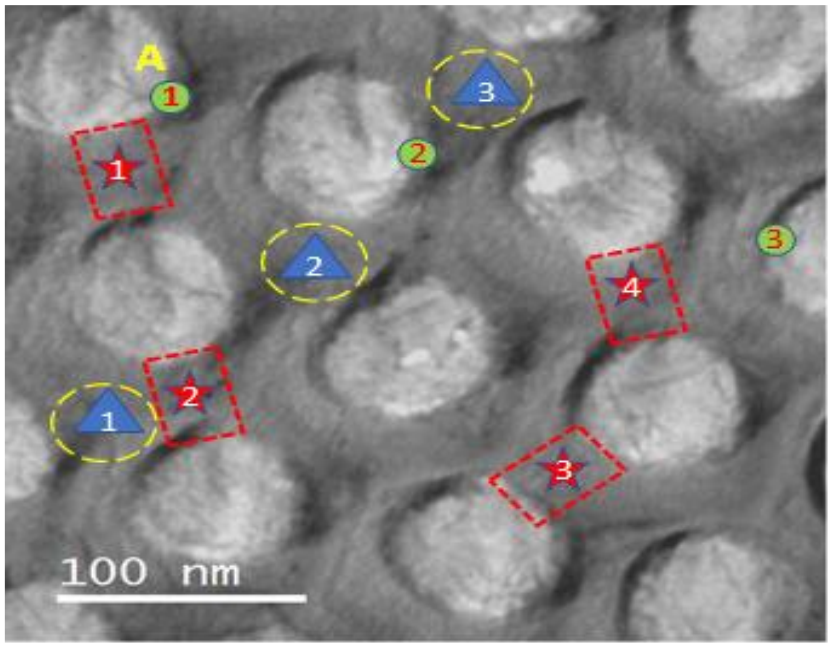


**Figure 7.11**: HR-TEM image for $Dy_{13}Fe_{87}$ antidot arrays showing the Dy and Fe elements distribution for different regions: at the edge of holes (green circle from 1 to 3), area between two holes (red stars from 1 to 4) and the area between three holes (blue triangles from 1 to 3).

Figure 7.11 shows the HR-TEM image with elemental analysis for Fe and Dy at three different places. From the chemical composition analysis, the TEM images around the hexagonal unit cell of the Dy-Fe antidot arrays show that the composition of Dy-Fe alloys differs from place to place. Around the hole's edges, the analysis of the spectra of three regions shows a $Dy_4Fe_{96}$ averaged composition, as summarized in Table 7.2. In contrast, for the area between two holes, W, which are marked as dotted red rectangles in Figure 7.11, the analysis of the four regions shows a $Dy_{28}Fe_{72}$ averaged composition. Finally, for the wide area confined between three holes, the Dy-Fe alloys exhibits an averaged composition of $Dy_{13}Fe_{87}$, which is very near to the continuous thin film values. Thus, the existence of iron rich areas with $Dy_4Fe_{96}$ alloy composition in case of hexagonal antidot arrays may lead to the observed increase in Tc and shifting in $T_{comp}$ as compared to the CTF as plotted in Figure7.9 and Figure7.10.

**Table 7.2**: Atomic percentage of Fe and Dy elements measured at different zones of the antidot sample.

| Region | Area around the holes (green dots) | | Area between two holes (red stars) | | Area between three holes (blue triangles) | |
|---|---|---|---|---|---|---|
| Spectrum | Fe (at. %) | Dy (at. %) | Fe (at. %) | Dy (at. %) | Fe (at. %) | Dy (at. %) |
| 1 | 95.0 | 5.0 | 76.0 | 24.0 | 89.0 | 11.0 |
| 2 | 97.0 | 3.0 | 77.0 | 23.0 | 84.8 | 15.2 |
| 3 | 96.5 | 3.5 | 71.0 | 29.0 | 87.5 | 12.5 |
| **4** | | | 69.0 | 31.0 | | |
| Average | **96.2** | **3.8** | **72.3** | **27.7** | **87.1** | **12.9** |

## 7.8 Tailoring of perpendicular magnetic anisotropy in $Dy_{13}Fe_{87}$ thin films with hexagonal antidot lattice nanostructure

In this section, we will discuss deeply the observation of an interesting phenomenon consisting in the easy magnetization axis transfer from a purely in-plane (INP) magnetic anisotropy to out-of-plane (OOP) magnetization, for a 30 nm thick layer of $Dy_{13}Fe_{87}$ thin film with hexagonal ordering antidots lattice.

### 7.8.1 Atomic Force Microscopy and Magnetic Force Microscopy imaging

Atomic Force Microscopy (AFM) image of the surface topography of the $Dy_{13}Fe_{87}$ antidot sample, with thickness of 30 nm, can be observed in Fig. 7.12a. The nanometric hole structure of the magnetic film is clearly visible and replicates the hexagonal geometry of the nanoporous alumina membrane used as template. The Magnetic Force Microscopy (MFM) signal is mainly sensitive to the out of plane component of the

magnetization and to the magnetic-poles accumulation around the domain walls. The MFM image obtained in the same region in the as prepared state (see Fig. 7.12b) presents a magnetic configuration with positive and negative contrast corresponding to the out of plane magnetization.

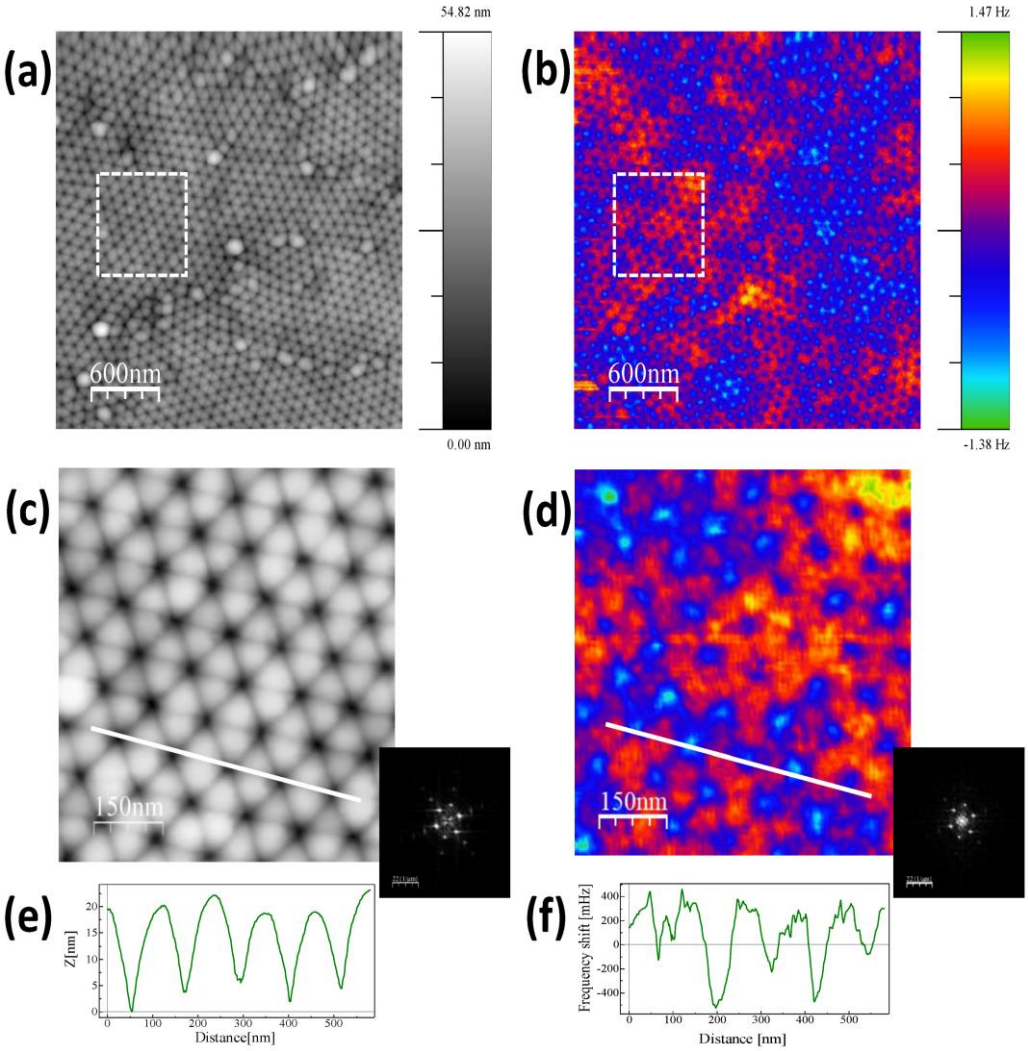


**Figure 7.12**: (a) Topography and (b) MFM images corresponding to the $Dy_{13}Fe_{87}$ antidot sample with 30 nm in thickness. (c) and (d) are zooms corresponding to the marked region in (a) and (b), respectively. Insets correspond to the FFT of each image. (e) and (f) are the profiles obtained along the marked lines in (c) and (d). The magnetic state of the sample is as prepared.

As shown in Fig. 7.12a, the sample presents different morphological domains. Fig. 7.12c and Fig. 7.12d are the zooms performed in the marked regions in Fig. 7.12a and Fig. 7.12b, respectively, in order to study the topographic periodicity and its correlation

with the magnetic signal. The profiles along the NN direction are displayed in Fig. 7.12e and Fig. 7.12f. From the profile scan in Fig. 7.12e, as well as from the Fast Fourier Transform (FFT) data shown in the inset, the lattice constant of the hexagonal antidot arrangement is estimated to be around 110 nm.

The corresponding MFM signal in Fig. 7.12d and Fig. 7.12f allows us to distinguish the superposition of two kind of contrast, one correlated with the topographic signal (always negative) and a positive/negative contrast corresponding to the out of plane magnetization, which is not correlated with the holes position. Notice that the FFT of the MFM signal presents a set of peaks corresponding to the hexagonal lattice and an additional contrast associated to the larger structures. Such component of the magnetic signal is due to the local magnetic anisotropy induced by the antidot thin film geometry.

### 7.8.2 Magneto-optical Kerr effect hysteresis loops

The surface magnetic properties of the $Dy_{13}Fe_{87}$ antidot thin films were characterized making use of the magneto-optical Kerr effect (MOKE), NanoMOKE3 magnetometer, which is sensitive to the longitudinal, transverse and polar magneto-optical Kerr effects; applying up to 0.1250 T by using the quadrupole electromagnet, or 0.5 T with the dipole electromagnet options, respectively.

In the Fig. 7.13a it is represented, in black line, the longitudinal MOKE hysteresis loop of a continuous $Dy_{13}Fe_{87}$ thin film, with 30 nm of thickness. It shows a square shape that matches within an in-plane easy magnetization axis. Red and blue plots in Fig. 7.13a show the longitudinal MOKE hysteresis loops for 30 nm thick antidot thin films, measured along both, the NN and NNN directions, respectively. By comparison of these two later measurements, we can observe that these directions act as easy (NN) and hard (NNN) in-plane magnetization axes. Furthermore, both longitudinal hysteresis loop for

the antidot thin film have lost the squared shape and acquired a shape bending in slope, if compared with the thin film one. This fact shows that the magnetization is not aligned along an easy axis direction, indicating that the easy magnetization axis does not totally lie in the in-plane direction. Coercivity of $Dy_{13}Fe_{87}$ antidots thin film increases also noticeably respect to the one for the continuous film, caused by the presence of holes that act as pinning centers of domain wall displacement [102].

Fig. 7.13b shows the hysteresis loop obtained by polar MOKE for the same antidot thin film with an out-of-plane applied magnetic field. In the polar MOKE configuration, the response of the polar Kerr effect is sensitive to the out of plane magnetization signal, while the longitudinal Kerr measurement is sensitive to any magnetization along the intersection of the film surface plane with the incidence plane of the laser beam, and thus the longitudinal Kerr response is dominated by the in-plane magnetization [174]. The hysteresis loop plotted in Fig. 7.13b shows a dominant magnetization component perpendicular to the surface plane in pseudo magnetization saturation. This fact proves the dropping of the magnetization onto the out of plane direction [174].

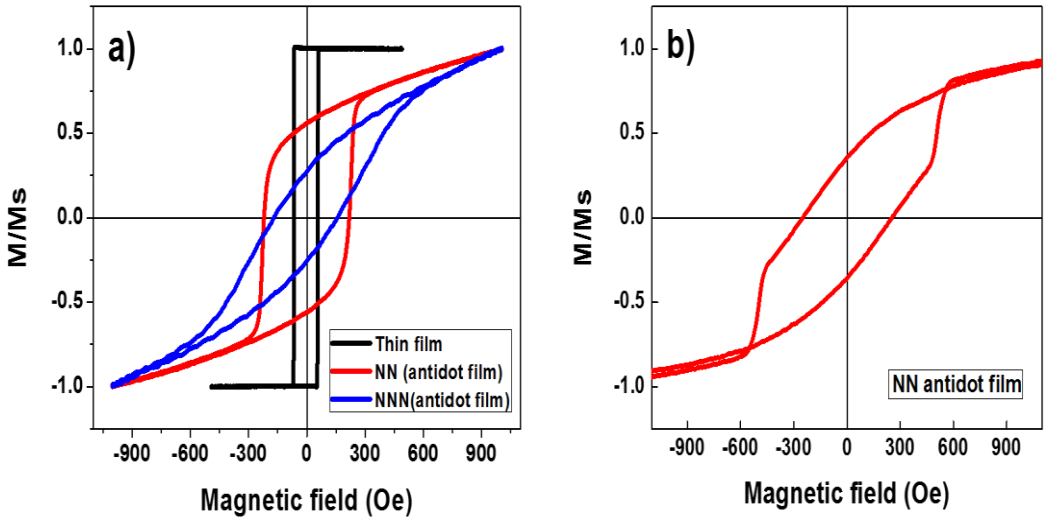


**Figure 7.13:** (a) Longitudinal Magneto-Optical Kerr Effect (MOKE) hysteresis loops of a 30 nm thick $Dy_{13}Fe_{87}$ thin film (black line) and antidot film of the same thickness and composition, measured along the NN (red line) and NNN (blue line) directions of the hexagonal lattice. (b): Polar MOKE hysteresis loop with an out of plane applied magnetic field for the same antidot thin film.

### 7.8.3 Vibrating Sample Magnetometer hysteresis loops

For investigating the whole magnetic behaviour of antidots thin film by measuring the bulk sample hysteresis loops, we use a vibrating sample magnetometer (VSM), at room temperature and with applied magnetic field values up to ±3T. Two common magnetic field configurations were considered for applied magnetic field, in-plane (INP, when magnetic field is applied parallel to film plane) and out of plane (OOP, for the magnetic field perpendicularly applied to film plane). Fig. 7.14a shows both, the INP and OOP hysteresis loops for a continuous thin film and Fig. 7.14 b shows the corresponding ones for the antidot thin film with 30 nm of thickness.

It can be observed from Fig. 7.14a that the magnetization is laying along the INP direction for the DyFe continuous film. In contrast, the OOP magnetization direction for antidot arrays is dominating, as it can be deduced from Fig. 7.14b and confirmed by the polar-

MOKE measurement. In addition, it can be observed the INP shape anisotropy deduced for the continuous thin film, while a more complex magnetic structure is ascribed for the antidot film, where its OOP component clearly differs from that of the continuous film.

It is expected that the anisotropy contributes to the appearance of the OOP magnetization component. The antidot arrays can induce strong local shape anisotropy. This can overcome any kind of intrinsic anisotropy of the host materials; moreover, it prefers an OOP orientation of the magnetization [113]. Also, theoretical studies about the magnetic anisotropy of antidot arrays performed by both, Monte–Carlo simulation [175], and micro magnetic simulation [49] illustrate that the INP preferred orientation of the magnetization in a thin film of antidots array can be, at least partially, lifted. Furthermore, magnetic surface anisotropy contributes to the partial OOP magnetization found here [176].

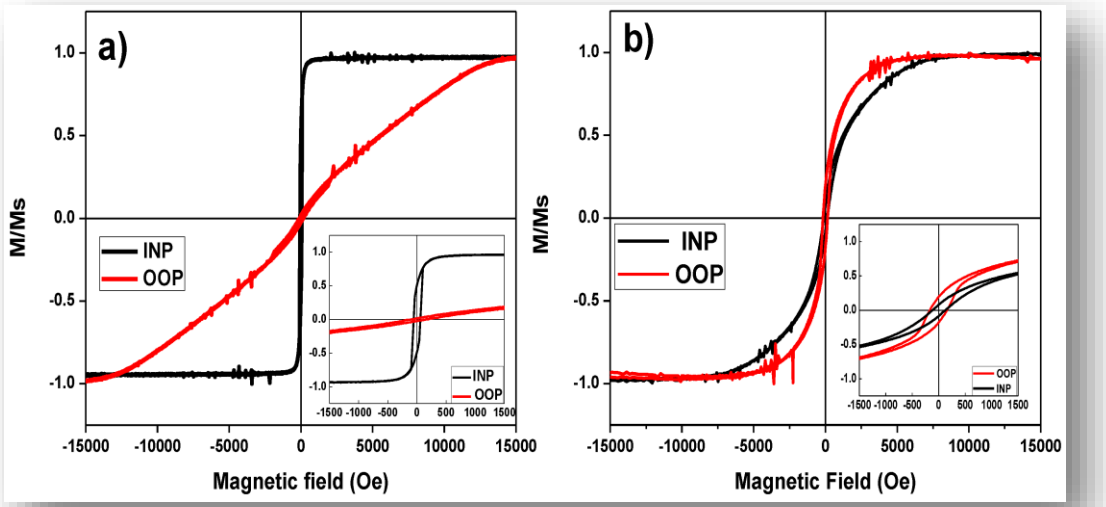


**Figure 7.14:** (a) VSM INP and OOP hysteresis loops for the continuous DyFe thin film with 30 nm thickness. The inset shows the low field scale of INP and OOP hysteresis loops. (b) INP and OOP VSM loops for DyFe antidot films with 30 nm thickness, $D_{int}$= 105 nm and d = 55 nm. The inset shows the magnification in the low field region.

The local geometry of antidot plays a major important role on the magnetization reversal of the antidot films [39][50][80][177]. Such kind of nanoholes arrays is usually described by a parameter named as the antidot aspect ratio, r, which is defined by [41][85]:

$$r = (d + dp)/2t \qquad (7.1)$$

For the current sample the aspect ratio, r, is close to 2.2, that is, the thickness of the films is near to the average antidot diameters and thus the magnetostatic energy accumulated by the surface poles, in the film plane, and that due to magnetic poles on the nanohole surfaces starts to be of the same order of magnitude. Therefore, the magnetization could lie in the OOP direction, as the thickness, t, increases, in order to reduce the whole magnetostatic energy of the system [41][85].

### 7.8.4 Effective magnetic anisotropy for HAD and CTF

Aiming to further investigate the rise of OOP magnetization phenomena, we have estimated the effective in-plane anisotropy, $K_{eff}$, for antidots and thin film samples with the same $Dy_{13}Fe_{87}$ composition and different thicknesses. $K_{eff}$ values were calculated from INP and OOP VSM hysteresis loops according to Refs. [80][114] and they are given by:

$$K_{eff} = \int_{0-OOP}^{M_S} HdM - \int_{0-INP}^{M_S} HdM \qquad (7.2)$$

where M is the magnetization, $M_S$ is the saturation magnetization and H is the applied magnetic field.

Fig. 7.15 (a, b) represents the $K_{eff}$ and the effective anisotropy density, $K_{eff} \times t$, for the Dy-Fe alloy HAD arrays and corresponding CTF with variation of the layer thickness. For CTF samples the $K_{eff}$ and $K_{eff} \times t$ has a nonlinear relationship with the layer thickness.

The maximum value of $K_{eff}$ and $K_{eff} \times t$ occurred at thickness 50 nm, and then start decrease with increasing of layer thickness due to decreasing of magnetization saturation of CTF. It is worth noting, for all CTF samples show a positive $K_{eff}$ and $K_{eff} \times t$ i.e. the CTF have an INP easy magnetization axis.

For the antidot samples, noticeable changes of the effective magnetic anisotropy have been observed. Firstly, $K_{eff}$ values sharply decrease in comparison to the CTF due to the competition between the intrinsic anisotropy and the shape anisotropy of nano-holes and the contribution of out-of-plane magnetic component in the magnetization reversal process [41][120]. Therefore, the magnetic anisotropy crossover from the in-plane to out-of-plane directions have been observed for antidot samples with layer thickness 25 nm and 30 nm (negative values of $K_{eff}$ and $K_{eff} \times t$). It is worth to mention that the values of effective perpendicular magnetic anisotropy energy density, $K_{eff} \times t$, (3.8 erg/cm$^2$) that have been obtained in this work represent an excellent candidate for magneto-optic perpendicular recording patterned media based on template-assisted deposition techniques [38].

Finally, for the thicker HAD samples a positive $K_{eff}$ and $K_{eff} \times t$ with values close to that of the ones for CTF indicates an in-plane easy magnetization axis. A strong relation between the geometric parameter and the effective anisotropy constant is thus confirmed.

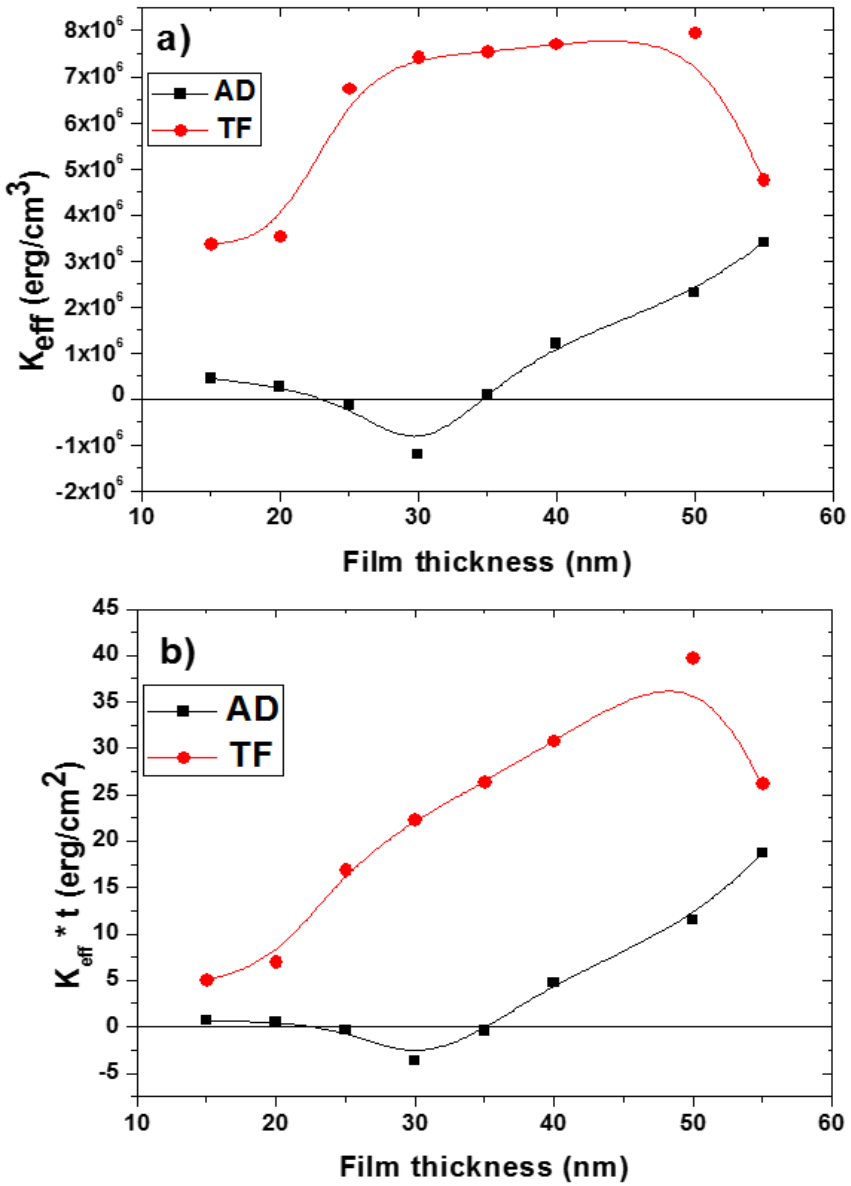


**Figure 7.15:** a) Effective anisotropy $K_{eff}$ and b) effective anisotropy density $K_{eff}$ ×t for Dy-Fe antidot arrays and their corresponding CTF plotted versus the thin film thickness. Negative values of $K_{eff}$ and $K_{eff}$ × t indicate samples with perpendicular (OOP) anisotropy. The lines are guides to the eye.

## 7.9 Conclusion

In summary, the magnetic behaviour of Dy-Fe alloy HAD and corresponding CTF with different layer thickness have been investigated. The dependence of the magnetization reversal mechanism on their lattice parameters have been analysed

through micro-and-macroscopic angular dependence of the in-plane coercivity. The microscopic local measurements of the in-plane magnetic anisotropy for antidot arrays samples show a dramatic change with increasing the layer thickness, exhibiting a magnetization crossover at the thickness value of 25 nm. For thinner antidot sample, W < d, tri-axial magnetic anisotropy has been detected. Meanwhile, for thicker antidot arrays samples, W > d, uniaxial magnetic anisotropy has been observed. A strong correlation between the edge-to-edge distance and the local magnetic anisotropy of Dy-Fe alloy antidot arrays samples has been found. Also, the competition between the intrinsic magnetic anisotropy of CTF and the magnetic shape anisotropy plays the main role on the effective magnetic anisotropy behaviour of the antidot arrays samples. Volume magnetic anisotropy shows a crossover of the magnetic anisotropy from the in-plane easy magnetization axis to out-of-plane easy axis by increasing the layer thickness (at 25 nm). The magnetostatic energy associated to the antidot array increases with the thickness of the thin film. When the thickness increases well enough to counterbalance the energy associated to the magnetic poles on the film surface, then, the preferred direction of magnetization should change from INP to OOP direction. In addition to, by suitable controlling the aspect ratio of antidot parameter, it allows also to tailor the magnetization process of the magnetic materials and controlling the direction of easy magnetization axis from the in plane or out of plane directions. Furthermore, the thermal magnetization behavior for antidot arrays shows an increase in the Curie temperature point comparing to that of the CTF due to the high thermal stability induced by the local hexagonal symmetry of nanoholes arrangement for the HAD sample. Moreover, the inhomogeneous distribution of Fe and Dy elements around and between the holes of antidot arrays play main role to tailor the Tc and room temperature compensation point. Finally, the strong dependence of magnetic properties of Dy-Fe alloys antidot arrays on

the layer thickness and temperature may advance 2D magnetic logic to the third dimension not only at room temperature, but also at high temperature. In addition, these observations can be of high interest for the development of novel magnetic sensors with high uniaxial magnetic anisotropy and for thermo-magnetic recording patterned media based on template-assisted deposition techniques.

# Conclusions

In the present thesis, the magnetic properties of hexagonally ordered antidot arrays within magnetically soft thin films of iron, cobalt, nickel and iron-dysprosium alloy have been studied. The antidot arrays are fabricated by depositing the magnetic materials onto nanoporous alumina membranes with different pore diameters varying in the range between 32±2 to 93±1 nm but fixed inter-hole distance, $D_{int}$ as described in Chapter 3.

In Chapter 4 the global and local magnetization behavior of Fe and Co-based antidot thin films is strongly dependent on holes diameter and layer thickness. For thinner AD samples the in-plane $H_{C//}$ shows four-fold symmetry, meanwhile the thicker AD samples show two-fold symmetry. Unexpected $H_C$ tendency behaviour with 1/t has been observed, which predict an interesting magnetic behaviour for AD samples with large nanohole diameter and thin layer thickness.

In Chapter 5, the magnetic properties of FM-antidot arrays with different hole diameter, (d = 35 to 89 nm) but fixed inter-hole distance ($D_{int}$ = 105 nm) and layer thickness (t = 20 nm) have been investigated. The current results suggest a unified description of the magnetic behaviour of FM-antidot arrays thin films along the change of $H_{C//}$ behaviour with W that takes place at the critical edge-edge distance ($W_{c//}$ = 18 nm, 24 nm and 33 nm) for Fe, Co and Ni-antidot arrays samples, respectively. At the critical edge-edge distance, the maximum $H_{C//}$ have been obtained due to two different complex domain wall pinning mechanism, between the neighbouring holes and inner wall of the holes. The multistep magnetic behaviour observed for antidot samples with $W < W_{c//}$ reveals the strong contribution of the OOP component in the magnetization reversal mechanism of the FM-antidots thin films. The magnetization crossover from the INP to OOP directions has been detected for antidot samples with $W_{c\perp} < R_{Coh}$ at 22 nm and 14 nm for Ni and Co antidot arrays samples, respectively.

In Chapter 6, deeply study of Ni antidot arrays with different nanohole diameter and fixed $D_{int}$ and t has been performed. The previous results suggest a unified description of the magnetic properties of Ni antidot arrays thin films along the crossover of magnetization from the INP to OOP directions that takes place at the unexpected critical hole diameter $d_c$ = (80 nm). The magnetostatic energy associated to the antidot array, increases with the antidot hole diameter. When the hole diameter is large enough to counterbalance the energy associated to the magnetic poles on the film surface, the preferred direction of magnetization should change from the INP to OOP direction. The magnetization crossover between the INP and OOP direction has been studied for two antidots densities regimes, LD-AD and HD-AD. In addition, the INP effective anisotropy coefficient approaches to zero as there is equivalent energy between the in-plane and out of plane loops. For antidot diameters above $d_c$, a strong effective PMA has been observed. The highest values of effective perpendicular magnetic anisotropy energy density of Ni antidot arrays that have been obtained in this work (1.44 erg/cm$^2$) are more than (7.5-48)-times stronger than that observed for Ni/Pt (0.18 erg/cm$^2$) and Ni/Pd (0.03 erg/cm$^2$) multilayer thin film with PMA, respectively. Furthermore, these findings point toward possibilities to engineer ferromagnetic metal antidots with large perpendicular magnetic anisotropy more than 2-times larger than compared with conventional multi-layered systems. Taking into account the long-standing challenge to promote large PMA in small size spintronic devices, antidot based nanomaterials constitute a benchmark for future spintronic information processing technologies and magneto-optic perpendicular recording patterned media.

In Chapter 7, we pay special attention to the basic magnetic properties (magnetic anisotropy) of Dy-Fe alloy antidot arrays by studying the effect of geometrical parameters as they are, shape of hole, holes ordering and antidot film thickness at room temperature.

In addition, the influence of hexagonal symmetry on the thermal magnetic behaviour compared to the continuous thin film samples has been investigated. The antidot arrays introduce a noticeable change in the morphology and magnetic behavior of the magnetic thin film if we compare it with that one of the continuous thin film. It makes to increase the magnetostatic energy associated to the antidot arrays, if the magnetization lies in the film plane. This energy might be due to the appearance of magnetic poles on the antidot surfaces in competition with the magnetostatic energy due to the magnetic poles on the film surface when the magnetization is OOP. The magnetostatic energy associated to the antidot array, increases with the film thickness. When the thickness increases enough to counterbalance the energy associated to the magnetic poles on the film surface, and then the preferred direction of magnetization should change from INP to OOP direction. In addition, by suitable controlling the aspect ratio of antidot parameter, it allows also to tailor the magnetization process of the magnetic materials and controlling the direction of easy magnetization axis from the in plane or out of plane directions.

Finally, the strong dependence of magnetic properties of Dy-Fe alloys antidot arrays on the layer thickness and temperature may advance 2D magnetic logic to the third dimension not only at room temperature, but also at high temperature. In addition, these observations can be of high interest for the development of novel magnetic sensors with high uniaxial magnetic anisotropy and for thermo-magnetic recording patterned media based on template-assisted deposition techniques.

# Conclusiones

En la presente tesis, se han estudiado las propiedades magnéticas de matrices ordenadas de antidots con geometría hexagonal dispuestas en películas delgadas magnéticamente blandas de hierro, cobalto y níquel, así como de la aleación de hierro-disprosio. Las matrices de antidots (AD) se fabricaron depositando los materiales magnéticos sobre membranas de alúmina nanoporosa con diferentes diámetros de poro que varían en el rango desde 32 ± 2 nm hasta 93 ± 1 nm, pero manteniendo fija la distancia entre nanohuecos, $D_{int}$, como se describe en el Capítulo 3.

En el Capítulo 4, se estudia el comportamiento de la imanación global y local de las películas delgadas de antidots basadas en Fe y Co, y cómo depende en gran medida del diámetro de los nanohuecos, d, y del espesor de la película delgada, t. Para muestras de AD más delgadas, el campo coercitivo, $H_C$, medido en el plano de la muestra presenta una simetría cuádruple, mientras que las muestras de AD más gruesas presentan una simetría doble. Se ha observado un comportamiento inesperado en la tendencia del $H_C$ con 1/t, que predice un comportamiento magnético interesante para muestras de AD con un gran diámetro de antidot y lámina de espesor muy delgado.

En el Capítulo 5, se han investigado las propiedades magnéticas de las matrices FM-antidot con diferentes diámetros de nanohueco (d = 35 a 89 nm), pero distancia fija entre nanohuecos ($D_{int}$ = 105 nm) y espesor de la película delgada (t = 20 nm). Los resultados obtenidos sugieren una descripción unificada del comportamiento magnético de las matrices delgadas de FM-antidot a lo largo del cambio del comportamiento de $H_{C//}$ con respecto a la distancia entre bordes de antidots, $W = D_{int}$-d, que tiene lugar para un valor de distancia crítica borde-borde entre nanohuecos, $W_{c//}$ = 18 nm, 24 nm y 33 nm para las muestras de Fe, Co y Ni-antidots, respectivamente. En la distancia crítica borde-borde entre nanohuecos, se ha obtenido el máximo de $H_{C//}$ debido a dos mecanismos

complejos diferentes de fijación de la pared del dominio, entre los nanohuecos vecinos y la pared interior de los nanohuecos. El comportamiento magnético de inversión de la imanación en varias etapas observado para las muestras de antidots con $W < W_{c//}$ revela la fuerte contribución del componente perpendicular o fuera del plano de la muestra (OOP), en el mecanismo de inversión de la imanación de las películas delgadas FM-antidots. El cruce que experimenta la imanación desde la dirección contenida en el plano de la muestra (INP) hacia la dirección perpendicular (OOP), se ha detectado para muestras de antidots con $W_{c\perp} < R_{Coh}$ de 22 nm y hasta 14 nm, para muestras de arreglos de antidots de Ni y Co, respectivamente.

En el Capítulo 6, se ha realizado un estudio profundo de las matrices de antidots de Ni con diferentes diámetros de nanohueco pero manteniendo $D_{int}$ y t fijos. Los resultados obtenidos sugieren una descripción unificada de las propiedades magnéticas de los arreglos antidots de Ni en películas delgadas a lo largo del salto de la imanación desde las dirección INP a la OOP, que tiene lugar para el valor de diámetro crítico del nanohueco $d_c = 80$ n). La energía magnetostática asociada a la matriz de antidots aumenta con el diámetro del nanohueco de antidot. Cuando el diámetro del nanohueco es lo suficientemente grande como para contrarrestar la energía asociada a los polos magnéticos en la superficie de la película, la dirección preferida de la imanación cambia desde la dirección INP a la OOP. El salto de la imanación desde la dirección INP a la OOP se ha estudiado para dos regímenes diferentes de densidades de antidots, LD-AD y HD-AD. Además, el coeficiente de anisotropía efectivo INP se aproxima a cero, ya que existe una energía equivalente entre los ciclos en el plano y fuera del plano. Para diámetros de antidot por encima de $d_c$, se ha observado la aparición de una anisotropía magnética perpendicular efectiva, PMA, fuerte. Los valores más altos de densidad de energía de la anisotropía magnética perpendicular efectiva de los arreglos de antidots de

Ni que se han obtenido en este trabajo (1.44 erg / $cm^2$) son más de 7.5-48 veces más elevados que los observados para Ni/Pt (0.18 erg / $cm^2$) y en películas delgadas multicapa de Ni/Pd (0.03 erg/$cm^2$) con PMA, respectivamente. Además, estos hallazgos apuntan hacia posibilidades para diseñar películas delgadas de antidots de metales ferromagnéticos con elevada anisotropía magnética perpendicular, de hasta más de 2 veces mayor que en comparación con los sistemas multicapa convencionales. Teniendo en cuenta el futuro desafío del almacenamiento de big-data con el fin de promover sistemas con elevada PMA en dispositivos espintrónicos de pequeño tamaño, los nanomateriales basados en estructuras ordenadas de antidots constituyen un punto de referencia para las futuras tecnologías de procesamiento de información para espintrónica y en los medios de grabación perpendicular magneto-óptica.

En el Capítulo 7, prestamos especial atención a las propiedades magnéticas básicas (anisotropía magnética) de las matrices de antidots de aleación Dy-Fe al estudiar la influencia de los parámetros geométricos sobre ellas, como son, la forma del nanohueco, el orden espacial de los nanohuecos y el espesor de la película del antidot, a temperatura ambiente. También se ha investigado la influencia de la simetría hexagonal del ordenamiento de los antidots sobre el comportamiento magneto-térmico en comparación con las muestras de película delgada continua. Las matrices de antidots introducen un cambio drástico en la morfología y el comportamiento magnético de la película delgada magnética si lo comparamos con el de la película delgada continua. Se incrementa la energía magnetostática asociada a las matrices de antidots si la imanación se encuentra en el plano de la película. Esta energía podría deberse a la aparición de polos magnéticos en las superficies del antidot, en competencia con la energía magnetostática asociada a los polos magnéticos de la superficie de la película cuando la imanación se dispone según la dirección OOP. Además, la energía magnetostática asociada a la matriz

de antidots aumenta con el espesor de la película. Cuando el grosor aumenta lo suficiente como para contrarrestar la energía asociada a los polos magnéticos en la superficie de la película delgada, la dirección preferente de la imanación (o eje de imanación fácil) debe cambiar de la dirección INP a la de OOP. Además, el control adecuado de la relación de aspecto de los parámetros de red de los antidots, también permite adaptar el proceso de imanación de los materiales magnéticos y controlar la dirección del eje de fácil imanación desde las direcciones en el plano o fuera del plano de la muestra. Finalmente, la fuerte dependencia encontrada de las propiedades magnéticas de las matrices de antidots de las aleaciones Dy-Fe respecto al espesor de la película delgada y la temperatura, permite emplear dichos materiales en dispositivos de lógica magnética 2D, y aumentar su avance hacia sistemas 3D, no solo a temperatura ambiente, sino también a alta temperatura.

Estas observaciones pueden ser de gran interés para el desarrollo de nuevos sensores magnéticos con alta anisotropía magnética uniaxial y para dispositivos de espintrónica basados en técnicas de deposición asistida mediante el empleo de plantillas patrón nanoestructuradas.

# References


[1] Barth J V., Costantini G and Kern K 2005 Engineering atomic and molecular nanostructures at surfaces *Nature* **437** 671–679

[2] Nie Z, Petukhova A and Kumacheva E 2010 Properties and emerging applications of self-assembled structures made from inorganic nanoparticles *Nat. Nanotechnol.* **5** 15–25

[3] Lenk B, Ulrichs H, Garbs F and Münzenberg M 2011 The building blocks of magnonics *Phys. Rep.* **507** 107–36

[4] Erb D J, Schlage K and Röhlsberger R 2015 Uniform metal nanostructures with long-range order via three-step hierarchical self-assembly *Sci. Adv.* **1** e1500751

[5] S. A. Wolf, D. D. Awschalom, R. A. Buhrman, J. M. Daughton, S. von Molnár, M. L. Roukes A Y C and D M T 2001 Spintronics: a spinn-based electronics vision for the future *Science.* **294** 1488–95

[6] Igor Zutic J F and S D S 2004 Spintronics: Fundamentals and applications *Rev. Mod. Phys.* **76** 323

[7] Wolf S A and Treger D 2000 Spintronics: A new paradigm for electronics for the new millennium *IEEE Trans. Magn.* **36** 2748–51

[8] M. N. Baibich, J. M. Broto, A. Fert, F. Nguyen Van Dau, F. Petroff, P. Etienne, G. Creuzet, A. Friederich and J C 1988 Giant Magnetoresistance of Fe and Cr Magnetic Superlattices *Phys. Rev. Lett.* **61** 2472–5

[9] G. Binasch, P. Griinberg, F. Saurenbach W Z 1989 Enhanced magnetoresistance in layered magnetic structures with antiferromagnetic interlayer exchange *Phys.*

*Rev. B* **39** 4828–30

[10] Reig C and Cubells-Beltrán M D 2013 Giant magnetoresistance (GMR) magnetometers *Smart Sensors, Measurement and Instrumentation* pp 103–31

[11] Materials A S 1994 Magnetic Field Sensors Using GMR Multilayer *IEEE Trans. Magn.* **30** 4608–10

[12] Prinz G A 1998 Magnetoelectronics *Science.* **282** 1660–3

[13] Khizroev S and Litvinov D 2004 Perpendicular magnetic recording : Writing process *J. Appl. Phys.* **95** 4521–37

[14] Weller D and Doerner M F 2000 Extremely High-Density Longitudinal Magnetic Recording Media *Annu. Rev. Mater. Sci.* **30** 611–44

[15] Weller D and Moser A 1999 Thermal effect limits in ultrahigh-density magnetic recording *IEEE Trans. Magn.* **35** 4423–39

[16] Brown W F 1963 Thermal fluctuations of a single-domain particle *Phys. Rev.* **130** 1677–86

[17] Bertotti G 1998 *Hysteresis in Magnetism*

[18] Guimarães A P 2009 Magnetic recording *NanoScience and Technology* (Berlin, Heidelberg: Springer) pp 173–84

[19] Hu Y, Wu H, Meng Y, Bogy D B, Hu Y, Wu H, Meng Y and Bogy D B 2017 Nanoscale thermal analysis for heat-assisted magnetic recording Nanoscale thermal analysis for heat-assisted magnetic recording *J. Appl. Phys.* **122** 134303

[20] Zhou N, Xu X, Hammack A T, Stipe B C, Gao K, Scholz W and Gage E C 2014

Plasmonic near-field transducer for heat-assisted magnetic recording *Nanophotonics* **3** 141–155

[21] Wang S, Wang Y and Victora R H 2013 Shingled magnetic recording on bit patterned media at 10 Tb/in2 *IEEE Trans. Magn.* **49** 3644–7

[22] Hwang E, Negi R and Kumar B V K V 2010 Signal Processing for Near 10 Tbit/inP Density in Two-Dimensional Magnetic Recording (TDMR) *IEEE Trans. Magn.* **46** 1813–6

[23] Spectra 2017 Digital Data Storage Outlook *Spectra White Pap.*

[24] Stamps R L, Breitkreutz S, Åkerman J, Chumak A V, Otani Y, Bauer G E W, Thiele J, Bowen M, Majetich S A, Kl M, Dempsey N M and Hillebrands B 2014 The 2014 Magnetism Roadmap **47** 333001–29

[25] Zhang S, Gilbert I, Nisoli C, Chern G W, Erickson M J, O'Brien L, Leighton C, Lammert P E, Crespi V H and Schiffer P 2013 Crystallites of magnetic charges in artificial spin ice *Nature* **500** 553–557

[26] Heyderman L J 2013 Artificial spin ice: Crystal-clear order *Nat. Nanotechnol.* **8** 705–706

[27] Laguna M F, Balseiro C A and Nori F 2001 Vortex structure and dynamics in kagome´ and triangular pinning potentials *Phys. Rev. B* **64** 104505

[28] Yu H, Duerr G, Huber R, Bahr M, Schwarze T, Brandl F and Grundler D 2013 Omnidirectional spin-wave nanograting coupler *Nat. Commun.* **4** 2702

[29] Mandal R, Barman S, Saha S, Otani Y and Barman A 2015 Tunable spin wave spectra in two-dimensional $Ni_{80}Fe_{20}$ antidot lattices with varying lattice symmetry

*J. Appl. Phys.* **118** 3910

[30] Palma J L, Pereira A, Álvaro R, García-Martín J M and Escrig J 2018 Magnetic properties of $Fe_3O_4$ antidot arrays synthesized by AFIR: Atomic layer deposition, focused ion beam and thermal reduction *Beilstein J. Nanotechnol.* **9** 1728–34

[31] Lange M, Van Bael M J, Moshchalkov V V. and Bruynseraede Y 2002 Asymmetric flux pinning by magnetic antidots *J. Magn. Magn. Mater.* **240** 595–597

[32] E. T. Filby, A. A. Zhukov, P. A. J. de Groot, M. A. Ghanem, P. N. Bartlett and V V M 2006 Shape induced anomalies in vortex pinning and dynamics of superconducting antidot arrays with spherical cavities *Appl. Phys. Lett.* **89** 2503–6

[33] Tripathy D and Adeyeye A O 2011 Perpendicular anisotropy and out-of-plane exchange bias in nanoscale antidot arrays *New J. Phys.* **13** 023035

[34] Kulesh N A, Vázquez M, Lepalovskij V N and Vas'Kovskiy V O 2018 Antidot patterned single and bilayer thin films based on ferrimagnetic Tb-Co alloy with perpendicular magnetic anisotropy *Nanotechnology* **29** 5301

[35] Bran C, Gawronski P, Lucas I, Del Real R P, Strichovanec P, Asenjo A, Vazquez M and Chubykalo-Fesenko O 2017 Magnetic hardening and domain structure in Co/Pt antidots with perpendicular anisotropy *J. Phys. D. Appl. Phys.* **50** 5003

[36] Mengotti E, Heyderman L J, Rodríguez A F, Nolting F, Hügli R V and Braun H 2011 Real-space observation of emergent magnetic monopoles and associated Dirac strings in artificial kagome spin ice *Nat. Phys.* **7** 68–74

[37] Ünal A A, Valencia S, Radu F, Marchenko D, Merazzo K J, Vázquez M and

Sánchez-Barriga J 2016 Ferrimagnetic $DyCo_5$ Nanostructures for Bits in Heat-Assisted Magnetic Recording *Phys. Rev. Appl.* **5** 064007

[38] Salaheldeen M, Vega V, Ibabe A, Jaafar M, Asenjo A, Fernandez A and Prida V M 2018 Tailoring of Perpendicular Magnetic Anisotropy in $Dy_{13}Fe_{87}$ Thin Films with Hexagonal Antidot Lattice Nanostructure *Nanomaterials* **8** 227

[39] Vavassori P, Gubbiotti G, Zangari G, Yu C T, Yin H, Jiang H and Mankey G J 2002 Lattice symmetry and magnetization reversal in micron-size antidot arrays in Permalloy film *J. Appl. Phys.* **91** 7992

[40] Wang C C, Adeyeye A O and Lin C C 2004 Magnetic properties of lithographically defined rectangular antidot permalloy arrays *J. Magn. Magn. Mater.* **272–276** e1299–e1300 Magnetic

[41] Merazzo K J, Castán-Guerrero C, Herrero-Albillos J, Kronast F, Bartolomé F, Bartolomé J, Sesé J, Del Real R P, García L M and Vázquez M 2012 X-ray photoemission electron microscopy studies of local magnetization in Py antidot array thin films *Phys. Rev. B - Condens. Matter Mater. Phys.* **85** 184427

[42] Torres L, Lopez-Diaz L and Alejos O 2000 Micromagnetic analysis of recording processes in periodic antidot arrays: Interaction between adjacent bits *J. Appl. Phys.* **87** 5645

[43] Deshpande N G, Seo M S, Jin X R, Lee S J, Lee Y P, Rhee J Y and Kim K W 2010 Tailoring of magnetic properties of patterned cobalt antidots by simple manipulation of lattice symmetry *Appl. Phys. Lett.* **96** 122503

[44] Hu X K, Sievers S, Janke V and Schumacher H W 2011 Classification of super domains and super domain walls in permalloy antidot lattices *Phys. Rev. B* **84**

024404

[45] Papaioannou E T, Kapaklis V, Patoka P, Giersig M, Fumagalli P, Garcia-Martin A, Ferreiro-Vila E and Ctistis G 2010 Magneto-optic enhancement and magnetic properties in Fe antidot films with hexagonal symmetry *Phys. Rev. B - Condens. Matter Mater. Phys.* **81** 054424

[46] Mengotti E, Heyderman L J, Nolting F, Craig B R, Chapman J N, Lopez-Diaz L, Matelon R J, Volkmann U G, Kläui M, Rüdiger U, Vaz C A F and Bland J A C 2008 Easy axis magnetization reversal in cobalt antidot arrays *J. Appl. Phys.* **103** 07D509

[47] Schneider T, Langer M, Alekhina J, Kowalska E, Oelschlägel A, Semisalova A, Neudert A, Lenz K, Potzger K, Kostylev M P, Fassbender J, Adeyeye A O, Lindner J and Bali R 2017 Programmability of Co-Antidot lattices of optimized geometry *Sci. Rep.* **7** 41157

[48] Manzin A, Barrera G, Celegato F, Coïsson M and Tiberto P 2016 Influence of lattice defects on the ferromagnetic resonance behaviour of 2D magnonic crystals *Sci. Rep.* **6** 22004

[49] Van De Wiele B, Manzin A, Vansteenkiste A, Bottauscio O, Dupré L and De Zutter D 2012 A micromagnetic study of the reversal mechanism in permalloy antidot arrays *J. Appl. Phys.* **111** 053915

[50] Wang C C, Adeyeye A O and Singh N 2006 Magnetic antidot nanostructures: Effect of lattice geometry *Nanotechnology* **17** 1629

[51] Heyderman L J, Nolting F and Quitmann C 2003 X-ray photoemission electron microscopy investigation of magnetic thin film antidot arrays *Appl. Phys. Lett.* **83**

1797

[52] Guedes I, Grimsditch M, Metlushko V, Vavassori P, Camley R, Ilic B, Neuzil P and Kumar R 2003 Magnetization reversal in an Fe film with an array of elliptical holes on a square lattice *Phys. Rev. B - Condens. Matter Mater. Phys.* **67** 024428

[53] A. Krasyuk, S.A. Nepijko, A. Oelsner, C.M. Schneider, H.J. Elmers G S 2007 Magnetic stray fields of patterned permalloy structures investigated by photoemission *Appl. Phys. A Mater. Sci. Process.* . **88** 793–6

[54] Liu C Y, Datta A and Wang Y L 2001 Ordered anodic alumina nanochannels on focused-ion-beam-prepatterned aluminum surfaces *Appl. Phys. Lett.* **78** 120–2

[55] Liu N W, Datta A, Liu C Y and Wang Y L 2003 High-speed focused-ion-beam patterning for guiding the growth of anodic alumina nanochannel arrays *Appl. Phys. Lett.* **82** 1281

[56] Chen B, Lu K and Tian Z 2010 Gradient and alternating diameter nanopore templates by focused ion beam guided anodization *Electrochim. Acta* **56** 435–40

[57] Sun Z and Kim H K 2002 Growth of ordered, single-domain, alumina nanopore arrays with holographically patterned aluminum films *Appl. Phys. Lett.* **81** 3458

[58] Demming A 2013 Designer fabrication: Nanotemplates get in shape *Nanotechnology* **24** 050201

[59] Fournier-Bidoz S, Arsenault A C, Manners I and Ozin G A 2005 Synthetic self-propelled nanorotors *Chem. Commun.* 441–3

[60] Kim B, Park S, McCarthy T J and Russell T P 2007 Fabrication of ordered anodic aluminum oxide using a solvent-induced array of block-copolymer micelles *Small*

**3** 1869–72

[61] Zhang C, Li W, Yu D, Wang Y, Yin M, Wang H, Song Y, Zhu X, Chang P, Chen X and Li D 2017 Wafer-Scale Highly Ordered Anodic Aluminum Oxide by Soft Nanoimprinting Lithography for Optoelectronics Light Management *Adv. Mater. Interfaces* **4** 1601116

[62] Moreno J M M, Waleczek M, Martens S, Zierold R, Görlitz D, Martínez V V, Prida V M and Nielsch K 2014 Constrained Order in Nanoporous Alumina with High Aspect Ratio : Smart Combination of Interference Lithography and Hard Anodization *Adv. Funct. Mater.* **24** 1857–63

[63] Heisenberg W 1926 Mehrkörperproblem und Resonanz in der Quantenmechanik *Zeitschrift für Phys.* **38** 411–26

[64] Dirac P A M 1926 On the Theory of Quantum Mechanics *Proc. R. Soc. A Math. Phys. Eng. Sci.*

[65] Kronmüller H and Fähnle M 2003 Micromagnetism and the Microstructure of Ferromagnetic Solids 448

[66] Hertel R and Kronmüller H 1999 Micromagnetic simulation of the domain structure of a flat rectangular permalloy prism *J. Appl. Phys.* **85** 6190–2

[67] Coey J M D 2010 *Magnetism and magnetic materials* (Cambridge University Press;)

[68] Abo G S, Hong Y K, Park J, Lee J, Lee W and Choi B C 2013 Definition of magnetic exchange length *IEEE Trans. Magn.* **49** 4937–9

[69] Wade R H 1962 The determination of domain wall thickness in ferromagnetic

films by electron microscopy *Proc. Phys. Soc.*

[70] Barthelmess M, Pels C, Thieme A and Meier G 2004 Stray fields of domains in permalloy microstructures - Measurements and simulations *J. Appl. Phys.* **95**

[71] Shaw J M, Russek S E, Thomson T, Donahue M J, Terris B D, Hellwig O, Dobisz E and Schneider M L 2008 Reversal mechanisms in perpendicularly magnetized nanostructures *Phys. Rev. B - Condens. Matter Mater. Phys.* **78** 024414

[72] Cowburn R P, Adeyeye A O and Bland J A C 1997 Magnetic domain formation in lithographically defined antidot Permalloy arrays *Appl. Phys. Lett.* **70** 2309

[73] Stöhr J and König H 1995 Determination of spin- and orbital-moment anisotropies in transition metals by angle-dependent X-ray magnetic circular dichroism *Phys. Rev. Lett.* **75** 3748

[74] Kneller E F and Hawig R 1991 The exchange-spring magnet: A new material principle for permanent magnets *IEEE Trans. Magn.* **27** 3588–3560

[75] Aharoni A 2007 Introduction to the Theory of Ferromagnetism *Oxford Sci. Publ.*

[76] Cullity B D and Graham C D 2013 Introduction to magnetic materials *Choice Rev. Online* **47** 47-0342-47–0342

[77] Prida V M, Salaheldeen M, Pfitzer G, Hidalgo A, Vega V, González S, Teixeira J M, Fernández A and Hernando B 2017 Template assisted deposition of ferromagnetic nanostructures: From antidot thin films to multisegmented nanowires *Acta Phys. Pol. A* **131** 822–7

[78] Paul D I 1982 General theory of the coercive force due to domain wall pinning *J. Appl. Phys.* **53** 1649–54

[79] Friedberg R and Paul D I 1975 New theory of coercive force of ferromagnetic materials *Phys. Rev. Lett.* **34** 1234–7

[80] Navas D, Hernández-Ívlez M, Vázquez M, Lee W and Nielsch K 2007 Ordered Ni nanohole arrays with engineered geometrical aspects and magnetic anisotropy *Appl. Phys. Lett.* **90** 192501

[81] Coey J M D 2011 Hard magnetic materials: A perspective *IEEE Trans. Magn.* **47** 4671–81

[82] Masuda H and Fukuda K 1995 Ordered Metal Nanohole Arrays Made by a Two-Step Replication of Honeycomb Structures of Anodic Alumina *Science.* **268** 1466

[83] López Antón R, Vega V, Prida V M, Fernández A, Pirota K R and Vázquez M 2009 Magnetic Properties of Hexagonally Ordered Arrays of Fe Antidots by Vacuum Thermal Evaporation on Nanoporous Alumina Templates *Solid State Phenom.* **152**–**153** 273–6

[84] Rahman M T, Shams N N, Lai C H, Fidler J and Suess D 2010 Co/Pt perpendicular antidot arrays with engineered feature size and magnetic properties fabricated on anodic aluminum oxide templates *Phys. Rev. B - Condens. Matter Mater. Phys.* **81** 014418

[85] Merazzo K J, Leitao D C, Jiménez E, Araujo J P, Camarero J, Del Real R P, Asenjo A and Vázquez M 2011 Geometry-dependent magnetization reversal mechanism in ordered Py antidot arrays *J. Phys. D. Appl. Phys.* **44** 5001–10

[86] Wiedwald, U.; Gräfe, J.; Lebecki, K. M.; Skripnik, M.; Haering, F.; Schütz, G.; Ziemann, P.; Goering, E.; Nowak U 2016 Magnetic switching of nanoscale antidot lattices *Beilstein J. Nanotechnol.* **7** 733–750

[87] Anon 2019 https://www.nanoscience.com/techniques/scanning-electron-microscopy/

[88] Jaafar M, Gómez-Herrero J, Gil A, Ares P, Vázquez M and Asenjo A 2009 Variable-field magnetic force microscopy *Ultramicroscopy* **109** 693–9

[89] Horcas I, Fernández R, Gómez-Rodríguez J M, Colchero J, Gómez-Herrero J and Baro A M 2007 WSXM: A software for scanning probe microscopy and a tool for nanotechnology *Rev. Sci. Instrum.* **78** 013705

[90] Anon 2019 https://imagej.nih.gov/ij/docs/index.html,

[91] Foner S 1959 Versatile and sensitive vibrating-sample magnetometer *Rev. Sci. Instrum.* **30** 548

[92] Jaafar M, Asenjo A and Vázquez M 2008 Calibration of coercive and stray fields of commercial magnetic force microscope probes *IEEE Trans. Nanotechnol.* **7** 245–50

[93] Jaafar M, Navas D, Asenjo A, Vázquez M, Hernández-Ýelez M and García-Martín J M 2007 Magnetic domain structure of nanohole arrays in Ni films *J. Appl. Phys.* **101** 09F513

[94] Navas D, Hernández-Vélez M, Asenjo A, Jaafar M, Baldonedo J L and Vázquez M 2006 Preparation and magnetic characterization of Ni membranes with controlled highly ordered nanohole arrays *IEEE Trans. Magn.* **42** 3057–9

[95] Anon 2019 http://mumax.github.io

[96] Vansteenkiste A, Leliaert J, Dvornik M, Helsen M, Garcia-Sanchez F and Van Waeyenberge B 2014 The design and verification of MuMax$^3$ *AIP Adv.* **4** 7133–

56

[97] Béron F, Pirota K R, Vega V, Prida V M, Fernández A, Hernando B and Knobel M 2011 An effective method to probe local magnetostatic properties in a nanometric FePd antidot array *New J. Phys.* **13** 013035

[98] Pirota K R, Prieto P, Neto A M J, Sanz J M, Knobel M and Vazquez M 2008 Coercive field behavior of permalloy antidot arrays based on self-assembled template fabrication *J. Magn. Magn. Mater.* **320** 235–8

[99] Leitao D C, Ventura J, Teixeira J M, Sousa C T, Pinto S, Sousa J B, Michalik J M, De Teresa J M, Vazquez M and Araujo J P 2013 Correlations among magnetic, electrical and magneto-transport properties of NiFe nanohole arrays *J. Phys. Condens. Matter* **25** 066007

[100] Castán-Guerrero C, Bartolomé J, Bartolomé F, García L M, Sesé J, Strichovanec P, Herrero-Albillos J, Merazzo K J, Vázquez M and Vavassori P 2013 Coercivity dependence on periodicity of Co and Py antidot arrays *J. Korean Phys. Soc.* **62** 1521–4

[101] Wang C C, Adeyeye A O and Singh N 2006 Magnetic antidot nanostructures: Effect of lattice geometry *Nanotechnology* **17** 1629–36

[102] Gräfe J, Schütz G and Goering E J 2016 Coercivity scaling in antidot lattices in Fe, Ni, and NiFe thin films *J. Magn. Magn. Mater.* **419** 517–20

[103] Zhao Y P, Gamache R M, Wang G C, Lu T M, Palasantzas G and De Hosson J T M 2001 Effect of surface roughness on magnetic domain wall thickness, domain size, and coercivity *J. Appl. Phys.* **89** 1325

[104] Vázquez M, Pirota K R, Navas D, Asenjo A, Hernández-Vélez M, Prieto P and Sanz J M 2008 Ordered magnetic nanohole and antidot arrays prepared through replication from anodic alumina templates *J. Magn. Magn. Mater.* **320** 1978–83

[105] Kern K, Heitmann D, Grambow P, Zhang Y H and Ploog K 1991 Collective excitations in antidots *Phys. Rev. Lett.* **66** 1618

[106] Ctistis G, Papaioannou E, Patoka P, Gutek J, Fumagalli P and Giersig M 2009 Optical and magnetic properties of hexagonal arrays of subwavelength holes in optically thin cobalt films *Nano Lett.* **9** 1–6

[107] Mora B, Perez-Valle A, Redondo C, Boyano M D and Morales R 2018 Cost-Effective Design of High-Magnetic Moment Nanostructures for Biotechnological Applications *ACS Appl. Mater. Interfaces* **10** 8165–72

[108] Garad H, Usmani S, Barral D, David P, Cagnon L, Testemale D, Mannix D, Fettar F, Proux O, Rosa A, Mathon O and Pascarelli S 2018 Influence of the pore diameter in Cu/Co/Cu antidots: A XANES study *Phys. Rev. Mater.* **2** 066001

[109] Xiaoyu Zhang, Alyson V. Whitney, Jing Zhao, Erin M. Hicks R P V D 2006 Advances in Contemporary Nanosphere Lithographic Techniques *J. Nanosci. Nanotechnol.* **6** 1920–34

[110] Baglin J E E 2012 Ion beam nanoscale fabrication and lithography - A review *Appl. Surf. Sci.* **258** 4103–11

[111] Manfrinato V R, Zhang L, Su D, Duan H, Hobbs R G, Stach E A and Berggren K K 2013 Resolution limits of electron-beam lithography toward the atomic scale *Nano Lett.* **13** 1555–8

[112] Heyderman L J, Nolting F, Backes D, Czekaj S, Lopez-Diaz L, Kläui M, Rüdiger U, Vaz C A F, Bland J A C, Matelon R J, Volkmann U G and Fischer P 2006 Magnetization reversal in cobalt antidot arrays *Phys. Rev. B - Condens. Matter Mater. Phys.* **73** 214429

[113] Cowburn R P, Adeyeye A O and Bland J A C 1997 Magnetic switching and uniaxial anisotropy in lithographically defined anti-dot Permalloy arrays *J. Magn. Magn. Mater.* **173** 193

[114] Salaheldeen M, Méndez M, Vega V, Fernández A and Prida V M 2019 Tuning Nanohole Sizes in Ni Hexagonal Antidot Arrays: Large Perpendicular Magnetic Anisotropy for Spintronic Applications *ACS Appl. Nano Mater.* **2** 1866–1875

[115] Merazzo K J, Del Real R P, Asenjo A and Vzquez M 2011 Dependence of magnetization process on thickness of Permalloy antidot arrays *J. Appl. Phys.* **109** 07B906

[116] Béron F, Kaidatzis A, Velo M F, Arzuza L C C, Palmero E M, del Real R P, Niarchos D, Pirota K R and García-Martín J M 2016 Nanometer Scale Hard/Soft Bilayer Magnetic Antidots *Nanoscale Res. Lett.* **11** 1–11

[117] Saldanha D R, Dugato D A, Mori T J A, Daudt N F, Dorneles L S and Denardin J C 2018 Tailoring the magnetic and magneto- transport properties of Pd/Co multilayers and pseudo-spin valve antidots *J. Phys. D. Appl. Phys.* **51** 395001

[118] Castán-Guerrero C, Herrero-Albillos J, Bartolomé J, Bartolomé F, Rodríguez L A, Magén C, Kronast F, Gawronski P, Chubykalo-Fesenko O, Merazzo K J, Vavassori P, Strichovanec P, Sesé J and García L M 2014 Magnetic antidot to dot crossover in Co and Py nanopatterned thin films *Phys. Rev. B - Condens. Matter*

*Mater. Phys.* **89** 144405

[119] Jang Y H and Cho J H 2014 Morphology-dependent multi-step ferromagnetic reversal processes in Co thin films on crescent-shaped antidot arrays *J. Appl. Phys.* **115** 063903

[120] Fettar F, Cagnon L and Rougemaille N 2010 Three-dimensional magnetization profile and multiaxes exchange bias in Co antidot arrays *Appl. Phys. Lett.* **97** 192502

[121] Nguyen, T. N. A.; Fedotova, J.; Kasiuk, J.; Bayev, V.; Kupreeva, O.; Lazarouk, S.; Manh, D. H.; Vu, D. L.; Chung, S.; Akerman, J.; Altynov, V.; Maximenko A 2018 Effect of flattened surface morphology of anodized aluminum oxide templates on the magnetic properties of nanoporous Co/Pt and Co/Pd thin multilayered films *Appl. Surf. Sci.* **427** 649–55

[122] D C Leitao, J Ventura, C T Sousa, J M Teixeira, J B Sousa, M Jaafar, A Asenjo, M Vazquez, J M De Teresa J P Araujo 2012 Tailoring the physical properties of thin nanohole arrays grown on flat anodic aluminum oxide templates *Nanotechnology* **23** 425701

[123] Paz E, Cebollada F, Palomares F J, González J M, Im M Y and Fischer P 2012 Scaling of the coercivity with the geometrical parameters in epitaxial Fe antidot arrays *J. Appl. Phys.* **111** 073908

[124] Ruiz-Feal I, Lopez-Diaz L, Hirohata A, Rothman J, Guertler C M, Bland J A C, Garcia L M, Torres J M, Bartolome J, Bartolome F, Natali M, Decanini D and Chen Y 2002 Geometric coercivity scaling in magnetic thin film antidot arrays *J. Magn. Magn. Mater.* **242**–**245** 597–600

[125] Bruna J M T, Bartolomé J, Vinuesa L M G, Sanchez F G, Gonzalez J M and Chubykalo-Fesenko O A 2005 A micromagnetic study of the hysteretic behavior of antidot Fe films *J. Magn. Magn. Mater.* **290**–**291** 149–52

[126] Prieto P, Pirota K R, Vazquez M and Sanz J M 2008 Fabrication and magnetic characterization of permalloy antidot arrays *Phys. Status Solidi Appl. Mater. Sci.* **205** 363–7

[127] Castán-Guerrero C, Sesé J, Bartolomé J, Bartolomé F, Herrero-Albillos J, Kronast F, Strichovanec P, Merazzo K J, Vázquez M, Vavassori P and García L M 2012 Fabrication and Magnetic Characterization of Cobalt Antidot Arrays: Effect of the Surrounding Continuous Film *J. Nanosci. Nanotechnol.* **12** 7437–41

[128] Krupinski M, Mitin D, Zarzycki A, Szkudlarek A, Giersig M, Albrecht M and Marszałek M 2017 Magnetic transition from dot to antidot regime in large area Co/Pd nanopatterned arrays with perpendicular magnetization *Nanotechnology* **28** 085302

[129] Chappert C, Fert A and Van Dau F N 2007 The emergence of spin electronics in data storage *Nat. Mater.* **6** 813–823

[130] Brataas A, Kent A D and Ohno H 2012 Current-induced torques in magnetic materials *Nat. Mater.* **11** 372–381

[131] Dieny B and Chshiev M 2017 Perpendicular magnetic anisotropy at transition metal/oxide interfaces and applications *Rev. Mod. Phys.* **89** 5008–62

[132] Monso S, Rodmacq B, Auffret S, Casali G, Fettar F, Gilles B, Dieny B and Boyer P 2002 Crossover from in-plane to perpendicular anisotropy in Pt/CoFe/AlO x sandwiches as a function of Al oxidation: A very accurate control of the oxidation

of tunnel barriers *Appl. Phys. Lett.* **80** 4157–9

[133] Ikeda S, Miura K, Yamamoto H, Mizunuma K, Gan H D, Endo M, Kanai S, Hayakawa J, Matsukura F and Ohno H 2010 A perpendicular-anisotropy CoFeB-MgO magnetic tunnel junction *Nat. Mater.* **9** 721–724

[134] Mangin S, Ravelosona D, Katine J A and Fullerton E E 2006 Current-induced magnetization reversal in nanopillars with perpendicular anisotropy *Nat. Mater.* **5** 210–215

[135] Miron I M, Garello K, Gaudin G, Zermatten P J, Costache M V., Auffret S, Bandiera S, Rodmacq B, Schuhl A and Gambardella P 2011 Perpendicular switching of a single ferromagnetic layer induced by in-plane current injection *Nature* **476** 189–193

[136] Emori S and Beach G S D 2011 Optimization of out-of-plane magnetized Co/Pt multilayers with resistive buffer layers *J. Appl. Phys.* **110** 3919–24

[137] Dai B, Kato T, Iwata S and Tsunashima S 2013 Temperature dependence of critical current density of spin transfer torque switching amorphous GdFeCo for thermally assisted MRAM *IEEE Trans. Magn.* **49** 4359–62

[138] Dai B, Guo Y, Zhu J, Kato T, Iwata S, Tsunashima S, Yang L and Han J 2017 Spin transfer torque switching in exchange-coupled amorphous GdFeCo/TbFe bilayers for thermally assisted MRAM application *J. Phys. D. Appl. Phys.* **50**

[139] Kaidatzis A, Del Real R P, Alvaro R, Palma J L, Anguita J, Niarchos D, Vázquez M, Escrig J and García-Martín J M 2016 Magnetic properties engineering of nanopatterned cobalt antidot arrays *J. Phys. D. Appl. Phys.* **49** 5004–12

[140] Rollinger M, Thielen P, Melander E, Östman E, Kapaklis V, Obry B, Cinchetti M, García-Martín A, Aeschlimann M and Papaioannou E T 2016 Light Localization and Magneto-Optic Enhancement in Ni Antidot Arrays *Nano Lett.* **16** 2432–8

[141] Yang H, Chen G, Cotta A A C, N'DIaye A T, Nikolaev S A, Soares E A, MacEdo W A A, Liu K, Schmid A K, Fert A and Chshiev M 2018 Significant Dzyaloshinskii-Moriya interaction at graphene-ferromagnet interfaces due to the Rashba effect *Nat. Mater.* **17** 605–609

[142] Yang H, Vu A D, Hallal A, Rougemaille N, Coraux J, Chen G, Schmid A K and Chshiev M 2016 Anatomy and Giant Enhancement of the Perpendicular Magnetic Anisotropy of Cobalt-Graphene Heterostructures *Nano Lett.* **16** 145–51

[143] Han H, Park S J, Jang J S, Ryu H, Kim K J, Baik S and Lee W 2013 In situ determination of the pore opening point during wet-chemical etching of the barrier layer of porous anodic aluminum oxide: Nonuniform Impurity Distribution in Anodic Oxide *ACS Appl. Mater. Interfaces* **5** 3441–8

[144] Phuoc N N, Lim S L, Xu F, Ma Y G and Ong C K 2008 Enhancement of exchange bias and ferromagnetic resonance frequency by using multilayer antidot arrays *J. Appl. Phys.* **104** 3708–13

[145] Béron F, Pirota K R, Vega V, Prida V M, Fernández A, Hernando B and Knobel M 2011 An effective method to probe local magnetostatic properties in a nanometric FePd antidot array *New J. Phys.* **13** 3035–51

[146] Jang Y H and Cho J H 2014 Morphology-dependent multi-step ferromagnetic reversal processes in Co thin films on crescent-shaped antidot arrays *J. Appl. Phys.* **115** 3903–8

[147] Gawronski P, Merazzo K J, Chubykalo-Fesenko O, Del Real R P and Vázquez M 2014 Micromagnetism of permalloy antidot arrays prepared from alumina templates *Nanotechnology* **25** 475703

[148] Lambert C H, Rajanikanth A, Hauet T, Mangin S, Fullerton E E and Andrieu S 2013 Quantifying perpendicular magnetic anisotropy at the Fe-MgO(001) interface *Appl. Phys. Lett.* **102** 2410–5

[149] Lee J, Brombacher C, Fidler J, Dymerska B, Suess D and Albrecht M 2011 Contribution of the easy axis orientation, anisotropy distribution and dot size on the switching field distribution of bit patterned media *Appl. Phys. Lett.* **99** 062505

[150] Yanagishita T, Nishio K and Masuda H 2005 Fabrication of metal nanohole arrays with high aspect ratios using two-step replication of anodic porous alumina *Adv. Mater.* **17** 2241–3

[151] FL Krishnan, H. Lassri, Shiva Prasad M P and M T 1993 Magnetic properties of Ni/Pt multilayers *J. Appl. Phys.* **73** 6433

[152] Jeong J-R, Kim Y-S and Shin S-C 1999 Origins of perpendicular magnetic anisotropy in Ni/Pd multilayer films *J. Appl. Phys.* **85** 085762

[153] Inglefield H E, Bochi G, Ballentine C A, O'Handley R C and Thompson C V. 1996 Perpendicular magnetic anisotropy in epitaxial Cu/Ni/Cu/Si (001) *Thin Solid Films* **275** 155–8

[154] Jungblut R, Johnson M T, Aan De Stegge J, Reinders A and Den Broeder F J A 1994 Orientational and structural dependence of magnetic anisotropy of Cu/Ni/Cu sandwiches: Misfit interface anisotropy *J. Appl. Phys.* **75** 6424

[155] Manzin A and Bottauscio O 2012 Micromagnetic modelling of the anisotropy properties of permalloy antidot arrays with hexagonal symmetry *J. Phys. D. Appl. Phys.* **45** 095001

[156] Ladak S, Walton S K, Zeissler K, Tyliszczak T, Read D E, Branford W R and Cohen L F 2012 Disorder-independent control of magnetic monopole defect population in artificial spin-ice honeycombs *New J. Phys.* **14** 045010

[157] Farhan A, Derlet P M, Anghinolfi L, Kleibert A, Heyderman L J 2017 Magnetic charge and moment dynamics in artificial kagome spin ice *Phys. Rev. B* **96**

[158] Radu F, Abrudan R, Radu I, Schmitz D and Zabel H 2012 Perpendicular exchange bias in ferrimagnetic spin valves *Nat. Commun.* **3** 715–7

[159] I. Radu, K.Vahaplar, C. Stamm, T.Kachel, N. Pontius, H. A. Du¨rr, T. A. Ostler, J. Barker, R. F.L.Evans, R.W.Chantrell, A. Tsukamoto, A.Itoh, A. Kirilyuk T R and A V K 2011 Transient ferromagnetic-like state mediating ultrafast reversal of antiferromagnetically coupled spins *Nature* **472** 205–208

[160] Hassdenteufel A, Hebler B, Schubert C, Liebig A, Teich M, Helm M, Aeschlimann M, Albrecht M and Bratschitsch R 2013 Thermally Assisted All-Optical Helicity Dependent Magnetic Switching in Amorphous $Fe_{100-x}$ $Tb_x$ Alloy Films *Adv. Mater.* **25** 3122–8

[161] K. Fleury-Frenette, J. Delwiche, F. Grandjean, D. Vandormael and G J L 2001 Magnetic and conversion electron Mössbauer spectral study of amorphous thin films of $Dy_xFe_{100-x}$ and $Dy_{20}Fe_{80-y}Co_y$ *J. Appl. Phys.* **90** 1934–40

[162] Tang M H, Zhang Z, Tian S Y, Wang J, Ma B and Jin Q Y 2015 Interfacial exchange coupling and magnetization reversal in perpendicular [Co/Ni]N/TbCo

composite structures *Sci. Rep.* **5** 1–7

[163] Chen K, Lott D, Radu F, Choueikani F, Otero E and Ohresser P 2015 Observation of an atomic exchange bias effect in $DyCo_4$ film *Sci. Rep.* **5** 1–8

[164] Fust S, Mukherjee S, Paul N, Stahn J, Kreuzpaintner W, Böni P and Paul A 2016 Realizing topological stability of magnetic helices in exchange-coupled multilayers for all-spin-based system *Sci. Rep.* **6** 1–14

[165] Hansen P, Klahn S, Clausen C, Much G and Witter K 1991 Magnetic and magneto-optical properties of rare-earth transition-metal alloys containing Dy, Ho, Fe, Co *J. Appl. Phys.* **69** 3194–207

[166] Kumail S, Akbar A, Atiq S, Saleem M, Iftikhar M, Naseem S and Sabieh M 2019 Optimization of DyFe nanostructures using E-beam lithography for magneto-optical applications *J. Magn. Magn. Mater.* **469** 196–202

[167] Svalov A V., Fernandez A, Vas'kovskiy V O, Kurlyandskaya G V., Barandiarán J M, Anton R L and Tejedor M 2006 MOKE study of Co/Ti/(Gd-Co) multilayers near the magnetic compensation state *J. Alloys Compd.* **419** 25–31

[168] Leamy H J and Dirks A G 1979 Microstructure and magnetism in amorphous rare-earth-transition-metal thin films. II. Magnetic anisotropy *J. Appl. Phys.* **50** 2871

[169] Leamy H J and Dirks A G 1978 Microstructure and magnetism in amorphous rare-earth–transition-metal thin films. I. Microstructure *J. Appl. Phys.* **49** 3034

[170] R. Carey, L. Dieu and D. M. Newman 1997 Thickness variation of the magnetic anisotropy in DyFe thin films using magneto-optical techniques *IEEE Trans. Magn.* **33** 3922–4

[171] Gong W J, Yu W J, Liu W, Guo S, Ma S, Feng J N, Li B and Zhang Z D 2012 Exchange bias and its thermal stability in ferromagnetic/antiferromagnetic antidot arrays *Appl. Phys. Lett.* **101** 2407

[172] Caballero-Flores R, Bingham N S, Phan M H, Torija M A, Leighton C, Franco V, Conde A, Phan T L, Yu S C and Srikanth H 2014 Magnetocaloric effect and critical behavior in $Pr_{0.5}Sr_{0.5}MnO_3$: An analysis of the validity of the Maxwell relation and the nature of the phase transitions *J. Phys. Condens. Matter* **26** 286001

[173] Punz D, Lee J, Fuger M, Fidler J, Schrefl T and Suess D 2010 Theory and micromagnetics of pinning mechanism at cylindrical defects in perpendicular magnetic films *J. Appl. Phys.* **107** 113926

[174] Mansuripur M 1990 Analysis of multilayer thin film structures containing magnetooptic and anisotropic media at oblique incidence using 2×2 matrices *J. Appl. Phys.* **67** 6466

[175] Ambrose M C and Stamps R L 2013 Magnetic stripe domain pinning and reduction of in-plane magnet order due to periodic defects in thin magnetic films *J. Magn. Magn. Mater.* **344** 140–7

[176] D. Weller, J. Stohr, R. Nakajima, A. Carl, M. G. Samant, C. Chappert R M, Beauvillain P and P. Veillet and G A H 1995 Microscopic Origin ofMagnetic Anisotropy in Au/Co/Au Probed with X-Ray Magnetic Circular Dichroism *Phys. Rev. Lett.* **75** 2219–23

[177] F. Baudelet, M.-T. Lin, W. Kuch, K. Meinel B C and C.M. Schneider. J.Kirschner 1995 Perpendicular anisotropy and spin reorientation in epitaxial Fe/Cu3Au(100) thin films *Phys. Rev. B* **51** 12564

# Publications and attended conferences

## 10.1 PhD thesis outcome publications

1- **Salaheldeen M**, Méndez M, Vega V, Fernández A and Prida V M 2019. Tuning Nanohole Sizes in Ni Hexagonal Antidot Arrays: Large Perpendicular Magnetic Anisotropy for Spintronic Applications. ACS Appl. Nano Mater. **2** 1866–1875.

2- **Salaheldeen M**, Vega V, Ibabe A, Jaafar M, Asenjo A, Fernandez A and Prida V M 2018. Tailoring of Perpendicular Magnetic Anisotropy in $Dy_{13}Fe_{87}$ Thin Films with Hexagonal Antidot Lattice Nanostructure. Nanomaterials **8** 227.

3- Prida V M, **Salaheldeen M**, Pfitzer G, Hidalgo A, Vega V, González S, Teixeira J M, Fernández A and Hernando B 2017. Template assisted deposition of ferromagnetic nanostructures: From antidot thin films to multisegmented nanowires. Acta Phys. Pol. A **131** 822–7.

4- **Salaheldeen M**, Vega V, Caballero-Flores R, Prida V M, Fernández A. Influence of nanoholes array geometrical parameters on magnetic properties of Dy-Fe antidot thin films. Nanotechnology submitted on (5/4/2019).

## 10.2 Attended conferences and congresses related to this PhD thesis

1- **M. Salaheldeen**, M. Raaif, V. M. Prida, V. Vega, A. Fernández, "Nanometer scale thickness effect in magnetic Fe-based antidot arrays", XIV Congreso Nacional de Materiales, 8-10 Junio, 2016, Gijón, España. (Póster)

2- V. M. Prida. V. Vega, S. González, **M. Salaheldeen**, J. M. Mesquita, A. Fernández and B. Hernando "Template Assisted Deposition of Ferromagnetic Nanostructures: from Antidot Thin Films to Multisegmented Nanowires and Metallic Nanotubes" 16th Czech and Slovak Conference on Magnetism, 13-17 June, 2016, Košice, Slovakia. (Conferencia Invitada).

3- **M. Salaheldeen**, M. Raaif, J.M. Teixeira, V.M. Prida, A. Fernández "Geometrical engineering of magnetization reversal in Ni, Co and NiFe- based antidot lattices "in International Conference on Chemical Sciences and Applications (ICCSA-2016) 6-9 Aug 2016, Alexandria, Egypt. (Ponencia Oral).

4- **M. Salaheldeen**, V.M. Prida, A. Fernández "Tailoring the magnetic properties of DyFe antidot arrays by varying the film thickness and degree of disorder" 1st Egy Nanophotonics and Nanophononics Conference 10-13 August 2016, Hurghada, Egypt. (Ponencia Oral).

5- **M.Salaheldeen**, V. Vega, A. Ibabe, M. Jaafar, A. Asenjo V.M. Prida, A. Fernández "Tailoring perpendicular magnetic anisotropy in $Dy_{12}Fe_{88}$ thin films hexagonal antidot lattices "24rd International Symposium on Metastable, Amorphous and Nanostructured Materials, ISMANAM 2017, June 18th-23th 2017. (Poster).

6- R. Caballero-Flores; **M. Salaheldeen**; L. J. Fernández; M. Méndez; A. S. González; V. Vega; V. M. Prida; A. Fernández; B. Hernando. "Template assisted deposition of ferromagnetic nanostructures: From antidots thin films to multisegmented nanowire and metallic nanotube", XXXVI Reunión Bienal de la Real Sociedad Española de Física, 17-21/07/2017, Santiago, Spain. (Poster)